

SELF-CONSISTENT MEAN FIELD THEORY
OF THE MICROPHASES OF NEAT
DIBLOCK COPOLYMERS

By

©Jeffrey David Vavasour

A THESIS SUBMITTED IN PARTIAL
FULFILLMENT OF THE REQUIREMENTS
FOR THE DEGREE OF
BACHELOR OF SCIENCE (HONOURS)

DEPARTMENT OF PHYSICS
MEMORIAL UNIVERSITY OF NEWFOUNDLAND

APRIL 1992

ST. JOHN'S

NEWFOUNDLAND

Abstract

A mean field theory of polymer blends [17] has been extended to treat systems of neat diblock copolymers. We have derived a set of self-consistent equations describing the probability distribution functions, and devised and implemented convergent numerical techniques to solve this system of equations for a wide range of physical parameters.

The primary numerical work was a study of the equilibrium morphology of these systems. Applying the self-consistent theory to a model system, we constructed a phase diagram which exhibits the equilibrium morphology as a function of the effective degree of polymerization, r_C , the volume fractions of the two blocks, f_A and $f_B \equiv 1 - f_A$, and the Flory interaction parameter, χ_{AB} . In a second investigation, the numerical techniques were used to calculate the lattice parameter R for specific morphologies and values of f_A , as a function of χ_{AB} and r_C . The results were expressed in terms of a power law, $R \propto \chi_{AB}^p r_C^q$.

This work unifies the results of earlier calculations, which represent limiting cases of the present work, and provides satisfactory agreement with experiment. Through an analytic treatment, we were able to show that, in general, the equilibrium morphology is a function of f_A , the product $\chi_{AB} r_C$, and ϵ where the latter parameter is characteristic of the two blocks. A similar generalisation revealed the exponents of the lattice parameter power law to be related by $q = p + 1/2$.

Finally, we outline analytic extensions to our approach which encompass systems other than those discussed here. These include copolymer/homopolymer and copolymer/solvent blends as well as molecules of more complex architectures.

Acknowledgements

I wish to thank my supervisor, Dr. Mark Whitmore, for his enthusiastic support and encouragement in this project and throughout my undergraduate career. The time and interest which he has offered have made the past four years of my academic life both pleasant and highly informative.

I would like to acknowledge Michał Banaszak for helpful instruction and important commentary on our numerical techniques. Also, thanks to André Roberge for interesting and stimulating conversation. I would also like to thank everybody in the Physics Department who helped to make academia enjoyable.

Finally, I would like to extend my deepest love and gratitude to my parents whose encouragement and understanding have been an inspiration. It has meant more to me than they will ever know.

“Dad, I want to be a physicist.”

“And what do they grow, son?”

– from the movie *Young Einstein*

Table of Contents

Abstract	ii
Acknowledgements	iii
List of Tables	vi
List of Figures	vii
1 Introduction	1
2 Formalism	11
2.1 The Functional Integral Representation	11
2.2 The Mean Field Approximation	18
2.3 Method of Numerical Solution	29
3 The Phase Diagram and Density Distributions	37
3.1 Introduction	37
3.2 Results and Discussion	41
3.3 Generalisation of the Phase Diagram	52
3.4 The Dilution Approximation	57
4 Equilibrium Domain Sizes	61
4.1 Introduction	61
4.2 Results and Discussion	63

5 Summary and Conclusions	74
Bibliography	80
Appendix A Tables of Numerical Results	84
Appendix B Extensions to Other Architectures and Blends	94
B.1 Linear Multiblock Copolymers	94
B.2 Star Diblock Copolymers	97
B.3 Copolymer/Homopolymer Blends	99

List of Tables

2.1	Weight function for an integral of m dimensions.	31
3.1	Parameter ranges for the three investigated phase diagrams.	38
A.1	Free energy comparison between layers and cylinders for $\chi_{AB} = 0.04$, $Z = 500$, $f_A = 0.626$ to 0.638	84
A.2	Phase transition boundaries for $Z = 500$	85
A.3	Phase transition boundaries for $Z = 200$	86
A.4	Phase transition boundaries for $\chi_{AB} = 0.1$	87
A.5	Mean phase boundaries of $Z = 500$, $Z = 200$, and $\chi_{AB} = 0.1$ diagrams. .	88
A.6	Dependence of repeat distance, d , on χ_{AB} and Z for lamellar structure at $f_A = 0.5$	89
A.7	Dependence of cell radius, R , on χ_{AB} and Z for cylindrical structure at $f_A = 0.7$	91
A.8	Dependence of cell radius, R , on χ_{AB} and Z for spherical structure at $f_A = 0.9$	93

List of Figures

1.1	Common ordered morphologies of diblock copolymers.	5
2.1	Minimisation of the free energy density with respect to lamellar repeat distance, d	36
3.1	Determination of the equilibrium structure for $\chi_{AB} = 0.04$, $Z = 500$	39
3.2	Composite phase diagram for the three investigations.	42
3.3	Sample density profiles for the lamellar structure.	44
3.4	Sample density profiles for the cylindrical structure.	45
3.5	Sample density profiles for the spherical structure.	47
4.1	Dependence of the repeat distance d on χ_{AB} and Z for layers at $f_A = 0.5$	64
4.2	Dependence of the cell radius R on χ_{AB} and Z for cylinders at $f_A = 0.7$	66
4.3	Dependence of the cell radius R on χ_{AB} and Z for spheres at $f_A = 0.9$	68
4.4	Generalised power law relation for layers, cylinders and spheres. The rescaled lattice parameter $RZ^{-1/2}$ is given as a function of $\chi_{AB}Z$	71
4.5	Rescaled free energy density as a function of $\chi_{AB}Z$ for the three selected morphologies and associated f_A values.	73

Chapter 1

Introduction

Polymers are of great interest both theoretically for their fascinating properties and experimentally for their practical value in science and industry. [6] Virtually all synthetics such as plastics, rubber, and styrofoam are made from polymer material. Polymers are also found in living systems in the form of starch, cellulose, glycogen and other molecules. This has made for a widespread demand for research in the fields of polymer chemistry and engineering.

In this respect, it is desirable to form theoretical models of these chemical systems, both to facilitate the understanding of the inherent chemical and physical properties and to predict the outcome of potentially time-consuming and expensive experiments. Such systems are ideally suited for treatment using the techniques of statistical mechanics, and thus become problems of physics.

In its most basic form, a polymer is a macromolecule consisting of a chain built from simpler chemical units, termed monomers. [6] Examples of these monomers include styrene, isoprene, or butadiene. In these cases, a terminating hydrogen molecule is removed from each monomer to create a bonding site for another monomer. Polymer molecules constructed entirely from monomers of a single species are termed *homopolymers*. For the monomers given above, the corresponding homopolymer would be polystyrene (PS), polyisoprene (PI), or polybutadiene (PBD) respectively. In many cases, these are linear chains. However, one can also form *graft polymers* in which there can be several branches.

A *diblock copolymer* is formed when two distinct linear homopolymers are bonded together at one end. Each homopolymer constituent becomes a “block” of the copolymer molecule. In standard notation, a copolymer molecule comprised of polystyrene and polyisoprene is designated PS-*b*-PI. Similarly, a polystyrene-polybutadiene diblock copolymer would be PS-*b*-PBD. As before, more complicated structures are possible. For example, one can attach another homopolymer to one end to form a triblock copolymer. Alternately, one could intersperse two or more monomer species in the chain to form both random and alternating copolymers.

An interesting effect arises in copolymer systems. As the blocks of a diblock copolymer are distinct, they will have unique chemical properties. This usually results in a net repulsive interaction between unlike monomers within the copolymer, which is characterised by an interaction energy found experimentally to have the form $AT + B$ where A and B are constants. This repulsion may be attributed to distinct polarizabilities, incompatible molecular geometries, entropic contributions and other factors. We define a dimensionless parameter χ_{AB} , known as the Flory interaction parameter, [9] which is the interaction energy divided by $k_B T$. It is therefore roughly correlated with temperature by the relation

$$\chi_{AB} \approx A' + \frac{B'}{T}, \quad (1.1)$$

If the repulsive strength χ_{AB} is strong enough, the molecules will attempt to reduce the contact between unlike monomers. For a system of distinct homopolymers, this may be sufficient to cause *macrophase* separation where the components separate into segregated domains much the same as is observed with oil and water. For copolymers, macrophase separation would require total dissociation of the copolymer into its homopolymer block components. Under normal circumstances, however, the two blocks of

the copolymer cannot break their chemical bonds. Thus, copolymer segregation is accomplished through an alignment of the molecules, resulting in a periodic ordered structure. This tendency is opposed by the reduction in entropy associated with ordering. This ordering phenomenon is known as *microphase* separation as the chemical bonds between the two blocks of a single copolymer molecule prevent the periodicity of this structure from being more than a few hundred angstroms in size. The transition to this ordered structure is known as the microphase separation transition, or MST.

In the body of this thesis, we present a new statistical mechanical model for the simplest polymer molecules in which this ordering occurs, a system of neat diblock copolymers. The term “neat” indicates that the chemical system is comprised entirely of diblock copolymers; no solvent or other distinct molecule is present. We further assume that the system is *monodisperse*. That is, all copolymer molecules are assumed to be identical. The study of this type of polymer is far from simply pedagogical, however. Extensive experimental data are available for comparison.

To treat this system, we must first establish some basic terminology and notation. Recalling that this molecule is comprised of two blocks, a relevant experimental parameter is the number of monomers in each block. These are the *block degrees of polymerization*. In our analysis, we will be considering two generic monomers, rather than specific species such as styrene or isoprene. We shall designate these monomers and their associated blocks as type *A* and *B*. Throughout this thesis, we shall use κ to represent either one of these monomer species. Thus, the degree of polymerization of species κ will be denoted as Z_κ . That is, the number of monomers per copolymer molecule of type *A* is Z_A and the number of type *B* is Z_B . We further define $Z \equiv Z_A + Z_B$ as the total degree of polymerization of the copolymer.

Another important characteristic of each species which we denote $\rho_{0\kappa}$ is the number of monomers per unit volume for a bulk system composed entirely of species κ . The

mean effective volume per monomer is thus $1/\rho_{0\kappa}$. Therefore, the total volume occupied by block κ for each copolymer molecule will be $Z_\kappa/\rho_{0\kappa}$. For convenience, we measure this volume with respect to a reference volume $1/\rho_{ref}$, where the density ρ_{ref} is used in the definition of χ_{AB} (see Section 2.2). Each reduced block volume is thus

$$r_\kappa = Z_\kappa \frac{\rho_{ref}}{\rho_{0\kappa}}. \quad (1.2)$$

In terms of this reference volume, the total volume of the copolymer molecule is

$$r_C = r_A + r_B. \quad (1.3)$$

This is known as the effective degree of polymerization of the copolymer.

A final quantity which we will find of use is the volume fraction of each species κ . This is the fraction of the copolymer volume which is comprised of species κ , written as

$$f_\kappa = \frac{r_\kappa}{r_C}, \quad (1.4)$$

where we recognise that $f_A + f_B = 1$. For neat copolymers, this is the same as the total volume fraction, $\bar{\phi}_\kappa$, which denotes the fraction of the *system's* volume occupied by species κ . If other molecules were present, as discussed in Section 3.4 and Appendix B.3, we would have $\bar{\phi}_\kappa < f_\kappa$. Since the primary focus of our investigation was neat diblock copolymers, these quantities will be considered equivalent throughout this thesis unless otherwise noted.

Having established our notation, we turn to the problem of interest. As mentioned above, for sufficiently high values of χ_{AB} , ordered structures are observed. In the case of diblock copolymers, four such structures are known. [30] The type of structure that forms is determined primarily by f_A (or equivalently $f_B = 1 - f_A$), and to a lesser extent by χ_{AB} , and r_C . Figure 1.1 identifies idealised extremes of three of these structures. One possible morphology, indicated in Figure 1.1(a), is the lamellar structure, which we

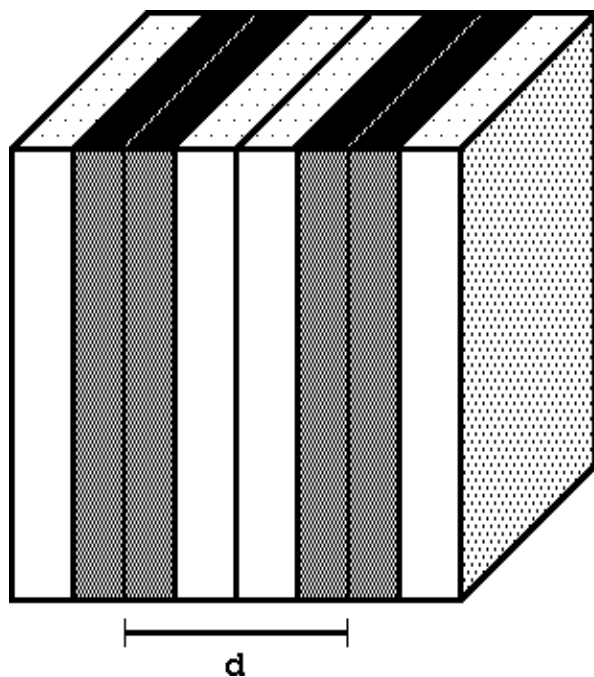
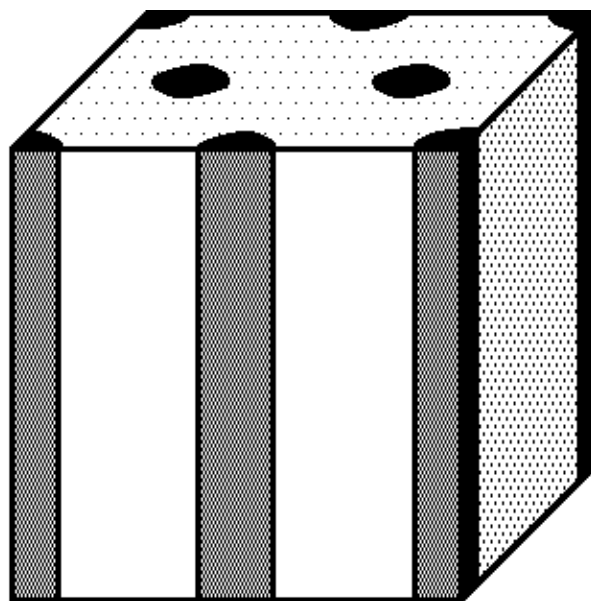
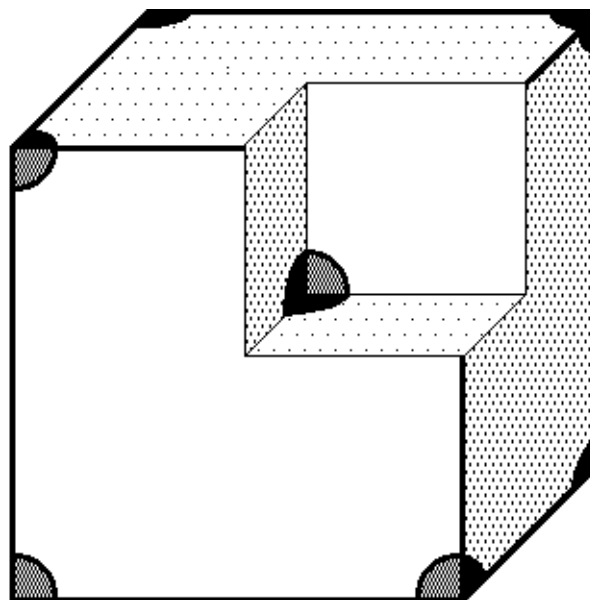
(a) *L structure*(b) *C structure*(c) *S structure*

Figure 1.1: Common ordered morphologies of diblock copolymers. (a) Lamellar with repeat distance d , (b) cylinders on a hexagonal lattice, (c) spheres on a *bcc* lattice. The black and white regions represent areas where one of the two monomer species dominate. The white area will be the majority component of the copolymer. These are idealised strong segregation cases. Intermixing is possible at the boundaries between regions.

designate L. In this example, the copolymer molecules arrange themselves in periodic layered structures such that the bonds between the A and B blocks lie in interfacial planar-like regions. The A blocks then extend to one side of these planes while the B block extends to the other.

We define a local volume fraction, $\phi_\kappa(\mathbf{r})$ which specifies the fraction of the volume at \mathbf{r} occupied by monomers of species κ . In the extreme of Figure 1.1(a), this would be a step function, being either 0 or 1 depending on the subdomain. In practice, there is intermixing in the interphase region which will tend to round off this function in the region between subdomains. Systems in which appreciable intermixing occurs, especially over the entire domain, are said to be weakly segregated. Those in which well defined subdomains form, having step-like local volume fractions, are strongly segregated. The morphologies indicated in Figure 1.1 are idealisations of the strong segregation limit.

Another possible structure, indicated in Figure 1.1(b), is a hexagonal lattice of cylindrical subdomains. Here, each A - B bond is located on the surface of a cylinder with one block inside the cylinder and the other one the outside. The block inside the cylinder is the minority component, having the smaller f_κ . These cylindrical domains are arranged on a hexagonal lattice. A third possibility, Figure 1.1(c), is a spherical domain arranged on a body-centred cubic (bcc) lattice. Again, the species in the core of the spherical subdomain is the minority component.

A fourth structure not shown in Figure 1.1 and not considered in this thesis is the “Ordered Bicontinuous Double-Diamond” structure. [25, 26] If we were to visualise two interlaced diamond structures, the minority component would be centred on the tetrapedal segments of the lattice, with the other component permeating the surrounding medium. In the case of the C and S structure, we are able to reduce the unit cell to a one-dimensional problem using the Wigner-Seitz method of approximating the primitive unit cell as a cylinder or sphere respectively. This is important as, in our approach, we

must solve a diffusion equation for the structure. There is no readily apparent dimension-reducing symmetry in the OBDD structure and so, to model it, we would have to solve, numerically, a partial differential equation in three dimensions. The computation time and storage requirements for even a modest three-dimensional grid are of a magnitude unsuitable for a project of this nature. (See Section 2.3 for details.) As such, the modelling of this structure is left to future investigation.

Experimental evidence of this ordering behaviour has primarily been obtained for strongly segregated systems. [14] An important result is that, in almost all observed cases, the transitions between two ordered microphases were virtually independent of temperature and r_C . In the strong segregation regime, it is found that the lamellar structure occurs in polymers of relatively low asymmetry, specifically in the range of $0.35 \lesssim f_A \lesssim 0.65$. For $0.2 \lesssim f_A \lesssim 0.35$ or $0.65 \lesssim f_A \lesssim 0.8$, a cylindrical structure is observed. Otherwise, when $f_A \lesssim 0.2$ or $f_A \gtrsim 0.8$, the spherical domains on the *bcc* lattice are observed. In addition, the OBDD structure is observed in PS-*b*-PI systems for PI volume fractions between 0.27 and 0.38. [26] In the weak segregation regime, the position of the MST was found to be determined by χ_{AB} , r_C and f_A . [15] However, one recent experiment [4] has found that the morphology in weakly segregated systems is determined not only by f_A but also by the temperature, and thus χ_{AB} . Experiments on ordering in the weak segregation limit are sparse, however.

Prior theoretical investigations into this ordering phenomenon have employed assumptions about the details of the structure. Helfand and Wasserman assumed large r_C and χ_{AB} leading to strongly segregated systems. [16] This is known as the narrow interphase approximation (NIA), referring to the relatively small amount of intermixing between subdomains as indicated for the morphologies in Figure 1.1. This theory predicts reasonable locations for the phase boundaries in strong segregation for PS-*b*-PBD, where the morphology is found to be dependent only on f_A . However, the NIA does not

apply near the MST, at least for nearly symmetric copolymers, as this is in the weak segregation regime. Furthermore, the NIA predicts no temperature dependent changes in morphology such as those observed recently in the weak segregation limit. [4]

Complementary to this is Leibler's treatment [20] which assumes that the difference between the local volume fractions of each component is small and is approximated by a Fourier series of the form

$$\phi_{\kappa}(\mathbf{r}) = \sum_{\mathbf{k}} A_{\mathbf{k}} e^{i\mathbf{k}\cdot\mathbf{r}}, \quad (1.5)$$

where the sum was restricted to include only the wavevectors \mathbf{k} which correspond to the fundamental reciprocal lattice vectors of the one-dimensional, two-dimensional *hex*, and three-dimensional *bcc* lattices as appropriate. Higher-order Fourier components were neglected. In addition, the free energy of the system was evaluated only to fourth order. These conditions were assumed to apply the weak segregation regime, in which the low amplitude of variations in the local volume fractions implied appreciable intermixing. Leibler's theory has been widely used for locating the MST. However, the predicted microphase boundaries for transitions between two ordered structures differ dramatically from NIA. Here, instead of the morphology being determined almost exclusively by f_A , there was a strong temperature dependence through χ_{AB} . Decreasing the temperature, the first structure to form after the MST for an asymmetric copolymer was predicted to be the *bcc* spherical structure. The morphology then changed to cylinders and layers as temperature decreased. For symmetric copolymer, layers were always predicted upon ordering, consistent with experiment. There were large discrepancies in other predictions, however. In particular, the spherical structure was restricted to a very narrow region in the weak segregation regime near MST, in clear disagreement with observation. The cylindrical structure also occurred exclusively at high asymmetries with the lamellar structure occurring for a much wider range of parameters than was observed in practice.

Both of these theories utilised the mean field approximation, in which the system configuration of highest Boltzmann probability was assumed to be the equilibrium state. Fredrickson and Helfand extended Leibler's approach to include fluctuations about the mean field. [11] The MST was modified by this approach such that direct transitions from a homogeneous disordered state to the L or C structure were possible. However, it also resulted in an even more restricted range of parameters for which the S structure was predicted. Overall, the inclusion of fluctuations did not significantly improve agreement with experiment. This failure may be attributed to the fact that, despite the inclusion of fluctuations, the weak segregation assumption of equation (1.5) and the fourth-order expansion of the free energy were still employed.

Small angle X-ray and neutron scattering are often used in the analysis of experimental systems. [13] Due to the low contrast between the species involved, both being hydrocarbon compounds, it is not possible to determine the density variations, but only the morphology type and fundamental lattice parameters. If we can successfully predict these properties, then this would lend credence to our theory, and perhaps provide insight into experimentally undetectable aspects of this behaviour.

In our approach, we do not use any assumptions on the nature of the density variations. Instead, we derive a set of self-consistent equations which are solved numerically to predict the correct equilibrium morphology, its density profiles and associated characteristics. This approach follows an analogous formalism to that of Hong and Noolandi, [17] who developed a self-consistent theory of polymer/solvent blends which they initially applied to determine interface characteristics in macrophase separation. This approach has already been successfully applied to systems involving diblock copolymers in a solvent. [2, 3, 18, 28, 29] The absence of solvent in our present case requires us to construct a modified approach. By adapting this theory for microphase separation in neat diblock copolymer systems, we have predicted the equilibrium morphological behaviour over the

entire range of system parameters which is consistent with experiment. We have chosen to study the model system $\rho_{ref} = \rho_{0A} = \rho_{0B}$ and $b_A = b_B$, where b_k is the mean effective separation between monomers, known as the Kuhn statistical bond length. The results unify those of the NIA and Leibler's weak segregation theory in their respective domains, providing a more general and experimentally consistent picture of copolymer systems.

We find that the MST and equilibrium morphologies for our model system are, in the self-consistent mean field theory, entirely determined by the parameter f_A and the product $\chi_{AB}r_C$. Furthermore, we derive analytically in Section 3.3 that the system is, in the most general sense of mean field theory, determined by these two quantities and a third parameter $\epsilon = \rho_{0B}b_B^2/\rho_{0A}b_A^2$.

The remainder of this thesis is organised as follows: Chapter 2 outlines the full derivation of our theory from first principles. Section 2.3 details the numerical implementation and computational procedure utilised in this investigation. In Chapter 3 we present our results for a morphological study of the model diblock copolymer system. This is given in the form of a phase diagram where the three structures of Figure 1.1 and the disordered phase are identified in terms of the system parameters $\chi_{AB}r_C$ and f_A . The density profiles for several representative cases are also given. The generalisation to other systems, including those with solvent, is then discussed. Chapter 4 details the relationship between the lattice dimensions of the various morphologies and the parameters χ_{AB} and r_C for the model system in terms of a power law. The free energy density dependence is also illustrated, with analytic generalisations given for both. In Chapter 5 we summarise our investigation, the numerical results of which are tabulated in Appendix A. Finally, Appendix B illustrates how the theory can be extended to systems more complicated than the linear diblock case given here.

Chapter 2

Formalism

2.1 The Functional Integral Representation

We begin the construction of the model for our chemical system with the mathematical representation of a polymer chain. Addressing two adjacent monomer units within a chain, the bond lengths are assumed to have a Gaussian distribution [8] with the *rms* bond length, known as the Kuhn statistical bond length, given by b . The probability, ψ , of a bond being of length r is thus given by

$$\psi(r) = \left[\frac{3}{2\pi b^2}\right]^{3/2} \exp\left[-\frac{3r^2}{2b^2}\right], \quad (2.1)$$

which satisfies our Gaussian criteria. For a chain of Z monomers with their positions given by the set of vectors $\{\mathbf{R}_n\}$, the associated probability of the configuration will become

$$\begin{aligned} \Psi(\{\mathbf{R}_n\}) &= \prod_{n=1}^{Z-1} \psi(|\mathbf{R}_{n+1} - \mathbf{R}_n|) \\ &= \left[\frac{3}{2\pi b^2}\right]^{3(Z-1)/2} \exp\left[-\sum_{n=1}^{Z-1} \frac{3|\mathbf{R}_{n+1} - \mathbf{R}_n|^2}{2b^2}\right]. \end{aligned} \quad (2.2)$$

In our treatment we consider chains of high degree of polymerization. Thus, it is reasonable to consider the continuous limit of equation (2.2): [12]

$$P \propto \exp\left[-\frac{3}{2b^2} \int_0^Z d\tau \dot{\mathbf{r}}^2(\tau)\right], \quad (2.3)$$

where the polymer chain is represented by an arbitrary space-curve, $\mathbf{r}(\tau)$, parameterised by the monomer position along the chain, τ . Equation (2.3) is known as the Wiener measure.

With equation 2.3 as our underlying assumption, we construct the partition function applying the general approach of the Hong and Noolandi formalism. [17] Considering a system of \tilde{N}_C copolymer chains, we identify the two distinct chemical species of the chain as blocks A and B . Each block has associated with it a distinct Kuhn length, b_A or b_B . We also require the bulk number densities of each species, ρ_{0A} and ρ_{0B} . The partition function \mathbf{Z} is thus given by a functional integral [12] over all possible configurations for each Gaussian chain, weighted by the appropriate probabilities.

$$\begin{aligned} \mathbf{Z} = & \frac{\mathcal{Z}_C^{\tilde{N}_C}}{\tilde{N}_C!} \int \prod_{i=1}^{\tilde{N}_C} \delta \mathbf{r}_{A_i}(\cdot) \delta \mathbf{r}_{B_i}(\cdot) \times \\ & P_A[\mathbf{r}_{A_i}(\cdot)] P_B[\mathbf{r}_{B_i}(\cdot)] \times \\ & \delta[\mathbf{r}_{A_i}(Z_A) - \mathbf{r}_{B_i}(Z_B)] \times \\ & \prod_{\mathbf{r}} \delta \left[1 - \frac{\hat{\rho}_A(\mathbf{r})}{\rho_{0A}} - \frac{\hat{\rho}_B(\mathbf{r})}{\rho_{0B}} \right] \times \\ & \exp[-\beta \hat{V}(\cdot)], \end{aligned} \quad (2.4)$$

where \mathcal{Z}_C is the contribution to the partition function from the kinetic energy of the copolymer molecule. Each block κ of each polymer chain i is parameterised by a space-curve $\mathbf{r}_{\kappa i}(\cdot)$, where the dot denotes the fact that the curve is a function of the configuration. Note that $\delta \mathbf{r}_{\kappa i}(\cdot)$ represents a functional integration over all configurations of the space-curve, while $\delta[\dots]$ represents the Dirac delta functional. Equation (2.4) is in fact a simplified version of the partition function derived for the case of copolymer/solvent blends, [27] where the kinetic energy and configurational probabilities of the solvent are absent.

As we are concerned with copolymer molecules, where each block of species A is bonded to a complementary block of species B , this must be reflected in the permitted states in the partition function. This is accomplished by the δ function which appears in the third line of equation (2.4). Physically this factor requires that space-curves of the

A and B blocks terminate at a common coordinate.

The δ functional in the fourth line of the partition function represents the assumed incompressibility of the system. As this condition must be maintained at every spatial position, a δ functional factor must be included for each position \mathbf{r} . This is denoted by the $\prod_{\mathbf{r}}$ notation. The Hong and Noolandi partition function does not include this term. Instead they introduce incompressibility as a minimisation constraint in the saddle-function approximation (see Section 2.2). Following the approaches of Banaszak, [2] and Ohta and Kawasaki, [21] the variation used here is preferred in that all physical characteristics of the system are explicitly contained in the initial construction of the partition function, rather than being introduced later.

Considering the monomers to have no internal structure, the number densities appearing in this function are

$$\begin{aligned}\hat{\rho}_{\kappa}(\mathbf{r}) &= \hat{\rho}_{\kappa}(\mathbf{r}, \{\mathbf{r}_{\kappa i}\}) \\ &= \sum_{i=1}^{\tilde{N}_C} \int_0^{Z_{\kappa}} d\tau \delta[\mathbf{r} - \mathbf{r}_{\kappa i}(\tau)].\end{aligned}\quad (2.5)$$

The functional integral that defines \mathbf{Z} is weighted by a Wiener distribution for each chain and by a Boltzmann factor corresponding to the potential energy $\hat{V}(\cdot)$ of the system at a temperature $T = 1/k_B\beta$. This potential is due to the interaction between monomers and is a function of the monomer distributions $\hat{\rho}_{\kappa}(\cdot)$.

Equation (2.5) essentially represents a piecewise definition of the density distribution in terms of the individual pointlike monomers. We may replace this piecewise function with a continuous function, $\rho_{\kappa}(\cdot)$, through the identity,

$$\begin{aligned}\prod_{\mathbf{r}} \delta\left[1 - \frac{\hat{\rho}_A(\mathbf{r})}{\rho_{0A}} - \frac{\hat{\rho}_B(\mathbf{r})}{\rho_{0B}}\right] e^{-\beta\hat{V}[\{\hat{\rho}_{\kappa}(\cdot)\}]} &= \int \prod_{\kappa=A}^B \delta\rho_{\kappa}(\cdot) \delta[\rho_{\kappa}(\cdot) - \hat{\rho}_{\kappa}(\cdot)] \times \\ &\quad \prod_{\mathbf{r}} \delta\left[1 - \frac{\rho_A(\mathbf{r})}{\rho_{0A}} - \frac{\rho_B(\mathbf{r})}{\rho_{0B}}\right] e^{-\beta V[\{\rho_{\kappa}(\cdot)\}]}.\end{aligned}\quad (2.6)$$

In order to apply the saddle-function approximation, as is our goal in the mean field approach, we express the partition function in terms of a free energy. To this end, we express the δ functionals in terms of their Fourier transforms to obtain

$$\delta[\rho_\kappa(\cdot) - \hat{\rho}_\kappa(\cdot)] = \mathcal{N}_1 \int \delta\omega_\kappa(\cdot) \exp \left\{ \int d^3r \omega_\kappa(\mathbf{r}) [\rho_\kappa(\mathbf{r}) - \hat{\rho}_\kappa(\mathbf{r})] \right\}, \quad (2.7)$$

and

$$\prod_{\mathbf{r}} \delta \left[1 - \frac{\rho_A(\mathbf{r})}{\rho_{0A}} - \frac{\rho_B(\mathbf{r})}{\rho_{0B}} \right] = \mathcal{N}_2 \int \delta\eta(\cdot) \times \exp \left\{ \int d^3r \eta(\mathbf{r}) \left[1 - \frac{\rho_A(\mathbf{r})}{\rho_{0A}} - \frac{\rho_B(\mathbf{r})}{\rho_{0B}} \right] \right\}, \quad (2.8)$$

where the limits of integration on $\omega_\kappa(\mathbf{r})$ and $\eta(\mathbf{r})$ are $\pm i\infty$. All integrals of the form d^3r are over the volume of the system with \mathcal{N}_1 and \mathcal{N}_2 as normalisation constants. Substituting these identities into equation (2.4), the partition function becomes,

$$\begin{aligned} \mathbf{Z} &= \mathcal{N} \frac{Z_C^{\tilde{N}_C}}{\tilde{N}_C!} \times \\ &\int \delta\rho_A(\cdot) \delta\rho_B(\cdot) \delta\omega_A(\cdot) \delta\omega_B(\cdot) \delta\eta(\cdot) \times \\ &\exp \left\{ \int d^3r \eta(\mathbf{r}) \left[1 - \frac{\rho_A(\mathbf{r})}{\rho_{0A}} - \frac{\rho_B(\mathbf{r})}{\rho_{0B}} \right] \right\} \times \\ &\exp \left\{ \int d^3r [\omega_A(\mathbf{r})\rho_A(\mathbf{r}) + \omega_B(\mathbf{r})\rho_B(\mathbf{r})] \right\} \times \\ &Q_C^{\tilde{N}_C} e^{-\beta V[\{\rho_\kappa(\cdot)\}]}, \end{aligned} \quad (2.9)$$

where

$$\begin{aligned} Q_C^{\tilde{N}_C} &= \int \prod_{i=1}^{\tilde{N}_C} \delta\mathbf{r}_{Ai}(\cdot) \delta\mathbf{r}_{Bi}(\cdot) P_A[\mathbf{r}_{Ai}(\cdot)] P_B[\mathbf{r}_{Bi}(\cdot)] \times \\ &\delta[r_{Ai}(Z_A) - r_{Bi}(Z_B)] \times \\ &\exp \left\{ - \int d^3r [\omega_A(\mathbf{r})\hat{\rho}_A(\mathbf{r}) + \omega_B(\mathbf{r})\hat{\rho}_B(\mathbf{r})] \right\}. \end{aligned} \quad (2.10)$$

The normalisations of equations (2.7) and (2.8) are contained in \mathcal{N} . By substituting

equation (2.5) into the expression for Q_C above, we can simplify as follows:

$$Q_C^{\tilde{N}_C} = \int \prod_{i=1}^{\tilde{N}_C} \delta \mathbf{r}_{Ai}(\cdot) \delta \mathbf{r}_{Bi}(\cdot) P_A[\mathbf{r}_{Ai}(\cdot)] P_B[\mathbf{r}_{Bi}(\cdot)] \times \\ \delta[r_{Ai}(Z_A) - r_{Bi}(Z_B)] \times \\ \exp \left\{ - \sum_{i=1}^{\tilde{N}_C} \left\{ \int_0^{Z_A} d\tau \omega_A[\mathbf{r}_{Ai}(\tau)] + \int_0^{Z_B} d\tau \omega_B[\mathbf{r}_{Bi}(\tau)] \right\} \right\}. \quad (2.11)$$

In this form, one can explicitly see that the right-hand side of equation (2.11) can be expressed as the product of \tilde{N}_C identical factors, each given by

$$Q_C = \int \delta \mathbf{r}_A(\cdot) \delta \mathbf{r}_B(\cdot) P_A[\mathbf{r}_A(\cdot)] P_B[\mathbf{r}_B(\cdot)] \times \\ \delta[r_A(Z_A) - r_B(Z_B)] \times \\ \exp \left\{ - \int_0^{Z_A} d\tau \omega_A[\mathbf{r}_A(\tau)] - \int_0^{Z_B} d\tau \omega_B[\mathbf{r}_B(\tau)] \right\}. \quad (2.12)$$

This reflects the indistinguishability of the copolymer molecules, as was already implied by the chosen form of the kinetic energy term in the partition function.

Using traditional notation, this Q_C can be expressed in terms of a ‘‘propagator’’ function, [12] defined for each species κ as

$$Q_\kappa(\mathbf{R}, \tau | \mathbf{R}') = \int \delta \mathbf{r}_\kappa(\cdot) \delta[\mathbf{r}_\kappa(\tau) - \mathbf{R}] \delta[\mathbf{r}_\kappa(0) - \mathbf{R}'] \times \\ \exp \left\{ - \int_0^\tau d\tau' \left\{ \frac{3}{2b_\kappa^2} \dot{\mathbf{r}}^2(\tau') + \omega_\kappa[\mathbf{r}_\kappa(\tau')] \right\} \right\}. \quad (2.13)$$

Note that the constant of proportionality for the Wiener measure appearing in this expression is contained implicitly within the $\delta \mathbf{r}_\kappa(\cdot)$ factor. [12] This function has the property,

$$Q_\kappa(\mathbf{R}, \tau | \mathbf{R}') = Q_\kappa(\mathbf{R}', \tau | \mathbf{R}). \quad (2.14)$$

Conceptually, the propagator $Q_\kappa(\mathbf{R}, \tau | \mathbf{R}')$ is an integration over all configurations of a block’s space-curve which originate at $\mathbf{r}(0) = \mathbf{R}'$ and terminate at $\mathbf{r}(\tau) = \mathbf{R}$. The integrand is weighted by the probability of each configuration. Physically then, the

propagator may be interpreted as being proportional to the probability that a block starting at \mathbf{R}' will arrive at \mathbf{R} after τ monomer steps. This function can be shown to satisfy the diffusion equation, [12]

$$\left[\frac{b_\kappa^2}{6}\nabla^2 - \omega_\kappa(\mathbf{r})\right]Q_\kappa(\mathbf{r}, \tau|\mathbf{r}') = \frac{\partial}{\partial\tau}Q_\kappa(\mathbf{r}, \tau|\mathbf{r}'), \quad (2.15)$$

with the initial condition,

$$Q_\kappa(\mathbf{r}, 0|\mathbf{r}') = \delta(\mathbf{r} - \mathbf{r}'), \quad (2.16)$$

obtained from the definition. From equation (2.13), it follows directly that

$$\begin{aligned} Q_C &= \int d^3R_1 d^3R_2 d^3R_3 d^3R_4 \times \\ &\quad Q_A(\mathbf{R}_2, Z_A|\mathbf{R}_1)\delta(\mathbf{R}_2 - \mathbf{R}_4)Q_B(\mathbf{R}_4, Z_B|\mathbf{R}_3) \\ &= \int d^3R_1 d^3R_2 d^3R_3 Q_A(\mathbf{R}_2, Z_A|\mathbf{R}_1)Q_B(\mathbf{R}_2, Z_B|\mathbf{R}_3). \end{aligned} \quad (2.17)$$

The appearance of the diffusion equation can be understood through physical arguments. Referring back to the definition (2.2), the mean-squared separation of the initial and final monomers in the chain, \mathbf{R}_1 and \mathbf{R}_Z , can be shown to be $(Z-1)b_\kappa^2$. [8] This is the same result as for a random walk of step length b_κ . The Wiener measure is, in fact, a well-known representation of the probability distribution in Brownian motion, a random walk process. [8] The diffusion equation represents the continuous limit of a time-evolving random walk. [23] Thus, the propagator provides an accurate visualisation of a copolymer as a diffusive random walk process where the time variable is replaced by the monomer position along a polymer chain, τ , with the diffusion coefficient identified as b_κ^2 . We have assumed that the polymers interact, which biases this random walk. From (2.15), we recognise $\omega_\kappa(\mathbf{r})$ as the biasing potential for a species κ .

We now return to the partition function, which can be expressed as an integral of a free energy functional. That is, equation (2.9) may be rewritten as

$$\mathbf{Z} = \mathcal{N} \int \delta\rho_A(\cdot)\delta\rho_B(\cdot)\delta\omega_A(\cdot)\delta\omega_B(\cdot)\delta\eta(\cdot) \times$$

$$\exp \left\{ -\mathcal{F}[\{\rho_\kappa(\cdot)\}, \{\omega_\kappa(\cdot)\}, \eta(\cdot)] \right\}, \quad (2.18)$$

where the reduced free energy (expressed in units of $k_B T$) is given by

$$\begin{aligned} \mathcal{F}[\{\rho_\kappa(\cdot)\}, \{\omega_\kappa(\cdot)\}, \eta(\cdot)] &= -\tilde{N}_C \ln \mathcal{Z}_C + \ln \tilde{N}_C! - \tilde{N}_C \ln Q_C - \\ &\int d^3r \eta(\mathbf{r}) \left[1 - \frac{\rho_A(\mathbf{r})}{\rho_{0A}} - \frac{\rho_B(\mathbf{r})}{\rho_{0B}} \right] - \\ &\int d^3r [\omega_A(\mathbf{r})\rho_A(\mathbf{r}) + \omega_B(\mathbf{r})\rho_B(\mathbf{r})] + \\ &\beta V[\{\rho_\kappa(\cdot)\}]. \end{aligned} \quad (2.19)$$

Applying Stirling's approximation [23] to $\ln \tilde{N}_C!$ for a large numbers of copolymers, and combining all of the logarithmic terms, this becomes

$$\begin{aligned} \mathcal{F}[\{\rho_\kappa(\cdot)\}, \{\omega_\kappa(\cdot)\}, \eta(\cdot)] &= \tilde{N}_C \left(\ln \frac{\tilde{N}_C}{\mathcal{Z}_C Q_C} - 1 \right) - \\ &\int d^3r \eta(\mathbf{r}) \left[1 - \frac{\rho_A(\mathbf{r})}{\rho_{0A}} - \frac{\rho_B(\mathbf{r})}{\rho_{0B}} \right] - \\ &\int d^3r [\omega_A(\mathbf{r})\rho_A(\mathbf{r}) + \omega_B(\mathbf{r})\rho_B(\mathbf{r})] + \\ &\beta V[\{\rho_\kappa(\cdot)\}]. \end{aligned} \quad (2.20)$$

Thus, the copolymer system is now described by a partition function comprised of a functional integral over all configurations, weighted by the associated Boltzmann probability for the reduced free energy \mathcal{F} .

2.2 The Mean Field Approximation

Analogous to the saddle-point approximation, the saddle-function approximation is based on the supposition that there is a sharp maximum in the Boltzmann distribution $\exp[-\mathcal{F}]$ associated with a certain field configuration of $\rho_\kappa(\mathbf{r})$, $\omega_\kappa(\mathbf{r})$ and $\eta(\mathbf{r})$. This corresponds to a minimum in the free energy functional. This minimum can be located using the functional analysis equivalent to Lagrange multipliers, where we have a constraint reflecting the conservation of particle number for each species κ given by

$$\int d^3r \rho_\kappa(\mathbf{r}) = N_\kappa. \quad (2.21)$$

The functional Lagrange multiplier method identifies the minimum of \mathcal{F} with respect to a field configuration $\psi(\mathbf{r})$ as

$$\frac{\delta\mathcal{F}}{\delta\psi(\mathbf{r})} = \lambda_A \frac{\delta\mathcal{C}_A}{\delta\psi(\mathbf{r})} + \lambda_B \frac{\delta\mathcal{C}_B}{\delta\psi(\mathbf{r})}, \quad (2.22)$$

where \mathcal{C}_κ is the constraint surface, identified as the left-hand side of equation (2.21). Each λ_κ is a Lagrange multiplier. Thus, minimising equation (2.20) with respect to $\rho_\kappa(\mathbf{r})$, $\omega_\kappa(\mathbf{r})$, and $\eta(\mathbf{r})$ subject to the constraints, we obtain the relations

$$\frac{\eta(\mathbf{r})}{\rho_{0\kappa}} - \omega_\kappa(\mathbf{r}) + \frac{\delta}{\delta\rho_\kappa(\mathbf{r})} \beta V[\{\rho_\kappa(\cdot)\}] = \lambda_\kappa, \quad (2.23)$$

$$-\rho_\kappa(\mathbf{r}) - \frac{\tilde{N}_C}{Q_C} \frac{\delta Q_C}{\delta\omega_\kappa(\mathbf{r})} = 0, \quad (2.24)$$

$$1 - \frac{\rho_A(\mathbf{r})}{\rho_{0A}} - \frac{\rho_B(\mathbf{r})}{\rho_{0B}} = 0. \quad (2.25)$$

The first two of these are equations which can be solved for $\omega_\kappa(\mathbf{r})$ and $\rho_\kappa(\mathbf{r})$ and the last equation simply recovers the incompressibility condition.

Note that, via equation (2.12), Q_C is a function only of the fields $\omega_\kappa(\mathbf{r})$. Likewise the potential energy, V , is a function of only $\rho_\kappa(\mathbf{r})$. These conditions are reflected in the absence of $\delta V/\delta\eta(\mathbf{r})$ and similar terms from the above expressions.

Thus, in principle, we have a system of equations defining the most probable configuration of the copolymer system. We can show that, in the limit that $\exp[-\mathcal{F}]$ is sharply peaked, $\rho_\kappa(\mathbf{r})$ will correspond to the thermally averaged density distribution. This thermal average, $\langle \hat{\rho}_\kappa(\mathbf{r}) \rangle$, is most generally defined by a functional integral over all density configurations weighted by the appropriate probabilities. Referring to the initial definition of the partition function, equation (2.4), the normalisation of this probability is given by $\mathcal{Z}_C^{\tilde{N}_C} / \mathbf{Z}^{\tilde{N}_C!}$. Thus we have

$$\begin{aligned} \langle \hat{\rho}_\kappa(\mathbf{r}) \rangle = & \left(\frac{1}{\mathbf{Z}} \frac{\mathcal{Z}_C^{\tilde{N}_C}}{\tilde{N}_C!} \right) \int \prod_{i=1}^{\tilde{N}_C} \delta \mathbf{r}_{A_i}(\cdot) \delta \mathbf{r}_{B_i}(\cdot) \hat{\rho}_\kappa(\cdot) \times \\ & P_A[\mathbf{r}_{A_i}(\cdot)] P_B[\mathbf{r}_{B_i}(\cdot)] \times \\ & \delta[\mathbf{r}_{A_i}(Z_A) - \mathbf{r}_{B_i}(Z_B)] \times \\ & \prod_{\mathbf{r}} \delta \left[1 - \frac{\hat{\rho}_A(\mathbf{r})}{\rho_{0A}} - \frac{\hat{\rho}_B(\mathbf{r})}{\rho_{0B}} \right] \times \\ & \exp \left\{ -\beta \hat{V}[\{\rho_\kappa(\cdot)\}] \right\}. \end{aligned} \quad (2.26)$$

Applying the same steps used to transform the partition function into the form (2.18), the thermally averaged density can be written as

$$\begin{aligned} \langle \hat{\rho}_\kappa(\mathbf{r}) \rangle = & \frac{\mathcal{N}}{\mathbf{Z}} \int \delta \rho_A(\cdot) \delta \rho_B(\cdot) \delta \omega_A(\cdot) \delta \omega_B(\cdot) \delta \eta(\cdot) \times \\ & \rho_\kappa(\cdot) \exp \left\{ -\mathcal{F}[\{\rho_{\kappa'}(\cdot)\}, \{\omega_{\kappa'}(\cdot)\}, \eta(\cdot)] \right\} \end{aligned} \quad (2.27)$$

As this integral is weighted by the same Boltzmann factor, the dominant contribution to the thermal average must occur at the saddle-function. Thus, the thermal average density is approximated by the density distributions $\rho_\kappa(\mathbf{r})$ which define the minimum in the free energy functional, specified by equation (2.24).

Physically, the saddle-function represents the *mean field* of the system. From equations (2.23) through (2.25), we are now able to derive a set of self-consistent integrodifferential equations which can be solved to describe the physical system.

Before proceeding, however, we introduce an explicit form for the interaction potential energy, V , making two basic assumptions. First, we assume that only two-body interactions need be considered, as is conventionally the case. Explicitly, the total potential energy may be expressed in terms of this interaction as [17]

$$\beta V[\{\rho_\kappa(\cdot)\}] = \frac{1}{2} \sum_{\kappa=A}^B \sum_{\kappa'=A}^B \int d^3r d^3r' \rho_\kappa(\mathbf{r}) W_{\kappa\kappa'}(|\mathbf{r} - \mathbf{r}'|) \rho_{\kappa'}(\mathbf{r}'), \quad (2.28)$$

where $W_{\kappa\kappa'}(r)$ defines the potential acting on a monomer of species κ due to a monomer of species κ' at distance r . It is useful to define functions $U_{\kappa\kappa'}(r)$ in terms of these interaction potentials as [17]

$$U_{\kappa\kappa'}(r) = W_{\kappa\kappa'}(r) - \frac{1}{2} \frac{\rho_{0\kappa}}{\rho_{0\kappa'}} W_{\kappa\kappa}(r) - \frac{1}{2} \frac{\rho_{0\kappa'}}{\rho_{0\kappa}} W_{\kappa'\kappa'}(r). \quad (2.29)$$

For like monomers, where $\kappa = \kappa'$, this function reduces to

$$U_{\kappa\kappa}(r) = 0. \quad (2.30)$$

Substituting equation (2.29) into (2.28), we obtain

$$\begin{aligned} V[\{\rho_\kappa(\cdot)\}] &= \int d^3r d^3r' \rho_A(\mathbf{r}) U_{AB}(|\mathbf{r} - \mathbf{r}'|) \rho_B(\mathbf{r}') + \\ &\quad \frac{1}{4} \sum_{\kappa=A}^B \sum_{\kappa'=A}^B \int d^3r d^3r' \rho_\kappa(\mathbf{r}) \left[\frac{\rho_{0\kappa}}{\rho_{0\kappa'}} W_{\kappa\kappa}(|\mathbf{r} - \mathbf{r}'|) \right] \rho_{\kappa'}(\mathbf{r}') + \\ &\quad \frac{1}{4} \sum_{\kappa=A}^B \sum_{\kappa'=A}^B \int d^3r d^3r' \rho_\kappa(\mathbf{r}) \left[\frac{\rho_{0\kappa'}}{\rho_{0\kappa}} W_{\kappa'\kappa'}(|\mathbf{r} - \mathbf{r}'|) \right] \rho_{\kappa'}(\mathbf{r}'). \end{aligned} \quad (2.31)$$

By exchanging κ and κ' , one can readily see that the second and third terms in this expression are identical. Turning our attention to the evaluation of the second term in this equation,

$$\begin{aligned} &\sum_{\kappa=A}^B \sum_{\kappa'=A}^B \int d^3r d^3r' \rho_\kappa(\mathbf{r}) \left[\frac{\rho_{0\kappa}}{\rho_{0\kappa'}} W_{\kappa\kappa}(|\mathbf{r} - \mathbf{r}'|) \right] \rho_{\kappa'}(\mathbf{r}') \\ &= \sum_{\kappa=A}^B \int d^3r d^3r' \rho_\kappa(\mathbf{r}) \rho_{0\kappa} W_{\kappa\kappa}(|\mathbf{r} - \mathbf{r}'|) \left[\frac{\rho_A(\mathbf{r}')}{\rho_{0A}} + \frac{\rho_B(\mathbf{r}')}{\rho_{0B}} \right]. \end{aligned} \quad (2.32)$$

Applying the incompressibility condition (2.25), this simplifies to

$$\sum_{\kappa=A}^B \rho_{0\kappa} \int d^3r d^3r'' \rho_{\kappa}(\mathbf{r}) W_{\kappa\kappa}(r''). \quad (2.33)$$

Neglecting edge effects, this becomes

$$\rho_{0A} N_A W_{AA} + \rho_{0B} N_B W_{BB}, \quad (2.34)$$

where

$$W_{\kappa\kappa} = \int d^3r W_{\kappa\kappa}(r). \quad (2.35)$$

Thus, assuming two-body interactions, the potential energy becomes

$$\begin{aligned} \beta V[\{\rho_{\kappa}(\cdot)\}] &= \int d^3r d^3r' \rho_A(\mathbf{r}) U_{AB}(|\mathbf{r} - \mathbf{r}'|) \rho_B(\mathbf{r}') + \\ &\quad \frac{1}{2} \rho_{0A} N_A W_{AA} + \frac{1}{2} \rho_{0B} N_B W_{BB}, \end{aligned} \quad (2.36)$$

If we assume that these monomer interactions are short-range on the scale of the system, we can approximate the potential energy functional by the first two non-zero terms of the gradient expansion, [17]

$$\begin{aligned} \int d^3r d^3r' \rho_A(\mathbf{r}) U_{AB}(|\mathbf{r} - \mathbf{r}'|) \rho_B(\mathbf{r}') &= U_{AB}^{(1)} \int d^3r \rho_A(\mathbf{r}) \rho_B(\mathbf{r}) - \\ &\quad \frac{1}{6} U_{AB}^{(2)} \int d^3r \nabla \rho_A(\mathbf{r}) \cdot \nabla \rho_B(\mathbf{r}) + \\ &\quad \dots \end{aligned} \quad (2.37)$$

where $U_{AB}^{(n)}$ are expansion coefficients. Substituting this into the potential energy expression yields

$$\begin{aligned} \beta V[\{\rho_{\kappa}(\cdot)\}] &= \frac{\rho_{ref} \chi_{AB}}{\rho_{0A} \rho_{0B}} \left[\int d^3r \rho_A(\mathbf{r}) \rho_B(\mathbf{r}) - \frac{\sigma^2}{6} \int d^3r \nabla \rho_A(\mathbf{r}) \cdot \nabla \rho_B(\mathbf{r}) \right] + \\ &\quad \frac{1}{2} \rho_{0A} N_A W_{AA} + \frac{1}{2} \rho_{0B} N_B W_{BB}, \end{aligned} \quad (2.38)$$

where, by convention, [2] we have defined

$$\chi_{AB} \equiv \frac{\rho_{0A}\rho_{0B}}{\rho_{ref}} U_{AB}^{(1)}, \quad (2.39)$$

and

$$\sigma^2 \equiv \frac{U_{AB}^{(2)}}{U_{AB}^{(1)}}. \quad (2.40)$$

Here, χ_{AB} is the Flory interaction parameter and σ is designated the “effective range of the potential”. It should be noted that σ^2 need not necessarily be positive.

We now apply the mean-field equation (2.23) to the potential energy expression (2.38) to obtain expressions for the fields $\omega_\kappa(\mathbf{r})$:

$$\omega_A(\mathbf{r}) = \frac{\rho_{ref}}{\rho_{0A}} \left\{ \frac{\chi_{AB}}{\rho_{0B}} [\rho_B(\mathbf{r}) + \frac{\sigma^2}{6} \nabla^2 \rho_B(\mathbf{r})] + \frac{\eta(\mathbf{r})}{\rho_{ref}} \right\} - \lambda_A, \quad (2.41)$$

and

$$\omega_B(\mathbf{r}) = \frac{\rho_{ref}}{\rho_{0B}} \left\{ \frac{\chi_{AB}}{\rho_{0A}} [\rho_A(\mathbf{r}) + \frac{\sigma^2}{6} \nabla^2 \rho_A(\mathbf{r})] + \frac{\eta(\mathbf{r})}{\rho_{ref}} \right\} - \lambda_B. \quad (2.42)$$

It now remains to obtain the density distributions from equation (2.24). We calculate these in terms of the normalised local volume fractions,

$$\phi_\kappa(\mathbf{r}) \equiv \frac{\rho_\kappa(\mathbf{r})}{\rho_{0\kappa}}, \quad (2.43)$$

which leads to the restatement of the incompressibility condition (2.25) as $\phi_A(\mathbf{r}) + \phi_B(\mathbf{r}) = 1$.

In terms of the local volume fraction, then, we combine equations (2.17), (2.24), and (2.43) to arrive at

$$\phi_\kappa(\mathbf{r}) = -\frac{\tilde{N}_C}{\rho_{0\kappa} Q_C} \int d^3 R_1 d^3 R_2 d^3 R_3 \times \frac{\delta}{\delta \omega_\kappa(\mathbf{r})} [Q_A(\mathbf{R}_2, Z_A | \mathbf{R}_1) Q_B(\mathbf{R}_2, Z_B | \mathbf{R}_3)]. \quad (2.44)$$

From (2.13) it is clear that $Q_\kappa(\mathbf{r}, \tau|\mathbf{r}')$ will be a function only of the corresponding $\omega_\kappa(\mathbf{r})$.

Taking as an example, $\kappa = A$,

$$\begin{aligned}
Q_A(\mathbf{R}_2, Z_A|\mathbf{R}_1) &= \int \delta\mathbf{r}_A(\cdot) \delta[\mathbf{r}_A(0) - \mathbf{R}_1] \delta[\mathbf{r}_A(Z_A) - \mathbf{R}_2] \times \\
&\quad \exp \left\{ - \int_0^{Z_A} d\tau' \left\{ \frac{3}{2b_A^2} \dot{\mathbf{r}}_A^2(\tau') + \omega_A[\mathbf{r}_A(\tau')] \right\} \right\} \\
&= \int \delta\mathbf{r}_A(\cdot) \delta[\mathbf{r}_A(0) - \mathbf{R}_1] \delta[\mathbf{r}_A(Z_A) - \mathbf{R}_2] \times \\
&\quad \exp \left\{ - \int_0^{Z_A} d\tau' \left\{ \frac{3}{2b_A^2} \dot{\mathbf{r}}_A^2(\tau') + \right. \right. \\
&\quad \left. \left. \int d^3r \omega_A(\mathbf{r}) \delta[\mathbf{r}_A(\tau') - \mathbf{r}] \right\} \right\}. \quad (2.45)
\end{aligned}$$

Thus, calculating the functional derivative,

$$\begin{aligned}
\frac{\delta Q_A}{\delta \omega_A(\mathbf{r})} &= - \int_0^{Z_A} d\tau \int \delta\mathbf{r}_A(\cdot) \delta[\mathbf{r}_A(\tau) - \mathbf{r}] \delta[\mathbf{R}_1 - \mathbf{r}_A(0)] \delta[\mathbf{R}_2 - \mathbf{r}_A(Z_A)] \times \\
&\quad \exp \left\{ - \int_0^{Z_A} d\tau' \left\{ \frac{3}{2b_A^2} \dot{\mathbf{r}}_A^2(\tau') + \omega_A[\mathbf{r}_A(\tau')] \right\} \right\}. \quad (2.46)
\end{aligned}$$

We separate this into two separate functional integrals, coupled by the Dirac delta function $\delta[\mathbf{r}_A(\tau) - \mathbf{R}']$, where \mathbf{R}' is integrated over all space:

$$\begin{aligned}
\frac{\delta Q_A}{\delta \omega_A(\mathbf{r})} &= - \int_0^{Z_A} d\tau \int d^3R' \delta(\mathbf{r} - \mathbf{R}') \times \\
&\quad \left\{ \int \delta\mathbf{r}_A(\cdot) \delta[\mathbf{r}_A(\tau) - \mathbf{r}] \delta[\mathbf{R}_1 - \mathbf{r}_A(0)] \times \right. \\
&\quad \left. \exp \left\{ - \int_0^\tau d\tau' \left\{ \frac{3}{2b_A^2} \dot{\mathbf{r}}_A^2(\tau') + \omega_A[\mathbf{r}_A(\tau')] \right\} \right\} \right\} \times \\
&\quad \left\{ \int \delta\mathbf{r}_A(\cdot) \delta[\mathbf{r}_A(\tau) - \mathbf{R}'] \delta[\mathbf{R}_2 - \mathbf{r}_A(Z_A)] \times \right. \\
&\quad \left. \exp \left\{ - \int_\tau^{Z_A} d\tau' \left\{ \frac{3}{2b_A^2} \dot{\mathbf{r}}_A^2(\tau') + \omega_A[\mathbf{r}_A(\tau')] \right\} \right\} \right\}. \quad (2.47)
\end{aligned}$$

The equivalence to equation (2.46) can be seen by noting that the only permitted contributions are those where $\mathbf{r}(\tau)$ in each functional integral corresponds to the same \mathbf{R}' . This is integrated over all space \mathbf{R}' and all monomers τ to establish a correspondence between the entire space-curve in each integral. In this form, the factor forming the

second and third lines of this expression can be recognised as $Q_A(\mathbf{r}, \tau | \mathbf{R}_1)$. The fourth and fifth lines are also analogous to the definition of the propagator, being proportional to the probability of monomer τ in the chain being located at \mathbf{R}' with monomer Z_A being located at \mathbf{R}_2 . Since the monomers are indistinguishable within the block, any interval spanning the same number of monomers should give the same probability. Choosing an interval starting at monomer 0 and ending at $Z_A - \tau$, we see that this factor is equivalent to $Q_A(\mathbf{R}_2, Z_A - \tau | \mathbf{R}')$, or $Q_A(\mathbf{R}', Z_A - \tau | \mathbf{R}_2)$ by the symmetry relation (2.14). Thus, equation (2.47) reduces to

$$\begin{aligned} \frac{\delta Q_A}{\delta \omega_A(\mathbf{r})} &= - \int_0^{Z_A} d\tau \int d^3 R' \delta(\mathbf{r} - \mathbf{R}') Q_A(\mathbf{r}, \tau | \mathbf{R}_1) Q_A(\mathbf{R}', Z_A - \tau | \mathbf{R}_2) \\ &= - \int_0^{Z_A} d\tau Q_A(\mathbf{r}, \tau | \mathbf{R}_1) Q_A(\mathbf{r}, Z_A - \tau | \mathbf{R}_2). \end{aligned} \quad (2.48)$$

Substituting this into equation (2.44), we obtain

$$\begin{aligned} \phi_A(\mathbf{r}) &= \frac{\bar{\phi}_A}{Z_A} \frac{\Omega}{Q_C} \int_0^{Z_A} d\tau \int d^3 R_1 d^3 R_2 d^3 R_3 Q_A(\mathbf{r}, \tau | \mathbf{R}_1) \times \\ &\quad Q_A(\mathbf{r}, Z_A - \tau | \mathbf{R}_2) Q_B(\mathbf{R}_2, Z_B | \mathbf{R}_3), \end{aligned} \quad (2.49)$$

where we have used the relation

$$\frac{Z_\kappa}{\rho_{0\kappa}} = \frac{\Omega \bar{\phi}_\kappa}{\tilde{N}_C}, \quad (2.50)$$

for a system of volume Ω to eliminate \tilde{N}_C . Equation (2.50) simply equates two expressions for the volume of a single block κ . An entirely analogous derivation provides us with the expression for $\phi_B(\mathbf{r})$,

$$\begin{aligned} \phi_B(\mathbf{r}) &= \frac{\bar{\phi}_B}{Z_B} \frac{\Omega}{Q_C} \int_0^{Z_B} d\tau \int d^3 R_1 d^3 R_2 d^3 R_3 Q_B(\mathbf{r}, \tau | \mathbf{R}_1) \times \\ &\quad Q_B(\mathbf{r}, Z_B - \tau | \mathbf{R}_2) Q_A(\mathbf{R}_2, Z_B | \mathbf{R}_3). \end{aligned} \quad (2.51)$$

We now have, in principle, a complete set of self-consistent equations. All quantities

appearing in them have a clear physical interpretation except for λ_κ . It is fairly straightforward, however, to demonstrate that the λ_κ terms do not affect the solution for the density distributions.

Referring to the diffusion equation (2.15), one can readily show that, if $Q_\kappa(\mathbf{r}, \tau|\mathbf{r}')$ is the solution corresponding to a given $\omega_\kappa(\mathbf{r})$, then adding a constant c_κ to the potential will give a new solution $Q'_\kappa(\mathbf{r}, \tau|\mathbf{r}') = e^{-c_\kappa\tau}Q_\kappa(\mathbf{r}, \tau|\mathbf{r}')$. This gives a new $Q'_C = e^{-c_A Z_A - c_B Z_B}Q_C$. Using Q'_C and $Q'_\kappa(\mathbf{r}, \tau|\mathbf{r}')$ in equations (2.49) and (2.51), we see that the resultant $\phi_\kappa(\mathbf{r})$ is unchanged. Thus, the density distributions are unchanged for any arbitrary additive constant in either potential.

Taking advantage of this property, we add $\lambda_\kappa - \chi_{AB}\bar{\phi}_\kappa\rho_{ref}/\rho_{0\kappa}$ to each potential to obtain,

$$\omega_A(\mathbf{r}) = \frac{\rho_{ref}}{\rho_{0A}} \left\{ \chi_{AB}[\phi_B(\mathbf{r}) - \bar{\phi}_B + \frac{\sigma^2}{6}\nabla^2\phi_B(\mathbf{r})] + \frac{\eta(\mathbf{r})}{\rho_{ref}} \right\}, \quad (2.52)$$

and

$$\omega_B(\mathbf{r}) = \frac{\rho_{ref}}{\rho_{0B}} \left\{ \chi_{AB}[\phi_A(\mathbf{r}) - \bar{\phi}_A + \frac{\sigma^2}{6}\nabla^2\phi_A(\mathbf{r})] + \frac{\eta(\mathbf{r})}{\rho_{ref}} \right\}. \quad (2.53)$$

This constant is chosen so that $\omega_\kappa(\mathbf{r})$ will reduce to zero for the case of homogeneous volume fraction distributions (i.e., $\phi_\kappa(\mathbf{r}) = \bar{\phi}_\kappa$). The choice of $\eta(\mathbf{r})$ is similarly arbitrary to within an additive constant, permitting its contribution to be zero in this case of homogeneous distribution.

It should be noted that, in the prior treatment of copolymer/solvent blends, [3, 28, 29] the function $\eta(\mathbf{r})$ had an explicit form in terms of the solvent density, $\bar{\phi}_S(\mathbf{r}) \equiv 1 - \bar{\phi}_A(\mathbf{r}) - \bar{\phi}_B(\mathbf{r})$. [27] Specifically, in that case it was found that $\eta(\mathbf{r}) = \ln[\bar{\phi}_S/\phi_S(\mathbf{r})]$. Though the initial partition function in our present case is conceptually simpler, the absence of such an explicit expression in this formalism adds a new degree of complexity to the problem. In both this and the prior treatment, $\eta(\mathbf{r})$ is determined by the incompressibility condition. Thus, in our current problem, $\eta(\mathbf{r})$ must be implicitly specified by $\phi_A(\mathbf{r}) + \phi_B(\mathbf{r}) = 1$.

In our investigation, we examine and compare the three morphologies shown in Figure 1.1. To predict the equilibrium structure for a given system, we must calculate its free energy density. The morphology with the lowest free energy will correspond to this equilibrium structure.

The expression for this free energy density is obtained by substituting equation (2.38) for the potential energy and equation (2.25) for the incompressibility into the expression (2.20):

$$\begin{aligned} \frac{f}{k_B T} &\equiv \frac{\mathcal{F}}{\Omega} \\ &= \frac{\tilde{N}_C}{\Omega} \left(\ln \frac{\tilde{N}_C}{\mathcal{Z}_C Q_C} - 1 \right) + \\ &\quad \frac{1}{\Omega} \int d^3 r \left\{ \rho_{ref} \chi_{AB} [\phi_A(\mathbf{r}) \phi_B(\mathbf{r}) - \frac{\sigma^2}{6} \nabla \phi_A(\mathbf{r}) \cdot \nabla \phi_B(\mathbf{r})] - \right. \\ &\quad \left. \rho_{0A} \omega_A(\mathbf{r}) \phi_A(\mathbf{r}) - \rho_{0B} \omega_B(\mathbf{r}) \phi_B(\mathbf{r}) \right\}. \end{aligned} \quad (2.54)$$

It is convenient to express this free energy relative to some reference configuration. Choosing the homogeneous phase as this reference, the free energy density of this state is

$$\begin{aligned} \frac{f_{hom}}{k_B T} &= \frac{\tilde{N}_C}{\Omega} \left(\ln \frac{\tilde{N}_C}{\mathcal{Z}_C \Omega} - 1 \right) + \\ &\quad \frac{1}{\Omega} \int d^3 r \rho_{ref} \chi_{AB} \bar{\phi}_A \bar{\phi}_B, \end{aligned} \quad (2.55)$$

where we recognise that $\omega_\kappa(\mathbf{r}) = 0$ for this state leads, through the solution of the diffusion equation and equation (2.17), to the conclusion that $Q_C = \Omega$. Thus, defining a free energy density relative to the homogeneous distribution, $\Delta f = f - f_{hom}$, we have

$$\begin{aligned} \frac{\Delta f}{\rho_{ref} k_B T} &= \frac{f - f_{hom}}{\rho_{ref} k_B T} \\ &= \frac{1}{\Omega} \int d^3 r \left\{ \chi_{AB} [\phi_A(\mathbf{r}) \phi_B(\mathbf{r}) - \bar{\phi}_A \bar{\phi}_B - \frac{\sigma^2}{6} \nabla \phi_A(\mathbf{r}) \cdot \nabla \phi_B(\mathbf{r})] - \right. \\ &\quad \left. \frac{\rho_{0A}}{\rho_{ref}} \omega_A(\mathbf{r}) \phi_A(\mathbf{r}) - \frac{\rho_{0B}}{\rho_{ref}} \omega_B(\mathbf{r}) \phi_B(\mathbf{r}) \right\} - \frac{1}{r_C} \ln \frac{Q_C}{\Omega}, \end{aligned} \quad (2.56)$$

where $1/r_C$ can be identified as $\tilde{N}_C/\rho_{ref}\Omega$.

In summary, we have arrived at a set of self-consistent equations describing our system through the use of the following assumptions:

1. The bond length between adjacent monomers in the copolymer chain are assumed to have a Gaussian distribution, with blocks A and B having Kuhn statistical bond lengths of b_A and b_B respectively.
2. The degrees of polymerization of each block, Z_A and Z_B , are assumed to be large so that the chain may be approximated as a continuous space-curve.
3. The system is assumed to be incompressible.
4. The number of copolymers in the system, \tilde{N}_C , is assumed to be large leading to the Stirling approximation of $\ln \tilde{N}_C!$
5. The thermally averaged density distributions of the monomer species are approximated by the system configuration of highest probability. This is the mean field approximation.
6. The potential energy of the system has been restricted to include only contributions from two-body interactions.
7. The two-body interaction is assumed to act over a finite range, being negligible for large monomer separations.

In this model, the copolymer system is entirely represented by the parameters Z_A , Z_B , χ_{AB} , b_A , b_B , ρ_{0A} , ρ_{0B} , and σ . The parameters $\bar{\phi}_A$ and $\bar{\phi}_B$ do not represent independent variables as they are simply functions of those above through (1.4). From these parameters, equations (2.15), (2.16), (2.17), (2.25), (2.49), (2.51), (2.52), and (2.53) represent a

closed set of self-consistent equations which, when solved, describe the approximate thermal average distributions of each monomer type. The associated free energy (2.56), which we calculate from the converged solutions, allows us to compare the various solutions of this system and predict the equilibrium structure.

2.3 Method of Numerical Solution

In principle, the set of equations describing the system should be solvable numerically using the relaxation method of self-consistent iteration. [22] A major source of difficulty arises, however, due to the presence of a singularity in the form of the initial conditions for the diffusion equation, the delta function (2.16). We can circumvent this, however, by defining four new functions,

$$q_\kappa(\mathbf{r}, \tau) = \int d^3r' Q_\kappa(\mathbf{r}, \tau|\mathbf{r}'), \quad (2.57)$$

and

$$q'_A(\mathbf{r}, \tau) = \int d^3r' Q_A(\mathbf{r}, \tau|\mathbf{r}')q_B(\mathbf{r}', Z_B), \quad (2.58)$$

$$q'_B(\mathbf{r}, \tau) = \int d^3r' Q_B(\mathbf{r}, \tau|\mathbf{r}')q_A(\mathbf{r}', Z_A). \quad (2.59)$$

In terms of these functions, Q_C and $\phi_\kappa(\mathbf{r})$ become, through direct substitution,

$$Q_C = \int d^3r q_A(\mathbf{r}, Z_A)q_B(\mathbf{r}, Z_B), \quad (2.60)$$

and

$$\phi_\kappa(\mathbf{r}) = \frac{\bar{\phi}_\kappa}{Z_\kappa} \frac{\Omega}{Q_C} \int_0^{Z_\kappa} d\tau q_\kappa(\mathbf{r}, \tau)q'_\kappa(\mathbf{r}, Z_\kappa - \tau). \quad (2.61)$$

In both $q_\kappa(\mathbf{r}, \tau)$ and $q'_\kappa(\mathbf{r}, \tau)$, a dependence on \mathbf{r} and τ appears only in a single $Q_\kappa(\mathbf{r}, \tau|\mathbf{r}')$ factor. Thus, $q_\kappa(\mathbf{r}, \tau)$ and $q'_\kappa(\mathbf{r}, \tau)$ satisfy the same diffusion equation as the propagator for species κ . The initial conditions for these equations are easily determined by substituting the delta function (2.16) into the definitions above. Doing this, we obtain

$$q_\kappa(\mathbf{r}, 0) = 1, \quad (2.62)$$

and

$$q'_A(\mathbf{r}, 0) = q_B(\mathbf{r}, Z_B), \quad (2.63)$$

$$q'_B(\mathbf{r}, 0) = q_A(\mathbf{r}, Z_A). \quad (2.64)$$

The diffusion equations for these functions contain no singularities and are readily solvable using numerical methods.

Physically, one can interpret $q_\kappa(\mathbf{r}, \tau)$, from equation (2.57) as being proportional to the probability of finding a monomer τ steps from the free end of the block at a position \mathbf{r} . Likewise, $q'_\kappa(\mathbf{r}, \tau)$ is the probability of finding a monomer, τ steps from the join between the two blocks, at \mathbf{r} . Consistent with the requirement that, for a copolymer, one must arrive at the same position for a given monomer regardless of the direction of approach along the chain, the expression for each density profile contains a product of these two probabilities, and includes an integration over all monomers in the block. Thus, Q_C represents the normalisation of this probability.

As we have already discussed, the field $\eta(\mathbf{r})$ appears because of the incompressibility condition $\phi_A(\mathbf{r}) + \phi_B(\mathbf{r}) = 1$. However, no explicit expression for $\eta(\mathbf{r})$ has yet been derived. This is necessary, however, in order to devise an iteration procedure and obtain converged solutions. By adding equations (2.52) and (2.53) and applying the incompressibility condition, we can solve for $\eta(\mathbf{r})$ to obtain

$$\eta(\mathbf{r}) = \frac{1}{2}[\rho_{0A}\omega_A(\mathbf{r}) + \rho_{0B}\omega_B(\mathbf{r})]. \quad (2.65)$$

This equation is only satisfied when the incompressibility condition is maintained. We now have the required number of independent equations to obtain a closed solution for the associated fields.

The solution of the diffusion equation in multiple dimensions is a formidable task. Therefore, we approximated the Wigner-Seitz unit cell of the hexagonal and *bcc* lattices by a cylinder or sphere respectively. [19] The resulting symmetry gives a solution which depends only on the radial coordinate and τ . The layered structure already has this property, and so, for all morphologies, the problem is reduced to one dimension. All

<i>Structure</i>	<i>m</i>	$\alpha_m(r)$
Layers	1	1
Cylinders	2	$2\pi r$
Spheres	3	$4\pi r^2$

Table 2.1: Weight function for an integral of m dimensions.

integrals of some arbitrary function $\psi(r, \tau)$ reduce to

$$\int d^m r \psi(r, \tau) = \int_0^R \alpha_m(r) dr \psi(r, \tau), \quad (2.66)$$

where each $\alpha_m(r)$ is the appropriate weighting function for a structure of m dimensions, as listed in Table 2.1. In the case of cylinders or spheres, R designates the radius of the approximated unit cell. For layers it is equivalent to the repeat distance d as illustrated in Figure 1.1(a). In terms of this effective lattice parameter, R , the volume of an m -dimensional cell is given by

$$\Omega = R\alpha_m(R)/m. \quad (2.67)$$

The angular dependence of the diffusion equation disappears in this symmetry leaving

$$\left[\frac{b_\kappa^2}{6} \left(\frac{\partial^2}{\partial r^2} + \frac{m-1}{r} \frac{\partial}{\partial r} \right) - \omega_\kappa(r) \right] q_\kappa(r, \tau) = \frac{\partial}{\partial \tau} q_\kappa(r, \tau), \quad (2.68)$$

with an identical form for $q'_\kappa(r, \tau)$.

To perform the actual numerical computation, the integrals, as well as the diffusion equation, must be discretised. For this investigation, we have discretised the distance variable r into $N_r = 100$ intervals, and monomer step variable τ_κ into $N_\tau = 400$ intervals. The width of each interval is thus $\Delta r = R/N_r$ and $\Delta \tau_\kappa = Z_\kappa/N_\tau$. Integrals were approximated to fourth order by Simpson's Rule as [22]

$$\begin{aligned}
\int_0^R \alpha_m(r) dr \psi(r, \tau) = & \Delta r \left\{ \frac{17}{48} \alpha_m(0) \psi_{0j} + \frac{59}{48} \alpha_m(\Delta r) \psi_{1j} + \right. \\
& \frac{43}{48} \alpha_m(2\Delta r) \psi_{2j} + \frac{49}{48} \alpha_m(3\Delta r) \psi_{3j} + \sum_{i=4}^{N_r-4} \alpha_m(i\Delta r) \psi_{ij} + \\
& \frac{49}{48} \alpha_m[(N_r-3)\Delta r] \psi_{N_r-3j} + \frac{43}{48} \alpha_m[(N_r-2)\Delta r] \psi_{N_r-2j} + \\
& \left. \frac{59}{48} \alpha_m[(N_r-1)\Delta r] \psi_{N_r-1j} + \frac{17}{48} \alpha_m(N_r\Delta r) \psi_{N_rj} \right\}, \quad (2.69)
\end{aligned}$$

and

$$\begin{aligned}
\int_0^{Z_\kappa} d\tau \psi(r, \tau) = & \Delta \tau_\kappa \left[\frac{17}{48} \psi_{i0} + \frac{59}{48} \psi_{i1} + \frac{43}{48} \psi_{i2} + \frac{49}{48} \psi_{i3} + \sum_{j=4}^{N_r-4} \psi_{ij} + \right. \\
& \left. \frac{49}{48} \psi_{i(N_r-3)} + \frac{43}{48} \psi_{i(N_r-2)} + \frac{59}{48} \psi_{i(N_r-1)} + \frac{17}{48} \psi_{iN_r} \right]. \quad (2.70)
\end{aligned}$$

where $\psi_{ij} = \psi(i\Delta r, j\Delta \tau_\kappa)$.

The diffusion equation was discretised, using the Crank-Nicholson method, [10] as

$$\begin{aligned}
& \frac{b_\kappa^2}{6} \left[\frac{1}{2} \left(\frac{\psi_{i+1j+1} - 2\psi_{ij+1} + \psi_{i-1j+1}}{(\Delta r)^2} + \frac{\psi_{i+1j} - 2\psi_{ij} + \psi_{i-1j}}{(\Delta r)^2} \right) + \right. \\
& \left. \frac{m}{i\Delta r} \frac{1}{2} \left(\frac{\psi_{i+1j+1} - \psi_{i-1j+1}}{2\Delta r} + \frac{\psi_{i+1j} - \psi_{i-1j}}{2\Delta r} \right) \right] - \omega_i \frac{\psi_{ij+1} + \psi_{ij}}{2} \\
& = \frac{\psi_{ij+1} - \psi_{ij}}{\Delta \tau}. \quad (2.71)
\end{aligned}$$

Collecting ψ terms of like subscripts, this can be rewritten as

$$\begin{aligned}
& \psi_{i-1j+1}[F - G_i] + \psi_{ij+1}[-1 - 2F - \frac{1}{2}\omega_i\Delta\tau] + \psi_{i+1j+1}[F + G_i] + \\
& \psi_{i-1j}[-F + G_i] + \psi_{ij}[-1 + 2F + \frac{1}{2}\omega_i\Delta\tau] + \psi_{i+1j}[-F - G_i] \\
& = 0, \quad (2.72)
\end{aligned}$$

where

$$F = \frac{b_\kappa^2 \Delta \tau}{12(\Delta r)^2}, \quad (2.73)$$

and

$$G_i = \frac{b_\kappa^2 m \Delta \tau}{24(\Delta r)^2 i} \quad \text{for } i \neq 0. \quad (2.74)$$

To enforce continuity, $\partial\psi/\partial r$ must vanish at $r = 0$ for all structures. It therefore follows that $G_0 = 0$. This defines a series of linear equations which can be solved to give ψ_{ij+1} in terms of ψ_{ij} for all i . The corresponding matrix for this system is represented by

$$B_0\psi_{0j+1} + (A_0 + C_0)\psi_{1j+1} = D_{0j} \quad (2.75)$$

$$A_i\psi_{i-1j+1} + B_i\psi_{ij+1} + C_i\psi_{i+1j+1} = D_{ij} \quad \text{for } 0 < i < N_r, \quad (2.76)$$

$$(A_{N_r} + C_{N_r})\psi_{N_r-1j+1} + B_{N_r}\psi_{N_rj+1} = D_{N_rj} \quad (2.77)$$

where

$$A_i = F - G_i, \quad (2.78)$$

$$B_i = -1 - 2F - \frac{1}{2}\omega_i\Delta\tau, \quad (2.79)$$

$$C_i = F + G_i, \quad (2.80)$$

and

$$D_{ij} = \psi_{i-1j}[-F + G_i] + \psi_{ij}[-1 + 2F + \frac{1}{2}\omega_i\Delta\tau] + \psi_{i+1j}[-F - G_i]. \quad (2.81)$$

This is a tridiagonal form and is known to have a simple method of solution which can be implemented computationally. [22] Note that equations (2.78) and (2.80) establish “mirrored” boundary conditions which guarantee continuity of ψ and $\partial\psi/\partial r$ on the boundaries between cells as Δr goes to zero.

Having established the numerical discretisation for our system of equations, we briefly outline the iterative process of solution: [28]

1. Given a specific set of system parameters χ_{AB} , Z_A , Z_B , b_A , b_B , ρ_{0A} , ρ_{0B} , and σ to solve for a structure of dimension m , we choose some arbitrary initial value for R .

2. As a first approximation, we set $\eta^{(0)}(r) = 0$ and choose a trial $\phi_{\kappa}^{(0)}(r)$ with a hyperbolic tangent profile. This is in qualitative agreement with Figure 1.1 where we have allowed for a limited degree of intermixing. It should be stressed that this is not an assumption on the form of $\phi_{\kappa}(r)$, as it is merely a starting point which is revised and refined through successive iterations.
3. From these functions, we construct the two trial potentials $\omega_{\kappa}^{(0)}(r)$ via equations (2.52) and (2.53).
4. Using the potentials $\omega_{\kappa}^{(n)}(r)$ we solve the diffusion equations for $q_{\kappa}^{(n+1)}(r, \tau)$ and $q'_{\kappa}^{(n+1)}(r, \tau)$. These solutions are then used to construct new volume fraction distributions, $\phi_{\kappa}^{(n+1)}(r)$ via equation (2.61).
5. The potentials $\omega_{\kappa}^{(n)}(r)$ are also used to construct a new $\eta^{(n+1)}(r)$ field via equation (2.65).
6. Potentials $\omega'_{\kappa}(r)$ are constructed using $\phi_{\kappa}^{(n+1)}(r)$ and $\eta^{(n+1)}(r)$.
7. New potentials $\omega_{\kappa}^{(n+1)}(r)$ are calculated using linear combinations of the previous $\omega_{\kappa}^{(i)}(r)$ solutions and the new solution $\omega'_{\kappa}(r)$.
8. If, for some preselected convergence parameter, δ , the condition

$$|\omega_{\kappa}^{(n+1)}(r) - \omega_{\kappa}^{(n)}(r)| < \delta$$

is violated for any r , we return to step 4 and iterate. When this is satisfied for all r , the fields have converged to a self-consistent solution. For our calculations, we have chosen $\delta = 10^{-7}$.

9. Having obtained the $\phi_{\kappa}(r)$ and $\omega_{\kappa}(r)$ fields associated with our chosen parameters, we evaluate the free energy density. We then increment R by some suitable step,

after which the process is repeated starting with step 2, until the R that minimises the free energy density is found.

Figure 2.1 illustrates this process for a sample system with parameters $b_A = b_B$, $\rho_{0A} = \rho_{0B} = \rho_{ref}$, $Z_A = 314$, $Z_B = 186$, and $\chi_{AB} = 0.04$. In it, the free energy density, Δf , has been plotted as a function of repeat distance, with a minimum evident at $d/b = 36.4$ where b is the Kuhn length. Each point on this free energy curve represents a converged solution obtained after several thousand iterations of steps 1 through 8. In this example, the free energy density was sampled over the range of $d/b = 34.6$ to 36.6 , in increments of 0.02 , as described in step 9. For all systems investigated, only one minimum was found and so the lattice parameter was uniquely determined for each system.

The numerical methods discuss here are, in fact, a revision to the original approach. In previous work, [28] the boundary conditions specified that the functions $q_\kappa(r, \tau)$ and $q'_\kappa(r, \tau)$ be constant within a distance of Δr of the cell boundaries in order to enforce continuity. This assumption was found to give results which were inconsistent with previous limits [16, 20] for asymmetric copolymers. Thus, the “mirrored” boundary conditions were chosen here as a suitable alternative with associated modifications to the evaluation of the free energy. Similarly, Riemann sums for numerical integration were replaced by Simpson’s Rule, thereby attaining three additional orders of accuracy. The iterative procedure was also automated as much as possible due to the magnitude of the calculations performed.

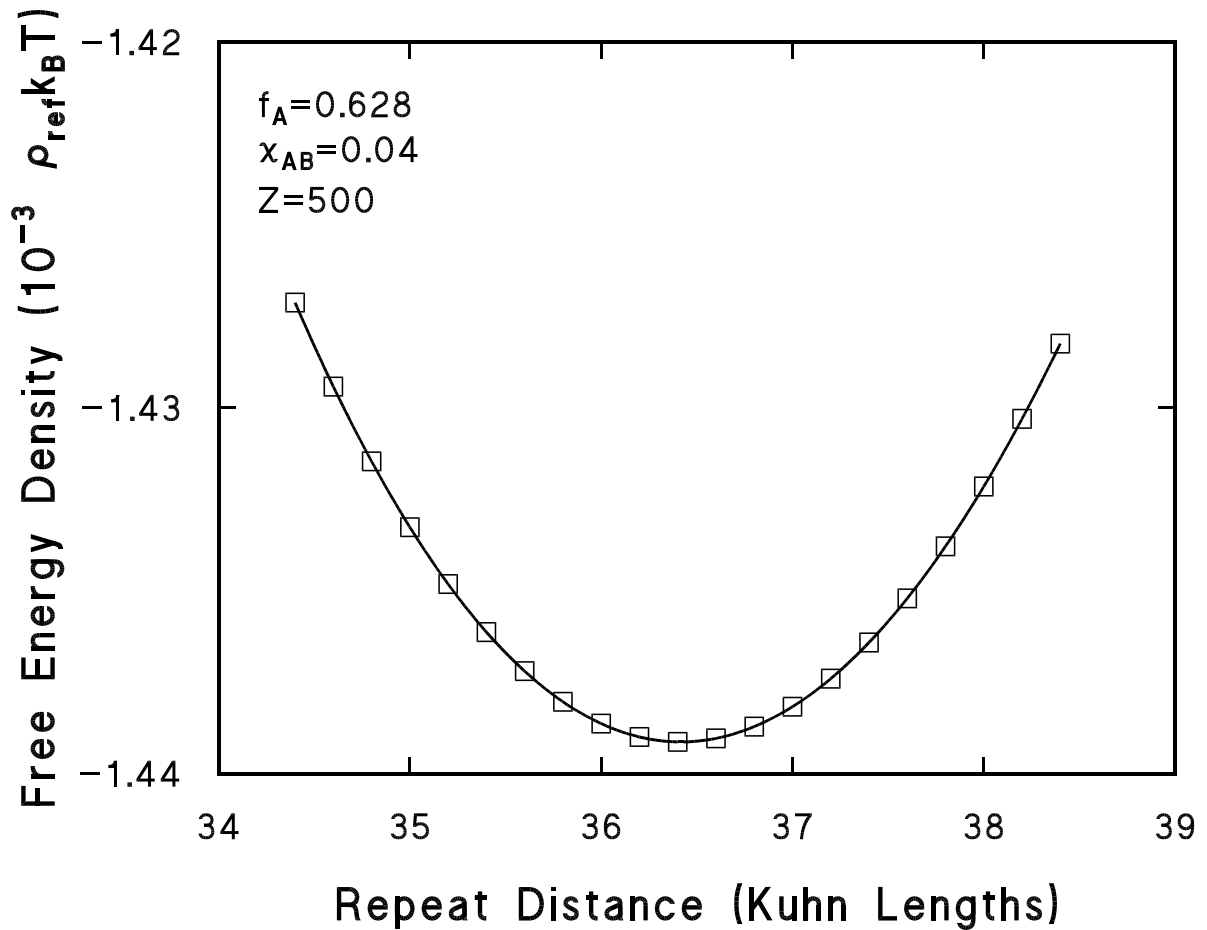


Figure 2.1: Minimisation of the free energy density with respect to lamellar repeat distance, d . The system parameters are $b_A = b_B$, $\rho_{0A} = \rho_{0B} = \rho_{ref}$, $Z_A = 314$, $Z_B = 186$, and $\chi_{AB} = 0.04$, where Z in the diagram has been defined as $Z_A + Z_B$. The step in d for free energy sampling was taken to be 0.2 Kuhn lengths.

Chapter 3

The Phase Diagram and Density Distributions

3.1 Introduction

We wish to predict the dependence of the equilibrium morphology on system parameters. We chose to investigate systems in which $\rho_{0A} = \rho_{0B} = \rho_{ref}$ and $b_A = b_B$ as was done in previous treatments, [2, 20, 28, 29] so that we can compare our results with these. Thus, it is only necessary to calculate the phase diagram for $f_A \geq 0.5$ since values of f_A below 0.5 would correspond to $f_B \geq 0.5$. In such a case, our results could be applied by interchanging A and B . As σ was, in previous treatments, [2, 29] found to have negligible effect, it was chosen to be zero in this investigation. We have verified that the results were negligibly affected for changes of $\sigma = 0$ to $\sigma = b$ for several representative systems, with the density profiles and free energies unchanged to one part in 10^3 .

The equilibrium structure is identified by choosing a combination of Z_A , Z_B , and χ_{AB} and solving the self-consistent problem for the lattice parameter, free energy, and density profiles of each morphology (corresponding to $m = 1, 2$, and 3). The associated free energy densities, Δf , were then compared, the lowest being identified as the one belonging to the equilibrium structure. In the case where all three free energies were positive, it was concluded that no microstructure formed and the homogeneous melt was the equilibrium state, since equation (2.56) is measured relative to the homogeneous state.

Leibler's work, [20] as well as that of Helfand and Wasserman, [16] suggested that

χ_{AB}	Z
0.022 to 0.160	500
0.055 to 0.400	200
0.1	110 to 800

Table 3.1: Parameter ranges for the three investigated phase diagrams.

the phase diagram in such systems would be parameterised by two quantities: f_A and the product $\chi_{AB}Z$. For our investigation, we constructed three phase diagrams. In two of these, Z was fixed and the equilibrium structure was located in terms of χ_{AB} and f_A . For the remaining diagram, χ_{AB} was fixed and Z and f_A were varied. Table 3.1 indicates the chosen parameters.

Determining the equilibrium structure for all possible combinations of these parameters required locating the phase boundaries between morphologies. Using prior approximations as a guide, a single point on a phase boundary was located by fixing the values of *both* Z and χ_{AB} , and incrementing f_A in small steps. For each f_A , the free energy was found through self-consistent calculations for each morphology. A plot of free energy versus f_A for the structures was then constructed (cf. Figure 3.1). By fitting fourth order polynomials to each free energy curve, we located the point at which two free energy curves intersected. This would be a point on the phase boundary for the chosen Z and χ_{AB} . Figure 3.1 illustrates this method in which, for $\chi_{AB} = 0.04$ and $Z = 500$, the structure was found to change from lamellar to cylindrical for $f_A \gtrsim 0.632$. Except near the order-disorder transition, the estimated uncertainty in the free energy was less than one part in 10^4 . In all cases, the difference in energy between morphologies and the change in free energy due to increments in f_A were both at least 100 times larger than this uncertainty.

Plots as shown in Figure 3.1 were constructed for each transition at a fixed χ_{AB} and

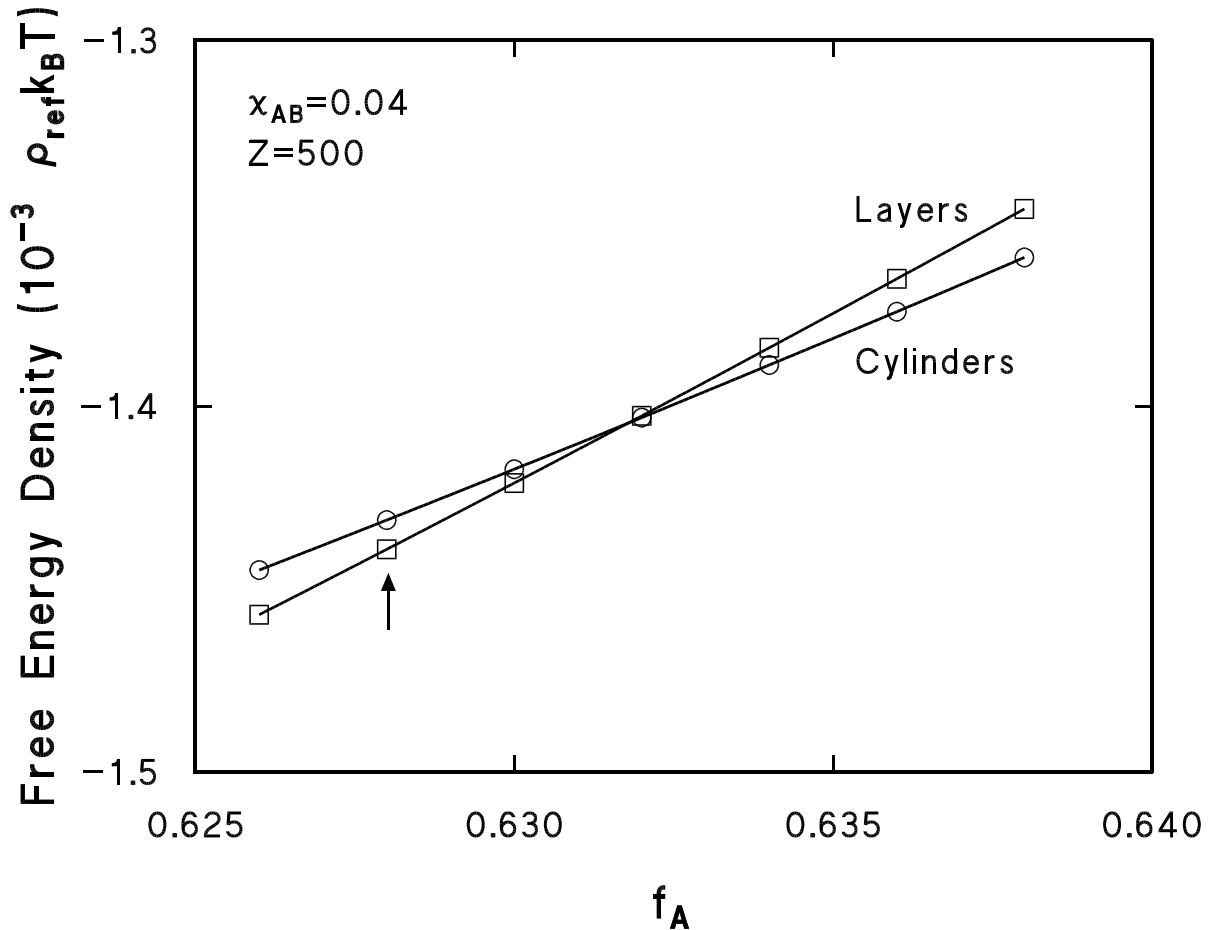


Figure 3.1: Determination of the equilibrium structure for $\chi_{AB} = 0.04$, $Z = 500$. The free energy densities of the layers and cylinders, minimised with respect to d or R respectively, were calculated for seven values of f_A , given in Table A.1 of Appendix A. The data have been fit to a fourth order polynomial to determine the point of intersection. The lowest free energy is associated with layers for $f_A < 0.632$ and cylinders above this point. Spheres had a significantly higher free energy for these parameters and are not shown. The arrow indicates the system identified in Figure 2.1.

Z . This entire process was then repeated for a different χ_{AB} or Z as appropriate to the phase diagram. Figure 3.2 summarises this investigation. The numerical values for each of the three phase diagrams described in Table 3.1 are given in Tables A.2 through A.4 of Appendix A respectively, and the mean value of f_A for the phase boundary as a function of $\chi_{AB}Z$, along with standard deviations, are given in Table A.5.

3.2 Results and Discussion

We found that, if we plotted the phase boundaries as functions of $\chi_{AB}Z$ and f_A , then all corresponding phase boundaries on the three phase diagrams coincided for a particular value of $\chi_{AB}Z$ to within an uncertainty of $\Delta f_A = \pm 0.003$. Thus, Leibler's implication that the phase diagram depends solely on $\chi_{AB}Z$ and f_A near the MST has been verified, in the cases investigated here, to apply to the entire phase diagram to within numerical accuracy. Figure 3.2 is a composite diagram of three cases in Table 3.1, where each phase boundary is determined by the mean value of f_A on the boundary associated with each tested $\chi_{AB}Z$. As a matter of scale, if the three individual phase diagrams were instead plotted on these axes, the deviation between corresponding phase boundaries would be less than the width of each line.

In fact, the uncertainty of $\Delta f_A = \pm 0.003$ occurs on the sphere-homogeneous (S-H) transition boundary at $\chi_{AB}Z = 12$. On a plot of $\chi_{AB}Z$ versus f_A as in Figure 3.2, the phase boundary is nearly horizontal here, and so, this uncertainty should not be considered significant. For $\chi_{AB}Z \geq 13$ where the slopes become steeper, the largest uncertainty reduces to $\Delta f_A = \pm 0.001$.

As can be seen in the figure, all of the boundaries appeared to converge to $f_A = 0.5$ as $\chi_{AB}Z$ approached 10.5. The exact point of convergence was, in fact, determined through a slightly different method than that used for the other points. In this case, f_A was fixed and the free energy for each structure was calculated as a function of χ_{AB} or Z as appropriate to the graph. In all three cases of Table 3.1, two significant features were observed for this symmetric case of $f_A = f_B = 0.5$. First, the free energy for the lamellar structure was always the lowest of the three ordered morphologies, becoming equal to that of the homogeneous structure as $\chi_{AB}Z \rightarrow 10.504 \pm 0.004$. Secondly, the amplitudes of the density profiles were found to decay smoothly to zero as we approached this limit.

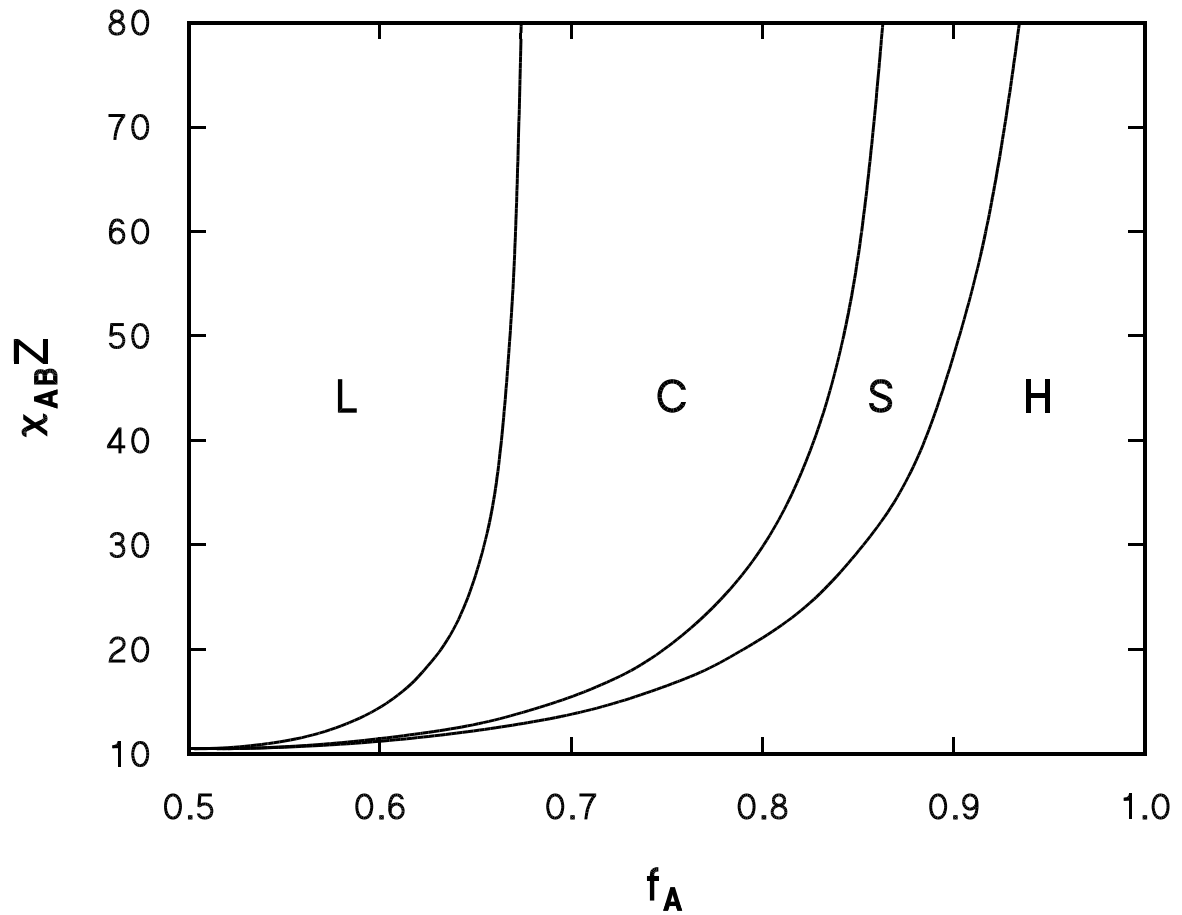


Figure 3.2: Composite phase diagram for the three investigations. The equilibrium morphology — layers (L), cylinders (C), or spheres (S) — is identified as a function of χ_{ABZ} and f_A . The disordered homogeneous phase is designated here by H. In all three cases in Table 3.1, the same phase diagram was obtained to within the numerical uncertainty.

This indicates a direct second-order phase transition from layers (L) to homogeneous (H) at $f_A = 0.5$, $\chi_{AB}Z = 10.504 \pm 0.004$.

In contrast, for any point on the phase diagram such that $f_A \neq 0.5$, there is no direct transition from the homogeneous to lamellar state. The homogeneous state is instead bounded by a transition to the spherical morphology as found in Leibler's investigation. Also, unlike the symmetric case, this phase transition is observed to be first-order as there is a discontinuous change in the amplitude of the density variations crossing this boundary. This discontinuity increases in magnitude as f_A moves further away from 0.5, or equivalently, as $\chi_{AB}Z$ increases.

Figures 3.3 through 3.5 illustrate typical density profiles obtained for various morphologies and system parameters. These represent the equilibrium solutions for the functions $\phi_\kappa(\mathbf{r})$ for the identified equilibrium morphology and correspond to the density variations within a single unit cell for the structures illustrated in Figure 1.1. These profiles have been calculated to a self-consistent uncertainty of less than $\pm 10^{-5}$. Figure 3.3 indicates two typical extremes of the lamellar structure, both at $f_A = 0.5$. In Figure 3.3(a), $\chi_{AB}Z = 11$, which is very close to the order-disorder transition. At this location, the system is weakly segregated with appreciable intermixing. The density profiles are very cosine-like as expected by Leibler, but, even this close to MST, their amplitudes are nearly half of their average values. In contrast, Figure 3.3(b) is also for $f_A = 0.5$, but at $\chi_{AB}Z = 80$. In this strongly segregated limit, the density profiles have a qualitative hyperbolic tangent shape. There are large subdomains occupied exclusively by either species A or B , with intermixing occurring in less than 20% of the unit cell.

Similar results were obtained for the cylindrical morphology. Figure 3.4 illustrates two systems at $f_A = 0.7$ where cylinders are the equilibrium structure. In 3.4(a), $\chi_{AB}Z = 15.5$ which corresponds to a point on the phase diagram virtually on the C-S transition boundary (cf. Figure 3.2). Again, this profile is qualitatively cosine-like in shape, but

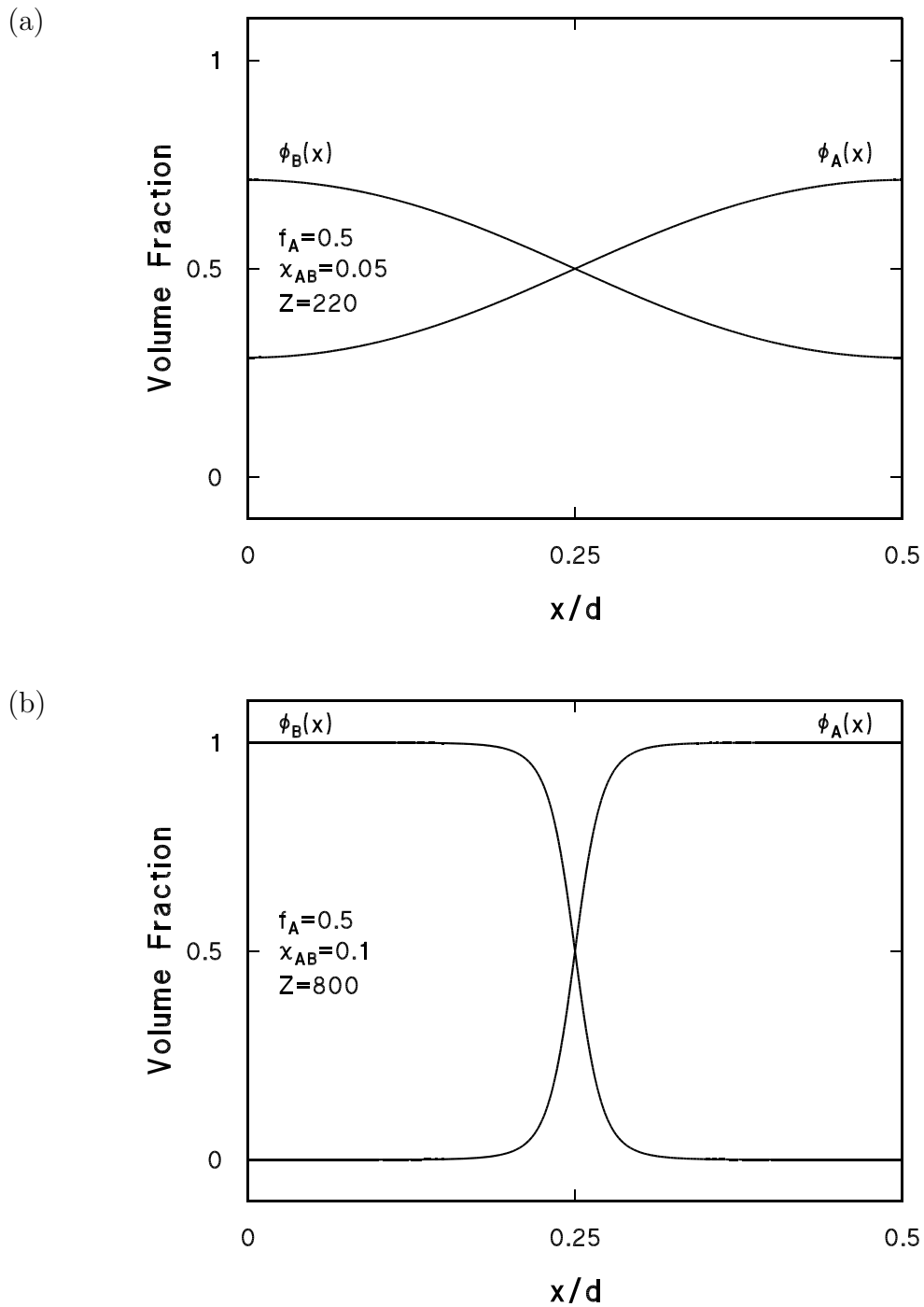


Figure 3.3: Sample density profiles for the lamellar structure. (a) Weak-segregation limit with $\chi_{AB}Z = 11$, $f_A = 0.5$. (b) Strong-segregation limit with $\chi_{AB}Z = 80$, $f_A = 0.5$. The position within the unit cell, x , has been normalised to the repeat distance d . The profile from $x/d = 0.5$ to $x/d = 1$ is the mirror image of this.

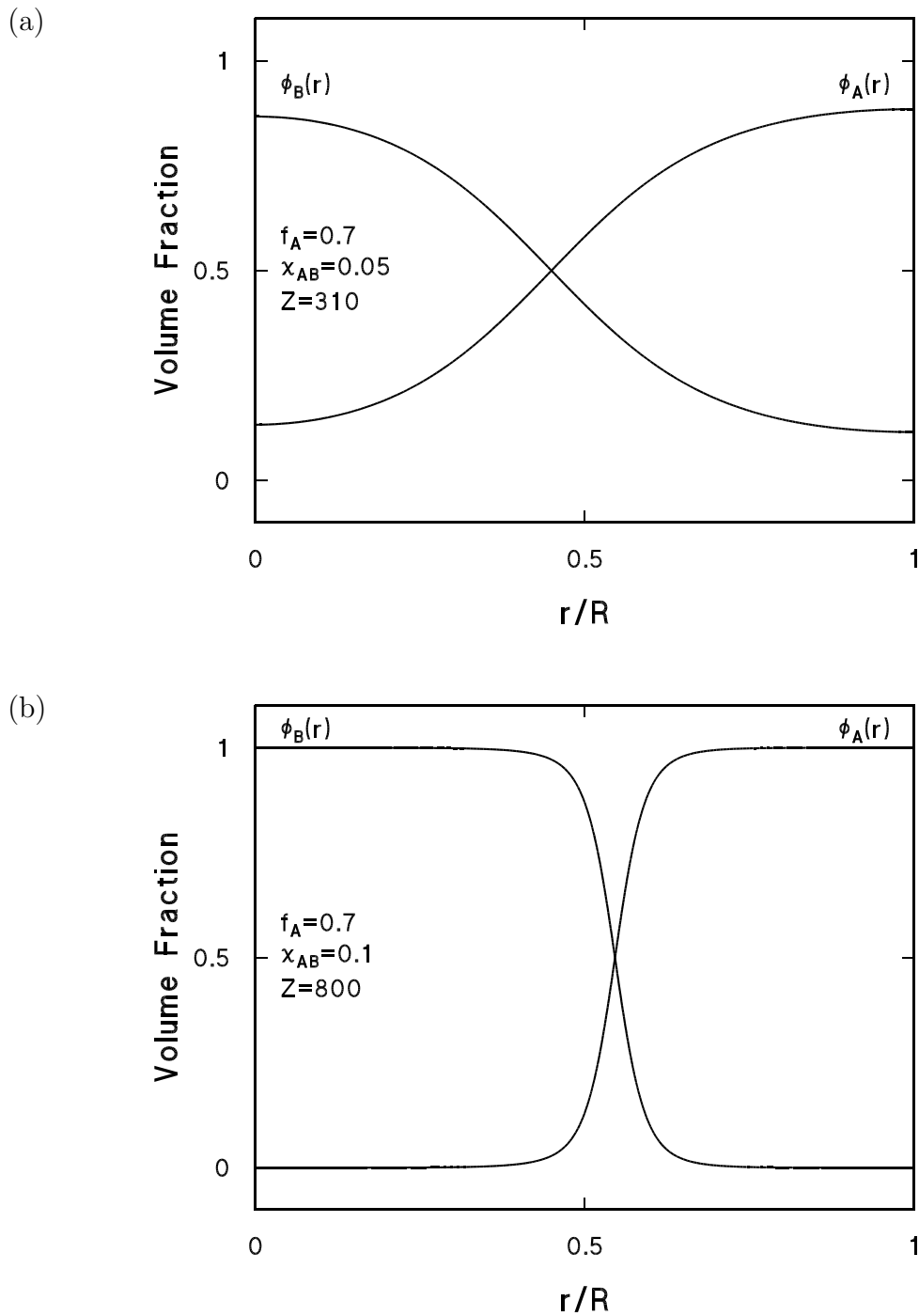


Figure 3.4: Sample density profiles for the cylindrical structure. (a) Weak-segregation limit with $\chi_{AB}Z = 15.5$, $f_A = 0.7$, lying virtually on the C-S boundary of Figure 3.2. (b) Strong-segregation limit with $\chi_{AB}Z = 80$, $f_A = 0.7$. The radial coordinate within the unit cell, r , has been normalised to the cell radius R .

with a slightly higher amplitude than the weakly-segregated lamellar structure. In Figure 3.4(b), we also see the hyperbolic-tangent-like strong segregation for $\chi_{AB}Z = 80$ at the same f_A .

In the case of the spherical morphology, Figure 3.5(a) represents a system lying virtually on the S-H transition boundary, with $f_A = 0.636$ and $\chi_{AB}Z = 12$. Despite this close proximity to the homogeneous phase (the transition is at $f_A = 0.640$ for $\chi_{AB}Z = 12$), there is still an appreciable variation in the local volume fraction — from 0.25 to 0.75. This demonstrates the first-order nature of the phase transition for asymmetrical copolymers. The profiles themselves, however, are still cosine-like. For $\chi_{AB}Z = 80$, $f_A = 0.9$, the density distribution has, again, a more hyperbolic-tangent quality.

This last pair of density profiles, Figure 3.5(b), exhibit a significant qualitative result. It is for a large value of $\chi_{AB}Z$, but it is also near the order-disorder transition which occurs at $f_A = 0.934$ for $\chi_{AB}Z = 80$. As such, it shares qualities of the two extremes — a hyperbolic-tangent shape, and significant intermixing. Despite this close proximity to the S-H boundary, however, the density variations have reached full amplitude, again indicating a first-order transition. This was in fact verified as converged solutions of significant amplitude were obtained for the spherical morphology at $\chi_{AB}Z = 80$ for values of f_A as high as 0.935, where the free energy is in fact positive relative to the homogeneous phase. Effectively, we have found a density profile normally associated with strong segregation for a system which is actually near the MST. Such a result contradicts the assumption of both Leibler, [20] and Fredrickson and Helfand. [11]

These results can be compared with prior investigations in their respective limits. In Leibler's theory, [20] the phase boundaries were found to converge at $\chi_{AB}Z \approx 10.5$ and $f_A = 0.5$ where a second-order L-H transition was located. Also, for $f_A \neq 0.5$ the only order-disorder transition was a first-order S-H phase change. The density profiles in Figures 3.3(a), 3.4(a) and 3.5(a) were also found to be cosine-like. All of this is

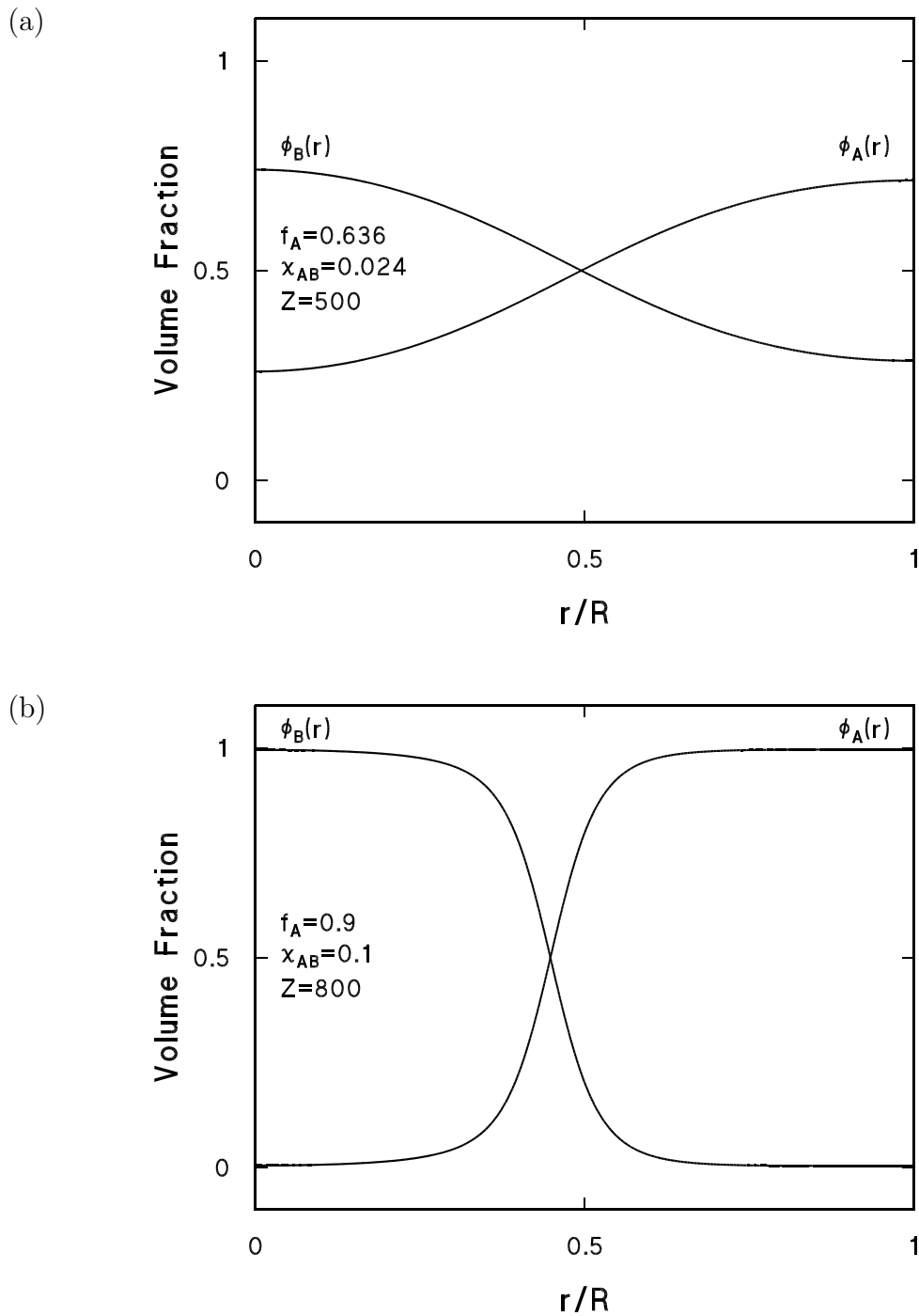


Figure 3.5: Sample density profiles for the spherical structure. (a) Weak-segregation limit with $\chi_{AB}Z = 12$, $f_A = 0.636$, lying virtually on the S-H boundary of Figure 3.2. (b) Strong-segregation limit with $\chi_{AB}Z = 80$, $f_A = 0.9$. The radial coordinate within the unit cell, r , has been normalised to the cell radius R .

consistent with Leibler's approximation. However, we find that for $\chi_{AB}Z \gtrsim 14$, the phase boundaries depart from Leibler's result. His phase diagram had qualitatively parabolic phase boundaries, with a very narrow region for the spherical structure: $f_A \approx 0.87$ to $f_A \approx 0.88$ for $\chi_{AB}Z = 50$. In our diagram, above $\chi_{AB}Z \gtrsim 14$, the slope of the L-C and C-S boundaries rapidly become nearly vertical with a much wider spherical region: $f_A \approx 0.84$ to $f_A \approx 0.90$ for $\chi_{AB}Z = 50$. Also, the S-H order-disorder line has moved out from the Leibler result for $f_A \neq 0.5$ such that ordered structures are stable for more asymmetric values of f_A than predicted by Leibler.

This correlates with the evolution of the density profiles from a cosine-like function to a hyperbolic-tangent-like function as $\chi_{AB}Z$ is increased. The density profile of Figure 3.5(b) indicates that this is not simply a consequence of moving away from the order-disorder line, and so, one may conclude that the Leibler approximation is valid only for a limited range of $\chi_{AB}Z \lesssim 14$.

The other limit, that of the strong segregation regime, includes systems which have a high degree of polymerization (i.e., large Z). This is the domain of Helfand and Wasserman's NIA theory, [16] which predicts that the phase boundaries depend on only the volume fraction, f_A . We can in fact see this trend in our phase diagram, as, even with $\chi_{AB}Z$ at a modest 80, the boundaries are becoming vertical. As it is conceivable that Z could exceed 10^4 , with a typical $\chi_{AB} \approx 0.2$, it is reasonable to conclude that for such a domain, variations in χ_{AB} or Z of an order of magnitude would have little effect on the location of the phase boundaries with respect to f_A . Though in the NIA a system of PS-b-PBD was investigated, the location of the phase boundaries at weight fractions of 0.3 and 0.65 (L-C) and 0.1 and 0.85 (C-S) is in reasonable agreement with the strong segregation limit of Figure 3.2. The NIA also predicted a qualitatively similar variation of the MST boundary with f_A . The asymmetry between $f_A \geq 0.5$ and $f_A \leq 0.5$ in their

result can be attributed to the differences in monomer densities and Kuhn lengths for that system.

Our results are also consistent with our previous investigation of copolymer/neutral solvent blends. [29] A result of that work was that the phase diagrams for systems of equal bulk monomer densities and Kuhn lengths were approximately determined by two quantities, as here. The quantities in that case, however, were $\chi_{eff}Z$ and f_A where, for a solvent occupying fraction $\bar{\phi}_S$ of the total system volume, we define $\chi_{eff} \equiv (1 - \bar{\phi}_S)\chi_{AB}$. This is known as the dilution approximation. If we use $\bar{\phi}_S = 0$ for the current investigation, Figure 3.2 maps onto the phase diagram for copolymer/solvent blends with a discrepancy between boundaries of $|\Delta f_A| \leq 0.01$ for corresponding values of $\chi_{eff}Z$. The dilution approximation is discussed in further detail in Section 3.4.

It is found in experiment that the equilibrium structure is determined by f_A for strongly-segregated systems, with the L-C transition at 0.65 and the C-S transition at 0.8. [14] The order-disorder line is variable, with a homogeneous solution guaranteed for sufficiently small Z or high temperature (i.e., $\chi_{AB}Z \approx 10.5$ for the symmetric case). In addition, the Ordered Bicontinuous Double-Diamond structure is observed in certain PS-b-PI systems for f_A between 0.27 and 0.38. [26] This is in good qualitative agreement with our strong segregation regime for the L, C, and S structures, and with the symmetric L-H transition as well as the predicted MST.

Experimental comparison in the weak segregation regime is sparse, however. Temperature induced changes in morphology have only recently been observed in experiment. [4] In that investigation, for $f_A = 0.65$, the lamellar structure of poly(ethylene-propylene)-poly(ethylene), or PEP-PEE, was observed at the lowest temperature. As the temperature was increased, the equilibrium morphology changed to the OBDD and cylindrical phases before reaching MST. This phenomenon is predicted in our theory by the bending of the phase boundaries towards smaller f_A in the weak segregation of Figure

3.2, making more than one morphology accessible by varying χ_{AB} for a fixed r_C and f_A . The sparsity of data on this phenomenon can be attributed to several factors. Most obvious is the fact that this region exists over a very small domain of $10.5 \lesssim \chi_{AB} Z \lesssim 14$. It is likely that it might be difficult to obtain systems precisely in this narrow range.

Also, there is the consideration of *metastability*. A chemical system would be specified by a particular fixed r_C and f_A with χ_{AB} being varied through its temperature dependence. Thus, descending the phase diagram along a constant f_A contour of, for example, 0.7, one would make a transition from cylinders to spheres and then the homogeneous state. Between $\chi_{AB} Z = 15.5$ and 14, the spherical structure would have the absolute minimum in free energy. However, there will be a local minimum in the free energy functional about the cylindrical structure. This is essentially the definition of metastability. As such, the system would be stable to small thermal fluctuations and may remain in the cylindrical structure even after entering this regime. It is quite conceivable that thermal fluctuations would not be sufficient to overcome this local minimum until the system is appreciably into the domain of homogeneous stability. A full understanding of these thermal fluctuations must, however, go beyond the mean field approximation by its very nature.

In relation to this, Fredrickson and Helfand considered the effect of fluctuations on the free energy functional of Leibler theory. [16] There, it was found that “windows” opened in the lower $\chi_{AB} Z$ regions of the phase diagram where C-H and L-H transitions were possible for $f_A \neq 0.5$. [11] It is likely that this might also occur, perhaps to a lesser extent, in our fully self-consistent theory.

Another experimental property which may serve to hamper a simple theoretical treatment is that of *polydispersity*. It is a practical impossibility to obtain a system comprised entirely of identical copolymers. The parameters Z and f_A will in fact have a distribution centered around the desired and most probable values. For the purposes of argument, one

might think of this distribution as being Gaussian. If this distribution had an effective width such that $\chi_{AB}\Delta Z \gtrsim 3.5$, this might be sufficient to obscure these narrow regions of low asymmetry cylinders and spheres. Since $\chi_{AB}Z \approx 12$ in this region, we have can restate this bound on polydispersity as $\Delta Z/Z \gtrsim 0.3$, which is of experimental magnitude.

As a final note, there have been limited attempts to predict the Ordered Bicontinuous Double-Diamond equilibrium microphase from theory, none of which have been successful. [1] This structure is in fact a recent discovery, having been first reported in 1986. [25, 26] In our approach, it was necessary to solve the diffusion equation for $q_\kappa(r, \tau)$ and $q'_\kappa(r, \tau)$. This was done by discretising space into 100 equal intervals. As the OBDD is a three dimensional structure with no simple dimension-reducing symmetry, even a $50 \times 50 \times 50$ grid would represent a 3750-fold increase in computation time. Such an undertaking is beyond the scope of this project. Ideally, it would be desirable to reduce such a system to a one-dimensional problem. In principle, one could parameterise this system in terms of contour surfaces of constant $\phi_\kappa(\mathbf{r})$ which should be dependent only on the symmetry. The family of surfaces would then have a single independent parameter, however the exact shape of these surfaces and, more important, the forms of the associated Laplacian and normal gradients in this symmetry are unknown.

3.3 Generalisation of the Phase Diagram

The phase boundaries on the microphase diagrams for our three model systems are nearly exactly superimposed when plotted using $\chi_{AB}Z$ and f_A as the axes. This implies some generalisation of the system in terms of these variables, as found in earlier approximations. In this section, we show this to be an intrinsic property of the mean field theory.

We begin by restating our equations in terms of a reduced distance $r/R \rightarrow r$ and a reduced monomer step $\tau/Z_\kappa \rightarrow \tau$. In this scale, the diffusion equation becomes

$$\left[\frac{b_\kappa^2}{6R^2}\nabla^2 - \omega_\kappa(r)\right]q_\kappa(r, \tau) = \frac{1}{Z_\kappa}\frac{\partial}{\partial\tau}q_\kappa(r, \tau), \quad (3.1)$$

where the interval of both r and τ become $[0, 1]$. The same can be done for $q'_\kappa(r, \tau)$ where the initial conditions become

$$q'_A(r, 0) = q_B(r, 1), \quad (3.2)$$

$$q'_B(r, 0) = q_A(r, 1). \quad (3.3)$$

In terms of these new fields, the potentials $\omega_\kappa(r)$ remain as defined in equations (2.52) and (2.53). However, the expressions for the density profiles $\phi_\kappa(r)$ become

$$\phi_\kappa(r) = \frac{\alpha_m(1)}{m}\frac{\bar{\phi}_\kappa}{Q'_C}\int_0^1 d\tau q_\kappa(r, \tau)q'_\kappa(r, 1 - \tau), \quad (3.4)$$

with

$$Q'_C = \int_0^1 \alpha_m(r)dr q_A(r, 1)q_B(r, 1), \quad (3.5)$$

where we recognise that the rescaled distance reduces Ω to $\alpha_m(1)/m$ via equation (2.67).

Multiplying the diffusion equation by $r_C\rho_{0\kappa}/\rho_{ref}$, and using the definition of f_κ in (1.4), we obtain

$$[\epsilon_\kappa\beta\nabla^2 - \omega'_\kappa(r)]q_\kappa(r, \tau) = \frac{1}{f_\kappa}\frac{\partial}{\partial\tau}q_\kappa(r, \tau), \quad (3.6)$$

where

$$\beta \equiv \frac{r_C \rho_{0A} b_A^2}{6 \rho_{ref} R^2}, \quad (3.7)$$

$$\epsilon_\kappa \equiv \frac{\rho_{0\kappa} b_\kappa^2}{\rho_{0A} b_A^2}, \quad (3.8)$$

and

$$\omega'_A(r) = \chi_{AB} r_C [\phi_B(r) - \bar{\phi}_B + \frac{\sigma^2}{6} \nabla^2 \phi_B(r)] + \eta'(r), \quad (3.9)$$

$$\omega'_B(r) = \chi_{AB} r_C [\phi_A(r) - \bar{\phi}_A + \frac{\sigma^2}{6} \nabla^2 \phi_A(r)] + \eta'(r). \quad (3.10)$$

The function $\eta'(r)$ is defined as $\eta(r)/\rho_{ref}$ and is given by

$$\eta'(r) = \frac{\omega'_A(r) + \omega'_B(r)}{2}. \quad (3.11)$$

Equations (3.4) through (3.11) form a rescaled version of our self-consistent system of equations. We recognise that $\epsilon_A = 1$ and $f_B = 1 - f_A$, so only five independent parameters are present: β , f_A , $\epsilon \equiv \epsilon_B$, σ , and the product $\chi_{AB} r_C$. Of these, we have found σ to have negligible effect and have set it to zero.

The fields $\phi_\kappa(r)$ remain unchanged by the transformation. Thus, in the most general sense, each distinct solution to our system of equations, and by extension each distinct physical microstructure, is parameterised solely by these four remaining parameters. Furthermore, we shall shortly see that one of these variables can be eliminated through the requirement that the free energy be minimised with respect to R for an equilibrium structure.

Consider a rescaled free energy density $r_C \Delta f$,

$$\begin{aligned} \frac{r_C \Delta f}{\rho_{ref} k_B T} &= \frac{m}{\alpha_m(1)} \int_0^1 \alpha_m(r) dr \times \\ &\left\{ \chi_{AB} r_C [\phi_A(r) \phi_B(r) - \bar{\phi}_A \bar{\phi}_B - \frac{\sigma^2}{6} \nabla \phi_A(r) \cdot \nabla \phi_B(r)] - \right. \\ &\left. \omega'_A(r) \phi_A(r) - \omega'_B(r) \phi_B(r) \right\} - \ln \frac{m Q'_C}{\alpha_m(1)}. \end{aligned} \quad (3.12)$$

Under the original system of equations, this minimisation requires $\partial\Delta f/\partial R = 0$. In the transformed system of equations, R is implicitly contained within the variable β . Thus, Δf can equivalently be minimised with respect to β . Since R and r_C , or equivalently, β and r_C are independent variables, it follows that

$$\begin{aligned}\frac{\partial}{\partial\beta}r_C\Delta f &= r_C\frac{\partial\Delta f}{\partial\beta} \\ &= 0,\end{aligned}\tag{3.13}$$

at equilibrium. From equation (3.12), $r_C\Delta f$ is dependent on the same four parameters as the self-consistent solutions — explicitly on $\chi_{AB}r_C$, and implicitly on β , ϵ , and f_A through the field solutions $\omega_\kappa(r)$ and $\phi_\kappa(r)$. Thus, equation (3.13) represents a holonomic constraint which serves to reduce the number of independent variables in the system by one. [24] In other words, since the derivative $\partial(r_C\Delta f)/\partial\beta$ is a function of these four parameters, equation (3.13) can in principle be solved for one of these parameters in terms of the other three.

Since $\chi_{AB}r_C$, f_A , and ϵ are known quantities which characterise the system, we solve this constraint for β as $\beta_{eq}(\chi_{AB}r_C, f_A, \epsilon)$. Thus, the equilibrium properties of any given system are controlled entirely by the three remaining independent variables. Consequently, the overall phase behaviour of all diblock copolymers can be constructed as a three dimensional phase diagram with axes $\chi_{AB}r_C$, f_A and ϵ . The bounds on these parameters are given by

$$0 \leq f_A \leq 1,\tag{3.14}$$

$$0 < \epsilon \leq 1.\tag{3.15}$$

In principle, the parameter χ_{AB} can be positive or negative (the latter corresponding to a net attraction between unlike monomers, where no microphase separation would occur). However, it is almost always found to be positive as the net A - B interaction is normally

repulsive. [7] Thus, $\chi_{AB}r_C$ is also generally positive.

Though the upper bound on ϵ may not be immediately obvious, it is clear that our theory, to this point, has made no distinction between the two species. We obtain equivalent results when A and B are reversed. Thus, in a case where ϵ is greater than 1, this must correspond to the solution for $\epsilon' = 1/\epsilon$ where A and B have been interchanged.

The lack of dependence on r_C and χ_{AB} individually should not be surprising, as these parameters vary with ρ_{ref} via their definitions (1.3) and (2.39) respectively. The properties of the system should be independent of our choice of reference density. Thus, no physical dependence on r_C or χ_{AB} alone is possible. The dependence on ρ_{ref} cancels in the product $\chi_{AB}r_C$ and so this is indeed a valid physical parameter.

Our investigation considered a model system of $\rho_{0A} = \rho_{0B} = \rho_{ref}$ and $b_A = b_B$. From equation (3.8), $\epsilon = 1$ in all such cases. Furthermore, for a system of equal bulk densities, we see that $r_C = Z$ from the definition (1.3). Our model phase diagram may thus equally be parameterised by f_A and $\chi_{AB}Z$, or f_A and $\chi_{AB}r_C$. Thus, Figure 3.2 represents a planar cross-section of the generalised 3-D phase diagram. Due to the amount of computational time required for this project alone – approximately 9000 computer-hours – the construction of the full 3-D phase diagram remains a task for the future.

As a final remark, we note that this proof includes the supposition that the microstructure is lamellar, cylindrical, or spherical in order that \mathbf{r} may be replaced by r and Ω by $\alpha_m(R)R/m$. In fact, this generalisation may be extended to any system where the volume of the unit cell is parameterised by any single scalar quantity, X . For example, the Ordered Bicontinuous Double-Diamond structure has a cubic unit cell, [26] and so the volume is given by $\Omega_{OBDD} = X^3$. In this case, distances would again be normalised to X , parameterising the system in terms of the same four quantities. The holonomic constraint is again applied to reduce the independent parameters to $\chi_{AB}r_C$, f_A , and ϵ for the equilibrium case (assuming σ to be negligible).

Thus, we may conclude that this parameterisation is independent of the approximation of the Wigner-Seitz unit cells as cylinders or spheres. The observed hexagonal and body-centred cubic lattices have a single independent lattice parameter, and so this generalisation will still be applicable. It is noteworthy, however, that Fredrickson and Helfand's fluctuation theory [11] includes an independent contribution from the parameter Z , and so our generalisation is restricted to the mean field theory.

3.4 The Dilution Approximation

In Section 3.2 we made reference to the *dilution approximation*, in which the phase diagram for copolymer/solvent blends was found to be equivalent to our present neat copolymer system with the substitution of $\chi_{eff} \equiv (1 - \bar{\phi}_S)\chi_{AB}$ for χ_{AB} . [29] In this section, we show that this would follow exactly if the solvent were uniformly and homogeneously distributed throughout the blend. This is an assumption that has particular relevance to experiment.

A rigorous analysis of the connection between these two properties would be especially lengthy, but it is fairly straightforward to make the connection between these two statements through some basic arguments. If we look at the partition function for a copolymer/solvent blend: [2, 27]

$$\begin{aligned} \mathbf{Z} = & \frac{\mathcal{Z}_C^{\tilde{N}_C}}{\tilde{N}_C!} \frac{\mathcal{Z}_S^{\tilde{N}_S}}{\tilde{N}_S!} \int \prod_{i=1}^{\tilde{N}_C} \delta \mathbf{r}_{Ai}(\cdot) \delta \mathbf{r}_{Bi}(\cdot) \prod_{j=1}^{\tilde{N}_S} d^3 r_{Sj} \times \\ & P_A[\mathbf{r}_{Ai}(\cdot)] P_B[\mathbf{r}_{Bi}(\cdot)] \times \\ & \delta[\mathbf{r}_{Ai}(Z_A) - \mathbf{r}_{Bi}(Z_B)] \times \\ & \prod_{\mathbf{r}} \delta \left[1 - \frac{\hat{\rho}_A(\mathbf{r})}{\rho_{0A}} - \frac{\hat{\rho}_B(\mathbf{r})}{\rho_{0B}} - \frac{\hat{\rho}_S(\mathbf{r})}{\rho_{0S}} \right] \times \\ & \exp[-\beta \hat{V}(\cdot)], \end{aligned} \quad (3.16)$$

we see additional terms for the solvent kinetic energy, \mathcal{Z}_S , and the solvent distribution, $\hat{\rho}_S(\mathbf{r})$. Here, \tilde{N}_S is the number of solvent molecules and \mathbf{r}_{Sj} is the position of the j -th solvent molecule. As with the copolymer components, $\hat{\rho}_S(\mathbf{r})$ will be a function of \mathbf{r}_{Sj} .

Let us assume that only the sets of \mathbf{r}_{Sj} which correspond to a uniform distribution of solvent make a significant contribution to the partition function. In that case, we can replace $\hat{\rho}_S(\mathbf{r})$ in equation (3.16) by $\bar{\phi}_S \rho_{0S}$ where $\bar{\phi}_S$ is the total solvent volume fraction.

Within this approximation, the partition function reduces to

$$\begin{aligned}
\mathbf{Z} = & \frac{\mathcal{Z}_C^{\tilde{N}_C} \mathcal{Z}_S^{\tilde{N}_S}}{\tilde{N}_C! \tilde{N}_S!} \int \prod_{i=1}^{\tilde{N}_C} \delta \mathbf{r}_{A_i}(\cdot) \delta \mathbf{r}_{B_i}(\cdot) \times \\
& P_A[\mathbf{r}_{A_i}(\cdot)] P_B[\mathbf{r}_{B_i}(\cdot)] \times \\
& \delta[\mathbf{r}_{A_i}(Z_A) - \mathbf{r}_{B_i}(Z_B)] \times \\
& \prod_{\mathbf{r}} \delta \left[1 - \frac{\hat{\rho}_A(\mathbf{r})}{\rho_{0A}} - \frac{\hat{\rho}_B(\mathbf{r})}{\rho_{0B}} - \bar{\phi}_S \right] \times \\
& \exp[-\beta \hat{V}(\cdot)]. \tag{3.17}
\end{aligned}$$

Assuming a neutral solvent-copolymer interaction, this is equivalent to the partition function (2.4) for the neat copolymer problem. Only the incompressibility term has been changed and an additional multiplicative constant included. The solvent contributions to the potential energy $\hat{V}(\cdot)$ can be included in the homogeneous term of the free energy, f_{hom} . Thus, for a neutral solvent, except for the incompressibility relation, the equations will be the same as for the pure copolymer system derived in Section 2.2. Furthermore, we can apply the methods of Section 3.3 to reduce the number of controlling parameters.

There is a distinction here, however. Before, we had $f_\kappa = \bar{\phi}_\kappa$, but f_κ is the fraction of the *molecule's* volume of type κ while $\bar{\phi}_\kappa$ is the fraction of the *system's* volume of type κ . Since some of the system's volume is occupied by the solvent, these quantities will no longer be the equivalent. For convenience, we define the total copolymer volume fraction, $\bar{\phi}_C \equiv 1 - \bar{\phi}_S$ which is guaranteed by our new incompressibility condition $\phi_A(\mathbf{r}) + \phi_B(\mathbf{r}) + \bar{\phi}_S = 1$. Then, for a solvent occupying a volume fraction $\bar{\phi}_S$ of the system volume, the relation between f_κ and $\bar{\phi}_\kappa$ will become $\bar{\phi}_\kappa = \bar{\phi}_C f_\kappa$.

In Section 3.3, both f_κ and $\bar{\phi}_\kappa$ were present in the final solution. Thus, in this form, $\bar{\phi}_C$ would be an additional parameter. However, we can eliminate this problem by defining a new function,

$$\Phi_\kappa(r) = \frac{\alpha_m(1)}{m} \frac{f_\kappa}{Q'_C} \int_0^1 d\tau q_\kappa(r, \tau) q'_\kappa(r, 1 - \tau). \tag{3.18}$$

This is a rescaling of equation (3.4). In terms of this function, $\phi_\kappa(\mathbf{r}) = \bar{\phi}_C \Phi_\kappa(\mathbf{r})$ and the original incompressibility condition,

$$\Phi_A(r) + \Phi_B(r) = 1, \quad (3.19)$$

is recovered. The potentials (3.9) and (3.10) become

$$\omega'_A(r) = \bar{\phi}_C \chi_{AB} r_C [\Phi_B(r) - f_B + \frac{\sigma^2}{6} \nabla^2 \Phi_B(r)] + \eta'(r), \quad (3.20)$$

$$\omega'_B(r) = \bar{\phi}_C \chi_{AB} r_C [\Phi_A(r) - f_A + \frac{\sigma^2}{6} \nabla^2 \Phi_A(r)] + \eta'(r). \quad (3.21)$$

Similarly, we can define a new rescaled free energy as $r_C \Delta f / \bar{\phi}_C$ to obtain

$$\begin{aligned} \frac{r_C}{\bar{\phi}_C} \frac{\Delta f}{\rho_{ref} k_B T} &= \frac{m}{\alpha_m(1)} \int_0^1 \alpha_m(r) dr \times \\ &\quad \left\{ \bar{\phi}_C \chi_{AB} r_C [\Phi_A(r) \Phi_B(r) - f_A f_B - \frac{\sigma^2}{6} \nabla \Phi_A(r) \cdot \nabla \Phi_B(r)] - \right. \\ &\quad \left. \omega'_A(r) \Phi_A(r) - \omega'_B(r) \Phi_B(r) \right\} - \ln \frac{m Q'_C}{\alpha_m(1)}. \end{aligned} \quad (3.22)$$

Note that in the case of copolymer/solvent blends, there was an additional $\bar{\phi}_C$ factor on the final $\ln Q_C / \Omega$ term of Δf . [28] As before, we can minimise this function with respect to β to obtain our holonomic constraint that eliminates β as an independent variable.

This new system of equations is now *exactly the same as for the neat copolymer system* with $\Phi_\kappa(r)$ being substituted for $\phi_\kappa(r)$ and $\bar{\phi}_C \chi_{AB} r_C$ being substituted for $\chi_{AB} r_C$. In analogy then, a copolymer/neutral solvent blend in the dilution approximation is entirely parameterised by f_A , ϵ , and $\bar{\phi}_C \chi_{AB} r_C$. In terms of our definition of χ_{eff} , this last parameter becomes $\chi_{eff} r_C$. Thus, to the extent that the dilution approximation is correct, the phase diagrams correspond exactly with the substitution of χ_{eff} into the neat copolymer solutions. The density profiles $\phi_\kappa(r)$, potentials $\omega_\kappa(r)$, and the free energy Δf are all simply rescaled from the corresponding neat copolymer solution by a multiplicative factor of $\bar{\phi}_C$.

In the previous work on copolymer/neutral solvent blends, the dilution approximation was *not* assumed, and a small shift in the phase boundaries was observed between diagrams of different $\bar{\phi}_C$. [29] Through the arguments in this section, one concludes that this shifting, being an order of magnitude higher than the uncertainty in f_A , was entirely due to inhomogeneities in the solvent distribution. As the dilution approximation is often used in experiment, this comparison provides a theoretical basis for its validity.

Chapter 4

Equilibrium Domain Sizes

4.1 Introduction

To this point, we have discussed which microstructures can arise in copolymer systems, but little has been said of the details of the structures themselves. We now address one of the more significant quantities associated with the unit cell, namely the lattice parameter, and its dependence on system parameters. As stated earlier, for the lamellar structure, the lattice parameter R is the repeat distance d , and for the cylindrical and spherical structures, it is the radius of the unit cell.

It has been observed in experiment that the lattice parameter R follows a rough power law relation of the form [15]

$$R \propto r_C^q T^r, \quad (4.1)$$

where T is the temperature of the system and q and r are slowly varying exponents. Our model does not include the temperature explicitly, though its effect is included in the parameter χ_{AB} through the relation (1.1). Thus, we expect a rough relation of the form

$$R \propto \chi_{AB}^p r_C^q, \quad (4.2)$$

where, to first approximation, $q \approx -r$. The validity of this approximation is related to the details of the χ_{AB} temperature dependence. Though the C and S structures have been approximated by the Wigner-Seitz cell, the true *hex* and *bcc* lattice parameters should be equal to the radius R multiplied by some geometric factor. Thus, the lattice parameter should obey the same power law relation as R .

To investigate equation (4.2), we chose a representative value of f_A for each structure. Referring to the phase diagram (Figure 3.2), layers clearly form for $f_A = 0.5$, while $f_A = 0.7$ and $f_A = 0.9$ fall roughly in the middle of the C and S regions respectively. These values were thus chosen as typical of their respective structures. Again, we use the model system $\rho_{ref} = \rho_{0A} = \rho_{0B}$ and $b_A = b_B$ giving us $r_c = Z$. Then, choosing a variety of values for χ_{AB} and Z for each structure, we solved the self-consistent equations and determined the lattice parameter which minimised the free energy.

Figures 4.1 through 4.5 summarise this investigation, with the numerical results tabulated in Tables A.6 through A.8 of Appendix A.

4.2 Results and Discussion

The converged solutions had an uncertainty in the equilibrium free energy comparable with that discussed for the phase diagram in Section 3.1. For the layers and cylinders, this allowed us to locate the equilibrium repeat distance, d , or cell radius, R , to an accuracy of ± 0.1 Kuhn lengths. In the case of the spherical morphology at $f_A = 0.9$, the dependence of free energy on cell radius was considerably weaker, and so the maximum uncertainty in the equilibrium cell radius increased to ± 0.5 Kuhn lengths.

In order to determine whether equation (4.2) was a good approximation of the behaviour of the lattice parameter, we plotted the lattice parameter as a function of χ_{AB} and separately as a function of Z for each morphology. These graphs are presented here as Figures 4.1 through 4.3. In each, a log-log scale has been used and so, if (4.2) were exact, then we should obtain straight lines in this representation. In fact, what we found were nearly straight lines, indicating that the proposed scaling relation is indeed a good approximation. The slopes of these lines, which are the exponents p and q , were found to vary slowly, consistent with our hypothesis.

Turning our attention to the lamellar structure at $f_A = 0.5$, the scaling of the repeat distance is given in Figure 4.1. In 4.1(a), we see that for large values of Z , the repeat distance goes roughly as $\chi_{AB}^{0.2}$. In this regime the log-log plot produces a virtually straight line. As we descend through smaller values of Z , we approach the homogeneous phase. As this happens, the slope of the log-log dependence increases. The line for $Z = 200$ is terminated at a higher value of χ_{AB} than those above it as $\chi_{AB} = 0.0525$ corresponds to $\chi_{AB}Z = 10.5$ for that line. Accurate determination of the equilibrium repeat distance approaching this limit is difficult, and so the last point on the solid line corresponds to $\chi_{AB}Z = 11$. Here, the repeat distance goes roughly as $\chi_{AB}^{0.4}$.

The self-consistent calculations could not determine the equilibrium repeat distance

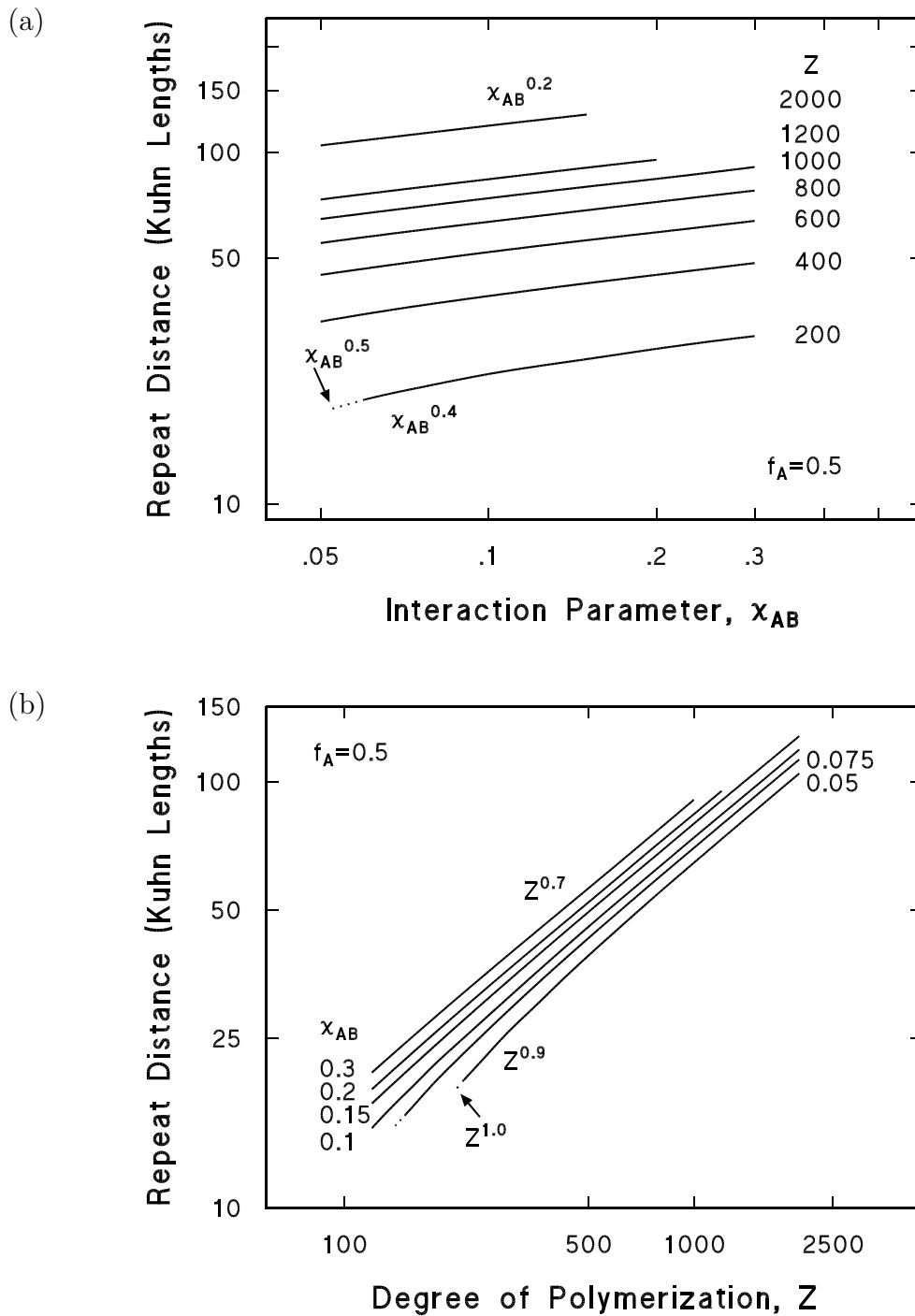


Figure 4.1: Dependence of the repeat distance d on χ_{AB} and Z for layers at $f_A = 0.5$. (a) The repeat distance is given as a function of χ_{AB} for a selection of fixed Z . (b) d as a function of Z for a selection of fixed χ_{AB} . A log-log scale has been used. The calculated points are given in Table A.6. The dotted lines represent an extrapolation to the MST using Leibler theory, [20] as discussed in relation to equation (4.3).

in the limit of $\chi_{AB}Z \rightarrow 10.5$ as the amplitudes of the density profiles diminish below the numerical accuracy. However, for this case of $f_A = 0.5$, the density variations approach those assumed by Leibler as both theories must agree at the MST. Using his results for this limit, [20] the repeat distance is given by $d/b = 2\pi q^*$ where $b = b_A = b_B$ and q^* is the magnitude of the wavevector which minimises the second-order term in the free energy. Numerically, this is found to give

$$\frac{d}{b} = 2\pi\left(\frac{Z}{22.7}\right)^{1/2}. \quad (4.3)$$

Returning to Figure 4.1, we extended the $Z = 200$ line to this limit and found that the scaling for χ_{AB} becomes $\chi_{AB}^{1/2}$ in the limit of the MST. Thus, q varies continuously from 0.7 in strongly segregated systems to 1/2 approaching MST for the symmetric lamellar case.

We found a similar behaviour for the repeat distance as a function of Z in the lamellar structure. In Figure 4.1(b), there is a near linear relation between the logarithms of d and Z . For strongly segregated systems where χ_{AB} is large, the repeat distance goes as $Z^{0.7}$. Again extrapolating to the MST using equation (4.3), we find that this dependence strengthens and the repeat distance goes as $Z^{1.0}$ in this limit.

Figure 4.2 illustrates the corresponding power law relation for cylinders at $f_A = 0.7$. Again, in the strong segregation regime, we find that the lattice parameter, this time the cell radius R , scales as $\chi_{AB}^{0.2}Z^{0.7}$. Descending along $f_A = 0.7$ on the phase diagram, we observe in Figure 3.2 that there is a transition from the cylindrical to spherical morphology before reaching the MST. Approaching this limit, we find that the scaling becomes $\chi_{AB}^{0.4}Z^{0.9}$. This is the lower extent of the solid lines on these graphs. Below the C-S transition on the phase diagram, there is a small region where the free energies satisfy the inequality $\Delta f_S < \Delta f_C < 0$. This occurs between $\chi_{AB}Z = 15.5$ and $\chi_{AB}Z = 14$. In this range, the cylinders are metastable and their radii are indicated

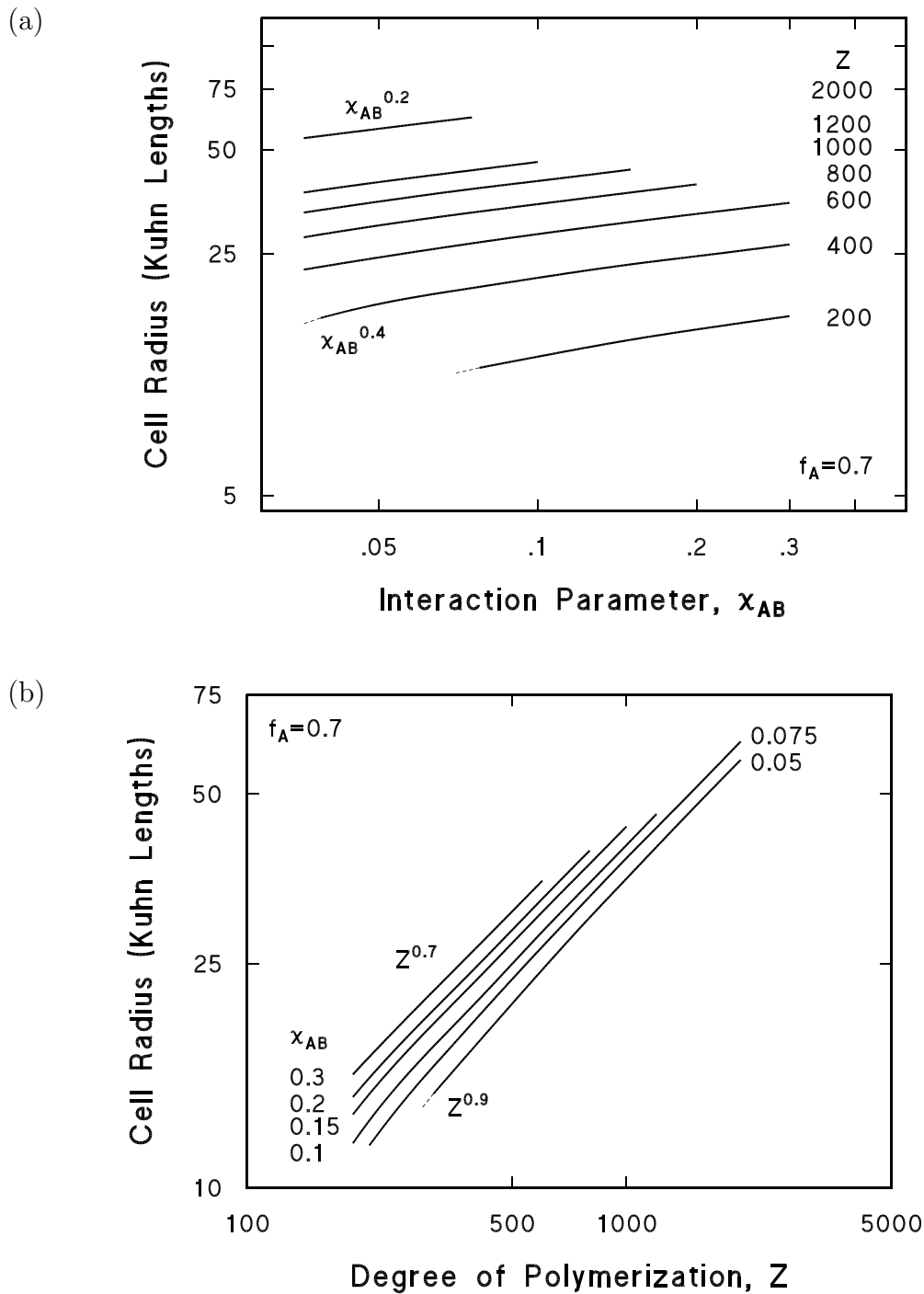


Figure 4.2: Dependence of the cell radius R on χ_{AB} and Z for cylinders at $f_A = 0.7$. (a) The cell radius is given as a function of χ_{AB} for a selection of fixed Z . (b) R as a function of Z for a selection of fixed χ_{AB} . A log-log scale has been used. The calculated points are given in Table A.7. The dashed lines represent solutions for which spheres are the equilibrium structure and cylinders are metastable, with higher free energy.

in Figure 4.2 by dashed lines. For this metastable structure, the scaling increases to roughly $\chi_{AB}^{0.45} Z^{0.95}$ before reaching MST. We could not use the Leibler relation (4.3) to extrapolate to MST in this case since the transition became first order and that approach could no longer strictly be applied. However, this same fact allowed us to perform the self-consistent calculations down to the MST. We thus conclude that these exponents do not reach the respective 1/2 and 1 limits of MST for the lamellar structure.

The case of spheres at $f_A = 0.9$ is illustrated in Figure 4.3. Over this entire range, we found that the cell radius scaled in accordance with the strong segregation limit of the previous cases, namely $\chi_{AB}^{0.2} Z^{0.7}$. Though we must note that the increased uncertainty in cell radius limits our accuracy, there was no detectable variation in exponents from near MST at $\chi_{AB} Z = 52$ up to $\chi_{AB} Z = 180$. The high asymmetry of these copolymers made it difficult to obtain fully converged solutions. This, combined with the increased uncertainty, made it impossible to determine the lattice parameter as we approached MST at $\chi_{AB} Z \approx 49$. However, the calculations were sufficiently accurate that we expect little variation in these exponents in this regime.

Recalling the density profiles presented in Section 3.2, we see that the values of the exponents p and q appear to be related to the amplitude of these profiles. In the limit of full-amplitude, hyperbolic-tangent-like profiles, the exponents are 0.2 and 0.7 for χ_{AB} and Z respectively. As these amplitudes approached zero, the exponents change to $p = 1/2$ and $q = 1$. Since it is only possible to reach zero amplitude for an ordered structure in the case of the second-order L-H transition at $f_A = 0.5$, we find the exponents $p = 1/2$ and $q = 1$ occurred only in this limit. The amplitudes at the MST increase as f_A moves away from 0.5. Correspondingly, the upper bounds on p and q decrease for increasingly asymmetric copolymer. For $f_A = 0.9$ we found that both the amplitudes and these exponents vary little between MST and the strong segregation limit.

An interesting relation can be noted for these exponents. In all cases, the exponents

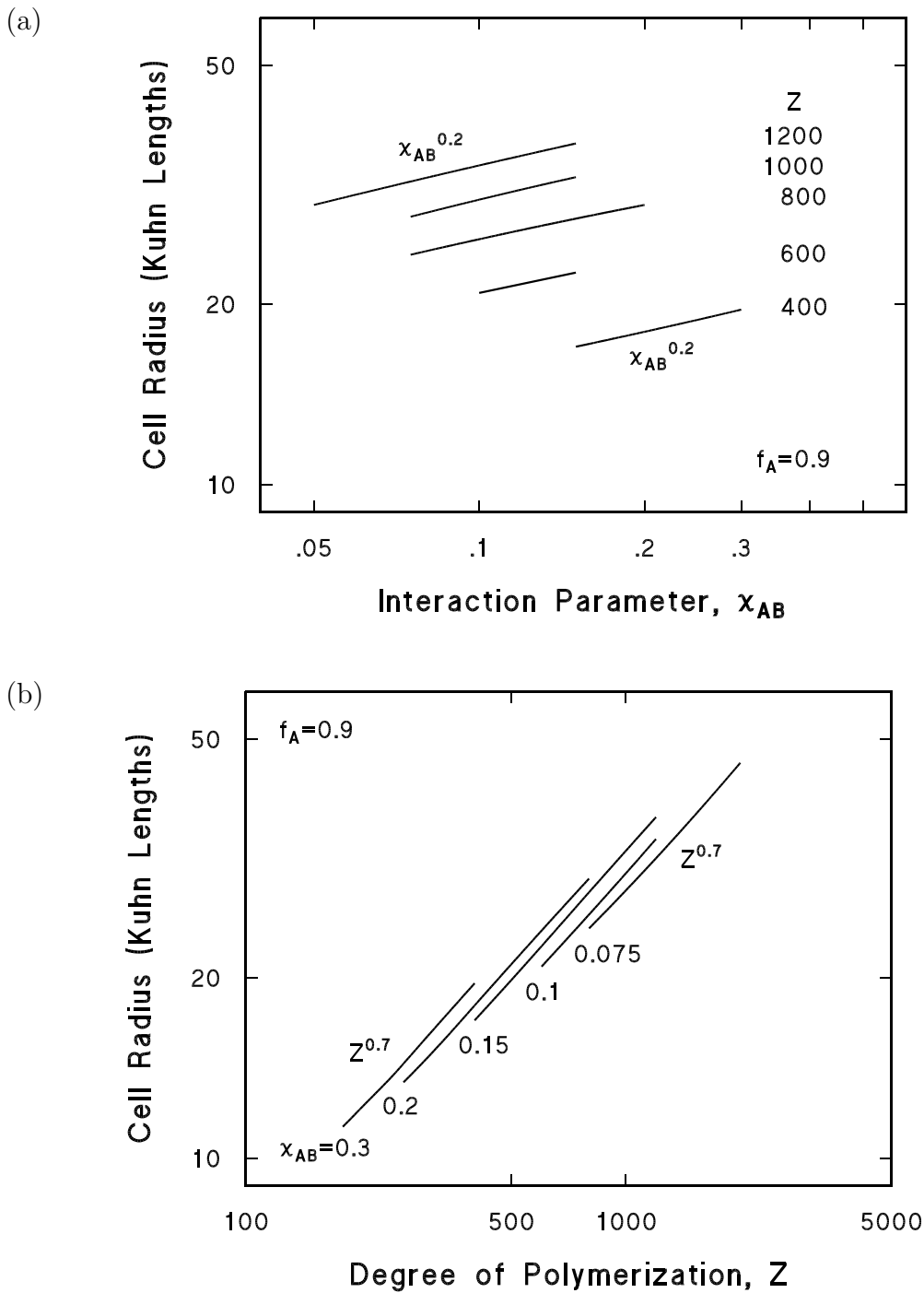


Figure 4.3: Dependence of the cell radius R on χ_{AB} and Z for spheres at $f_A = 0.9$. (a) The cell radius is given as a function of χ_{AB} for a selection of fixed Z . (b) R as a function of Z for a selection of fixed χ_{AB} . A log-log scale has been used. The calculated points are given in Table A.8.

p and q of equation (4.2) were related via

$$q = p + \frac{1}{2}. \quad (4.4)$$

It is very straightforward to demonstrate this as an intrinsic property of the mean field theory. To the extent that the power law relation (4.2) is correct, we can substitute this relation into the expression for β , equation (3.7), to obtain

$$\begin{aligned} \beta &\propto \frac{r_C \rho_{0A} b_A^2}{6 \rho_{ref} \chi_{AB}^{2p} r_C^{2q}} \\ &\propto \frac{\rho_{0A} b_A^2}{6 \rho_{ref}} (\chi_{AB} r_C)^{-2p} r_C^{2p-2q+1}. \end{aligned} \quad (4.5)$$

The arguments of Section 3.3 showed that, at equilibrium, $\beta = \beta_{eq}$ can depend on only $\chi_{AB} r_C$, f_A , and ϵ . It must not vary independently with r_C . Thus, the exponent $2p-2q+1$ must be zero. This, in turn implies that equation (4.4) is satisfied.

We find, in fact, that the power law relations of prior theories are also consistent with our results. Helfand and Wasserman's NIA theory predicted $p = 1/7$ and $q = 9/14$. [16] For $\chi_{AB} Z \rightarrow 180$, we have $p = 0.2$ and $q = 0.7$. It is reasonable to assume that as $\chi_{AB} Z$ goes to infinity, where the NIA approach would be exact, the self-consistent approach would yield results consistent with the NIA.

We can also demonstrate our results to be consistent with that of Leibler's MST limit, equation (4.3). Taking advantage of equation (4.4), we restate the scaling relation (4.2) as

$$R \propto (\chi_{AB} r_C)^p r_C^{1/2}. \quad (4.6)$$

The MST is specified for a particular value of f_A by a fixed value of $\chi_{AB} r_C$. Thus, at the MST limit, the constant $(\chi_{AB} r_C)^p$ is absorbed into the proportionality giving $R \propto r_C^{1/2}$. For our system, we have $r_C = Z$, giving the MST relation predicted by Leibler. However,

it must be noted that, for $f_A \neq 0.5$, the precise value of $\chi_{AB}r_C$ at the MST disagrees with Leibler's result, and so the constant of proportionality for $f_A \neq 0.5$ may also disagree.

Banaszak and Whitmore's analysis of symmetric copolymer/selective solvent blends in the lamellar structure also gave entirely equivalent results to the neat copolymer system, with $p = 0.2$ and $q = 0.7$ in the strong segregation and $p = 1/2$ and $q = 1$ in the weak segregation limit. [3] We can, in fact, generalise our results to the case of copolymer/solvent blends. Considering the dilution approximation, the scaling relation would contain $\chi_{eff} \equiv \bar{\phi}_C \chi_{AB}$ instead of χ_{AB} and so the lattice parameter should scale identically with $\bar{\phi}_C$ and χ_{AB} . This was in fact found for Banaszak and Whitmore's selective solvent study. Also, Whitmore and Noolandi's copolymer/neutral solvent study of the symmetric lamellar structure gave exponents of ~ 0.2 and ~ 0.22 for χ_{AB} and $\bar{\phi}_C$ respectively in the strong segregation and $1/3$ and 0.4 in the weak segregation. [28] The slight disagreement between these values may be attributed to the fact that the weak and strong segregation limits for each exponent did not correspond to the same value of $\chi_{eff}Z$. An additional effect from small inhomogeneities in the solvent density distribution may also be responsible for this discrepancy.

Taking advantage of the generality of equation (4.6), we replot in Figure 4.4 the lattice parameters of the three structures for $\chi_{AB}Z \leq 180$. Here, the three morphologies are plotted on a single graph of $RZ^{-1/2}$ versus $\chi_{AB}Z$ where the scaling for a fixed structure and f_A all fall on a single curve. The variation of the exponent q from weak to strong segregation is readily evident.

In experiment, it was found that, for PS-b-PI and various solvents, the lattice parameters scale roughly as [15]

$$R \propto (\bar{\phi}_C/T)^{1/3} Z^{2/3}. \quad (4.7)$$

This is in rough agreement with our strong segregation limit on Z . As already mentioned,

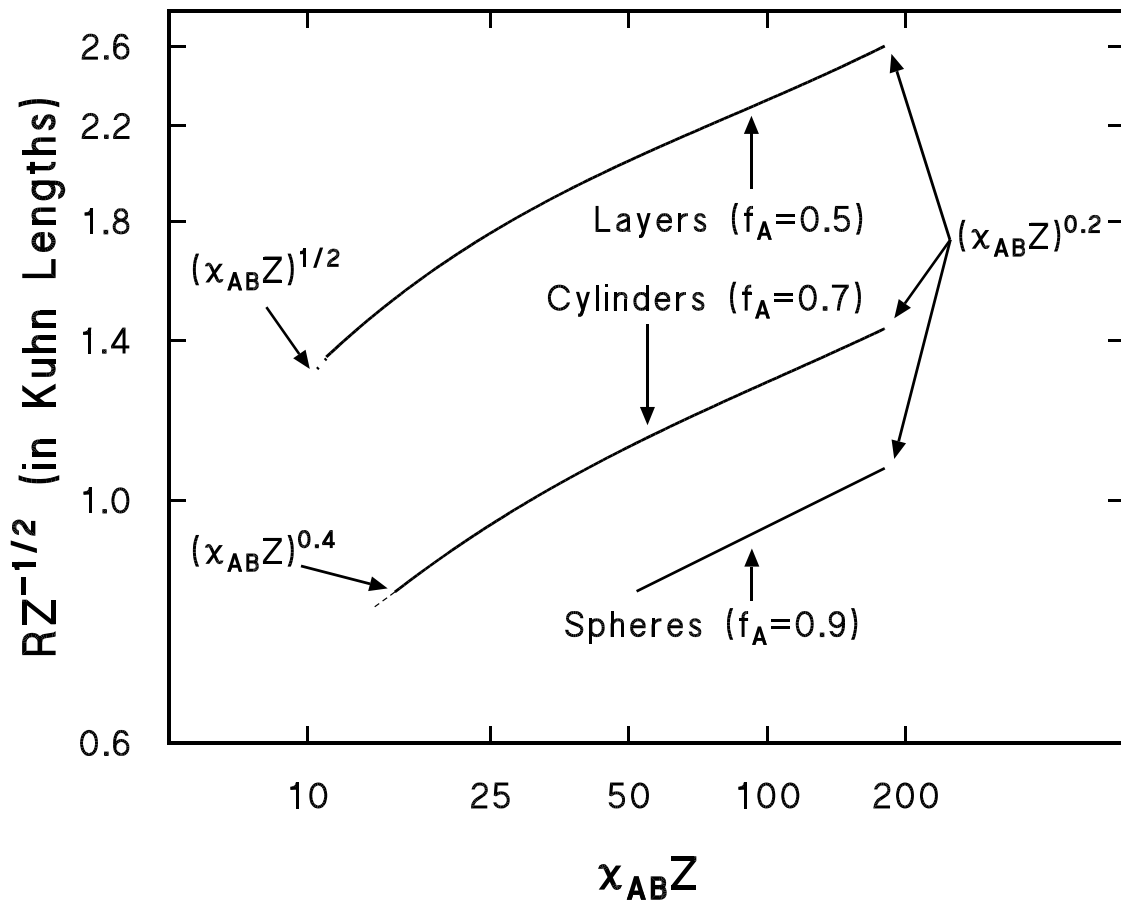


Figure 4.4: Generalised power law relation for layers, cylinders and spheres. The rescaled lattice parameter $RZ^{-1/2}$ is given as a function of $\chi_{AB}Z$. The dotted and dashed lines are as described in Figures 4.1 and 4.2.

however, proper comparison of the T and χ_{AB} exponents would require a thorough study of the dependence of χ_{AB} on temperature.

In the course of this investigation, the equilibrium free energy density associated with each lattice parameter was obtained. Figure 4.5 illustrates this for the selected morphologies and values of f_A used in this chapter. In accordance with equation (3.12), we expect that $Z\Delta f$ should be dependent on only $\chi_{AB}Z$ for a fixed f_A and ϵ , as here. To the degree that the curves in this figure are straight, we find that, as for the copolymer/neutral solvent case, [28] the free energy density obeys the relation

$$\frac{\Delta f}{\rho_{ref}k_B T} \propto -\frac{1}{\chi_{AB}Z^2}(\chi_{AB}Z - \alpha)^2, \quad (4.8)$$

where α depends on the structure and f_A . This relation is illustrated in the figure. The slight curvature can be attributed to higher order terms of the form $(\chi_{AB}Z - \alpha)^n/\chi_{AB}Z^2$. The exact value of α is given by the MST value of $\chi_{AB}Z$ for the L-H transition at $f_A = 0.5$ and the S-H transition at $f_A = 0.9$ for layers and cylinders respectively. Since there is no direct C-H transition at $f_A = 0.7$, α is simply the value at which the metastable cylinders' free energy goes to zero in that case.

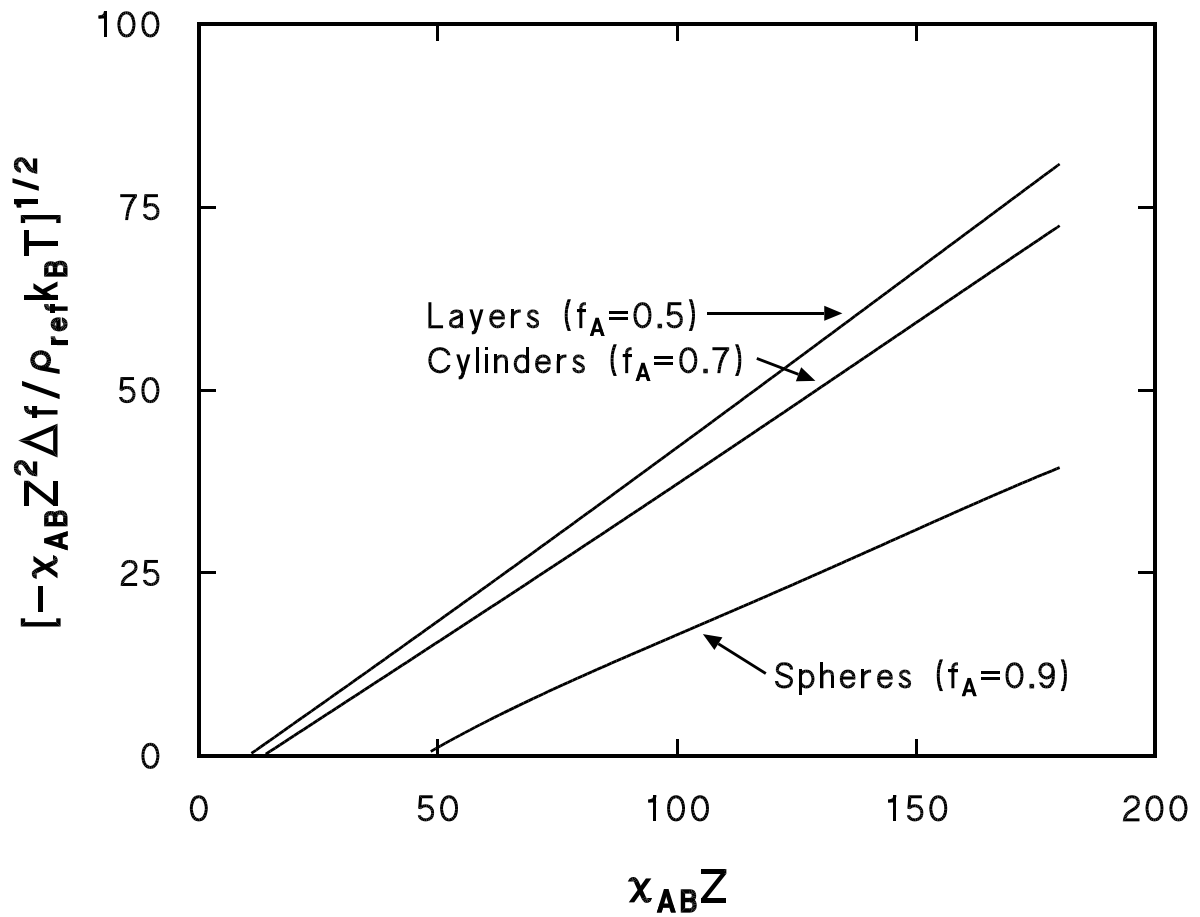


Figure 4.5: Rescaled free energy density as a function of $\chi_{AB}Z$ for the three selected morphologies and associated f_A values.

Chapter 5

Summary and Conclusions

The primary focus of this study has been the determination of the equilibrium microstructures of systems of neat diblock copolymers. In this regard, we have determined through the arguments in Section 3.3, that, in the limit of mean field theory, the system is entirely parameterised by the quantities f_A (the molecular volume fraction of species A), $\chi_{AB}r_C$ (the product of the Flory interaction parameter and the effective degree of polymerization), and $\epsilon = \rho_{0B}b_B^2/\rho_{0A}b_A^2$ (the ratio of the bulk monomer densities multiplied by the square of their associated Kuhn statistical bond lengths).

Our calculated phase diagram, Figure 3.2, is a central result of this work. In it we predict the phase transitions between the homogeneous phase and the three ordered morphologies L, C, and S as illustrated in Figure 1.1 for the case where the bulk monomer densities and the Kuhn statistical lengths of the two species A and B are equal. We have not attempted to model the recently-discovered OBDD structure due to the complexity associated with solving the diffusion equation (2.15) in three dimensions. No dimension-reducing symmetry analogous to the Wigner-Seitz approximation [19] was known for this structure.

In the case studied, $\epsilon = 1$ and so equation (1.3) gives $r_C = Z$ for our calculated phase diagram. For the symmetric copolymer case of $f_A = f_B = 0.5$, the lamellar morphology is always the equilibrium microstructure. Here, we obtain a second-order microphase separation transition with the amplitude of the density variations decreasing continuously

to zero as $\chi_{AB}Z \rightarrow 10.504 \pm 0.004$. For $f_A \neq 0.5$, the first ordered morphology encountered while ascending the graph to larger values of $\chi_{AB}Z$ is the spherical structure, and the transition is first order with a discontinuous change in the amplitude of the density variations crossing this boundary. The MST occurs for increasingly higher $\chi_{AB}Z$ as we move away from $f_A = 0.5$.

These results are in qualitative agreement with Leibler's weak segregation theory in the limit of $\chi_{AB}Z \lesssim 14$. In this region the variations in the densities of the two species are roughly cosine-like. Above this limit, the density profiles begin to flatten, taking on a hyperbolic-tangent quality. In such a regime, Leibler's theory is inadequate. We find as we move to large values of $\chi_{AB}Z$, the phase boundaries between the ordered structures become nearly vertical and thus dependent primarily on f_A . In this limit, the L-C transition occurs at $f_A \approx 0.67$, the C-S transition at $f_A \approx 0.86$. For $\chi_{AB}Z = 80$, the the S-H transition occurs at $f_A \approx 0.93$. As the slope of the S-H phase boundary is not yet vertical at $\chi_{AB}Z = 80$, however, this transition will move to higher f_A as $\chi_{AB}Z$ increases further. Overall, the phase diagram is in good agreement with experimental observation [14] as well as Helfand and Wasserman's NIA theory. [16]

The order-disorder transition is well documented and is also in good agreement with our results. However, to date, there is only one known experimental study which identifies the bending of the L-C and C-S boundaries towards $f_A = 0.5$ in the weak segregation limit. [4] This investigation probed the weak segregation regime of PEP-PEE at $f_A = 0.65$ and discovered temperature dependent transitions from layers to OBDD and OBDD to cylinders before the MST. This was qualitatively consistent with our phase diagram. We have a layers-cylinders transition due to the presence of the L-C boundary at $\chi_{AB}Z \approx 28$ for $f_A = 0.65$. Our theory also predicts a C-S transition, however, which was not observed. This discrepancy can be attributed to a number of factors including polydispersity, metastability, and thermal fluctuations. Furthermore, common

experimental systems such as PS-b-PI and PS-b-PBD typically involve species such that $\epsilon \approx 0.6$. Figure 3.2 is a single planar cross-section of the generalised 3-D phase diagram at $\epsilon = 1$. Though the construction of the full diagram is beyond the scope of this project, it would be interesting to investigate the phase diagram for $\epsilon \neq 1$ and determine whether these C-H and L-H “windows” for $f_A \neq 0.5$ are predicted. Concentrated experimentation in the weak segregation regime may help to clarify this behaviour and determine the adequacy of present theoretical predictions.

In our second investigation, we found that the lattice parameter for all three structures obeyed a rough power law relation $R \propto (\chi_{AB} r_C)^p r_C^{1/2}$ where p was a slowly varying quantity. For our $\epsilon = 1$ system we found that p ranged from 0.2 in the strong segregation limit to 1/2 at the MST for symmetric copolymers. The value of p was predominantly determined by the shape of the density profiles, and, in turn, on the value of $\chi_{AB} Z$. In the case of high asymmetry in f_A , the MST occurred at large values of $\chi_{AB} Z$, and p did not depart significantly from 0.2 over the entire range. These results again agreed with prior treatments in their respective limits, and to an reasonable extent with experiment.

Through the dilution approximation, we demonstrated that our results can be generalised to the case where a solvent is introduced. If we assume the solvent to be uniformly distributed, our phase diagram for the neat diblock copolymer system is entirely equivalent through the substitution of $\chi_{eff} \equiv \bar{\phi}_C \chi_{AB}$ for χ_{AB} where $1 - \bar{\phi}_C$ is the fraction of the system’s volume occupied by the solvent. The power law relations are similarly determined, with the density profiles, potentials and free energies all simply rescaled by a factor of $\bar{\phi}_C$. [3, 28, 29]

The mean field self-consistent theory applies to the full range of system parameters, and thus can be used as a guide by which we can determine the range of validity of these previous approximations and their respective assumptions. Its usefulness is established by comparison with experiment, and its ability to predict generalised properties not

previously known.

However, it should be emphasised that the project presented here constitutes a prototypical study of the fully self-consistent mean field theory. As such, this work establishes a grounding through which numerous opportunities for further study present themselves. The system studied in this thesis used model parameters. Systems of PS-b-PI and PS-b-PBD, two commonly studied diblock copolymers, are such that $\epsilon \approx 0.6$. One could conceivably construct a phase diagram analogous to Figure 3.2 in terms of χ_{AB^rC} and f_A for this ϵ . A study of the domain sizes, analogous to that of Chapter 4, would also be possible. Since both systems have roughly the same value of ϵ , such studies would be applicable to both.

In addition to an interest in systems for which $\epsilon \neq 1$, other relevant copolymer systems are possible. There have been theoretical treatments involving copolymer/homopolymer blends [2] and linear multiblock copolymers [18] (i.e., single copolymer chains with more than two species of monomers). The first of these references involve approximations similar to that of Leibler, carried to higher order; the second used only the lowest-order expansion of free energy and densities.

In addition, advances in polymerization have led to the development of “star diblock copolymers”. [5] These molecules consist of a number of diblock copolymers joined together in a pinwheel pattern at one end. One reason that this architecture is of interest is that, in addition to linear diblock PS-b-PI, star PS-PI is another relatively well studied system in which the Ordered Bicontinuous Double-Diamond structure has been observed. [25] The failure of theoretical attempts to predict this structure to date make for an especially enticing test of the self-consistent mean field theory. The major barrier at present is the required computational power.

To illustrate the extension of our approach to the treatment of other systems, Appendix B outlines the derivation of a self-consistent representation for these three molecular configurations. Through an analogous derivation to that of Chapter 2, we obtained the set of fully self-consistent equations for each of these systems. This has the advantage of being able to model the system for a full range of experimental parameters, without any *a priori* assumptions which restrict us to an undetermined range in the weak segregation regime. This advantage should be extremely useful in experimental comparison where the majority of data available are for strongly segregated systems.

Though self-consistent mean field theory can be applied to such a vast array of problems, it is not the last word in copolymer theory. Ideally, one would ultimately like to include thermal fluctuations for a more complete picture. In an extension of Leibler's theory, Fredrickson and Helfand included such fluctuation terms. [11] In that work, it was found that the C-H and L-H "windows" described above did indeed occur. However, the spherical region of the phase diagram was unrealistically diminished and, in some cases, entirely absent. It should be emphasised, however, that this was still a weak segregation theory. Perhaps, a fully self-consistent theory with fluctuation effects would also generate these C-H and L-H windows, but tempered such that the spherical morphology remained realistic in strong segregation, where fluctuations would be negligible.

Further improvements to our theory are also possible. There are many subtleties to chemical interactions which have been bypassed. In particular, the energetic contribution of the various bond orientations may warrant the inclusion of the detailed molecular structure of the monomers themselves. Certainly, such a treatment would shed a great deal of light on the details of the χ_{AB} interaction parameter, its dependence on temperature, and more generally the form of the interaction potential \hat{V} itself. The detail to which this could be carried out is primarily restricted by available computational power.

Ultimately, we hope that others will find that this treatment shows promise for a new

approach to copolymer modelling, and may lead to further improvements in copolymer theory.

Bibliography

- [1] D. M. Anderson and E. L. Thomas. Microdomain morphology of star copolymers in the strong-segregation limit. *Macromolecules*, 21:3221–3230, 1988.
- [2] M. Banaszak. *Microphase and Macrophase Separation in Binary and Ternary Block Copolymer Blends*. PhD thesis, Memorial University of Newfoundland, 1991.
- [3] M. Banaszak and M. D. Whitmore. Self-consistent theory of block copolymer blends: Selective solvent. *Macromolecules*, (in press).
- [4] F. S. Bates. Phase behavior of polyolefin block copolymers. APS meeting, Division of High Polymer Physics, March 1992.
- [5] L. Bi and L. J. Fetters. Synthesis and properties of block copolymers 3. polystyrene-polydiene star block copolymers. *Macromolecules*, 9:732–742, 1976.
- [6] J. M. G. Cowie. *Polymers: Chemistry & Physics of Modern Materials*. International Textbook Company Limited, Aylesbury, UK, 1973.
- [7] P.-G. de Gennes. *Scaling Concepts in Polymer Physics*. Cornell University Press, Ithaca, N.Y., 1979.
- [8] M. Doi and S. F. Edwards. *The Theory of Polymer Dynamics*. Oxford Science Publications, Oxford, 1986.
- [9] P. J. Flory. *Principles of Polymer Chemistry*. Cornell University Press, Ithaca, N.Y., 1953.

- [10] L. Fox, editor. *Numerical Solution of Ordinary and Partial Differential Equations*. Addison-Wesley, Reading, Mass., 1962.
- [11] G. H. Fredrickson and E. Helfand. Fluctuation effects in the theory of microphase separation in block copolymers. *J. Chem. Phys.*, 87:697–705, 1987.
- [12] K. F. Freed. *Renormalization Group Theory of Macromolecules*. Wiley-Interscience, New York, 1987.
- [13] O. Glatter and O. Kratky, editors. *Small Angle X-ray Scattering*. Academic Press, London, 1982.
- [14] H. Hasegawa, H. Tanaka, K. Yamasaki, and T. Hashimoto. Bicontinuous microdomain morphology of block copolymers 1. tetrapod-network structure of polystyrene-polyisoprene diblock polymers. *Macromolecules*, 20:1651–1662, 1987.
- [15] T. Hashimoto, M. Shibayama, and H. Kawai. Ordered structure in block polymer solutions 4. scaling rules on size of fluctuations with block molecular weight, concentration, and temperature in segregation and homogeneous regions. *Macromolecules*, 16:1093–1101, 1983.
- [16] E. Helfand and Z. R. Wasserman. Microdomain structure and the interface in block copolymers. In I. Goodman, editor, *Developments in Block Copolymers*, volume 1, pages 99–125. Elsevier, New York, 1982.
- [17] K. M. Hong and J. Noolandi. Theory of inhomogeneous multicomponent polymer systems. *Macromolecules*, 14:727–736, 1981.
- [18] T. A. Kavassalis and M. D. Whitmore. On the theory of linear multiblock copolymers. *Macromolecules*, 24:5340–5345, 1991.

- [19] C. Kittel. *Introduction to Solid State Physics*. Wiley, New York, 6th. edition, 1986.
- [20] L. Leibler. Theory of microphase separation in block copolymers. *Macromolecules*, 13:1602–1617, 1980.
- [21] T. Ohta and K. Kawasaki. Equilibrium morphology of block copolymer melts. *Macromolecules*, 19:2621–2632, 1986.
- [22] W. H. Press, B. P. Flannery, S. A. Teukolsky, and W. T. Vetterling. *Numerical Recipes in Pascal: The Art of Scientific Computing*. Cambridge University Press, New York, 1989.
- [23] F. Reif. *Fundamentals of Statistical and Thermal Physics*. McGraw-Hill, New York, 1965.
- [24] K. R. Symon. *Mechanics*. Addison-Wesley, Reading, Mass., 3rd. edition, 1971.
- [25] E. L. Thomas, D. B. Alward, D. J. Kinning, D. C. Martin, D. L. Handlin Jr., and L. J. Fetters. Ordered bicontinuous double-diamond structure of star block copolymers: A new equilibrium microdomain morphology. *Macromolecules*, 19:2197–2202, 1986.
- [26] E. L. Thomas, D. M. Anderson, C. S. Henkee, and D. Hoffman. Periodic area-minimizing surfaces in block copolymers. *Nature*, 334:598–601, 1988.
- [27] M. D. Whitmore and J. Noolandi. Theory of crystallizable block copolymer blends. *Macromolecules*, 21:1482–1496, 1988.
- [28] M. D. Whitmore and J. Noolandi. Self-consistent theory of block copolymer blends: Neutral solvent. *J. Chem. Phys.*, 93:2946–2955, 1990.

- [29] M. D. Whitmore and J. D. Vavasour. Self-consistent mean field theory of the microphase diagram of block copolymer-neutral solvent blends. *Macromolecules*, (in press).
- [30] A. E. Woodward. *Atlas of Polymer Morphology*. Oxford University Press, Don Mills, Ontario, 1988.

Appendix A

Tables of Numerical Results

f_A	Δf (in $10^{-3} \rho_{ref} k_B T$)	
	Layers	Cylinders
0.626	-1.45701±0.00008	-1.44448±0.00010
0.628	-1.43913±0.00013	-1.43113±0.00009
0.630	-1.42100±0.00011	-1.41723±0.00009
0.632	-1.40263±0.00011	-1.40311±0.00008
0.634	-1.38401±0.00015	-1.38873±0.00010
0.636	-1.36516±0.00016	-1.37416±0.00007
0.638	-1.34606±0.00010	-1.35933±0.00008

Table A.1: Free energy comparison between layers and cylinders for $\chi_{AB} = 0.04$, $Z = 500$, $f_A = 0.626$ to 0.638 . This relation is plotted in Figure 3.1.

$\chi_{AB}Z$	<i>L-C transition</i>	<i>C-S transition</i>	<i>S-H transition</i>
10.498	0.5	0.5	0.5
11	0.5416	0.5750	0.5848
12	0.5684	0.6216	0.6414
13	0.5842	0.6536	0.6766
14	0.5956	0.6760	0.7042
15	0.6046	0.6934	0.7246
16	0.6118	0.7078	0.7416
17	0.6178	0.7204	0.7566
18	0.6232	0.7312	0.7702
20	0.6318	0.7492	0.7898
25	0.6460	0.7794	0.8280
30	0.6544	0.7994	0.8524
40	0.6634	0.8268	0.8846
50	0.6680	0.8424	0.9026
60	0.6708	0.8516	0.9168
70	0.6726	0.8584	0.9264
80	0.6738	0.8622	0.9344

Table A.2: Phase transition boundaries for $Z = 500$. The value of f_A at the transition is given at the associated value of $\chi_{AB}Z$. Each point in this table required calculations as outlined in Table A.1 and Figure 3.1.

$\chi_{AB}Z$	<i>L-C transition</i>	<i>C-S transition</i>	<i>S-H transition</i>
10.504	0.5	0.5	0.5
11	0.5415	0.5760	0.5850
12	0.5685	0.6230	0.6425
13	0.5840	0.6545	0.6775
14	0.5955	0.6755	0.7045
15	0.6045	0.6930	0.7255
16	0.6120	0.7070	0.7420
17	0.6180	0.7205	0.7570
18	0.6230	0.7320	0.7695
20	0.6320	0.7480	0.7900
25	0.6460	0.7790	0.8280
30	0.6545	0.8010	0.8535
40	0.6635	0.8265	0.8845
50	0.6680	0.8425	0.9035
60	0.6710	0.8510	0.9165
70	0.6725	0.8575	0.9265
80	0.6740	0.8630	0.9345

Table A.3: Phase transition boundaries for $Z = 200$.

$\chi_{AB}\bar{Z}$	<i>L-C transition</i>	<i>C-S transition</i>	<i>S-H transition</i>
10.503	0.5	0.5	0.5
11	0.5418	0.5718	0.5836
12	0.5683	0.6225	0.6367
13	0.5838	0.6538	0.6777
14	0.5957	0.6736	0.7057
15	0.6047	0.6913	0.7253
16	0.6119	0.7081	0.7419
17	0.6182	0.7200	0.7565
18	0.6228	0.7311	0.7694
20	0.6320	0.7480	0.7900
25	0.6460	0.7792	0.8280
30	0.6543	0.8013	0.8523
40	0.6635	0.8275	0.8853
50	0.6680	0.8424	0.9026
60	0.6708	0.8528	0.9167
70	0.6726	0.8581	0.9267
80	0.6739	0.8634	0.9341

Table A.4: Phase transition boundaries for $\chi_{AB} = 0.1$.

$\chi_{AB}Z$	<i>L-C transition</i>	<i>C-S transition</i>	<i>S-H transition</i>
10.502±0.004	0.5	0.5	0.5
11	0.5416±0.0002	0.5743±0.0022	0.5845±0.0008
12	0.5684±0.0001	0.6224±0.0007	0.6402±0.0031
13	0.5840±0.0002	0.6540±0.0005	0.6773±0.0006
14	0.5956±0.0001	0.6750±0.0013	0.7048±0.0008
15	0.6046±0.0001	0.6926±0.0011	0.7251±0.0005
16	0.6119±0.0001	0.7076±0.0006	0.7418±0.0002
17	0.6180±0.0002	0.7203±0.0003	0.7567±0.0003
18	0.6230±0.0002	0.7314±0.0005	0.7697±0.0004
20	0.6319±0.0001	0.7484±0.0007	0.7899±0.0001
25	0.6460±0.0000	0.7792±0.0002	0.8280±0.0000
30	0.6545±0.0001	0.8006±0.0010	0.8527±0.0007
40	0.6635±0.0001	0.8269±0.0005	0.8848±0.0004
50	0.6680±0.0000	0.8424±0.0001	0.9029±0.0005
60	0.6709±0.0001	0.8518±0.0009	0.9167±0.0002
70	0.6726±0.0001	0.8580±0.0005	0.9265±0.0002
80	0.6739±0.0001	0.8629±0.0006	0.9343±0.0002

Table A.5: Mean phase boundaries of $Z = 500$, $Z = 200$, and $\chi_{AB} = 0.1$ diagrams. These have been used to construct the composite phase diagram, Figure 3.2.

χ_{AB}	Z	d	Δf (in $\rho_{ref}k_B T$)
0.100	120	15.4	$(-3.98272 \pm 0.00231) \times 10^{-4}$
0.150	120	17.6	$(-5.95597 \pm 0.00012) \times 10^{-3}$
0.200	120	19.0	$(-1.39508 \pm 0.00001) \times 10^{-2}$
0.300	120	20.8	$(-3.25495 \pm 0.00001) \times 10^{-2}$
0.100	140	17.6	$(-1.51185 \pm 0.00035) \times 10^{-3}$
0.075	150	16.6	$(-8.77101 \pm 0.03134) \times 10^{-5}$
0.075	160	17.4	$(-2.98680 \pm 0.00207) \times 10^{-4}$
0.100	160	19.6	$(-2.76512 \pm 0.00014) \times 10^{-3}$
0.075	180	19.6	$(-9.05660 \pm 0.00213) \times 10^{-4}$
0.100	180	21.6	$(-3.97050 \pm 0.00015) \times 10^{-3}$
0.060	200	19.8	$(-2.39052 \pm 0.00261) \times 10^{-4}$
0.065	200	20.4	$(-5.94953 \pm 0.00170) \times 10^{-4}$
0.070	200	21.0	$(-1.05837 \pm 0.00018) \times 10^{-3}$
0.075	200	21.4	$(-1.60337 \pm 0.00022) \times 10^{-3}$
0.100	200	23.4	$(-5.07682 \pm 0.00012) \times 10^{-3}$
0.150	200	25.8	$(-1.37733 \pm 0.00001) \times 10^{-2}$
0.200	200	27.6	$(-2.35047 \pm 0.00001) \times 10^{-2}$
0.300	200	30.0	$(-4.44075 \pm 0.00001) \times 10^{-2}$
0.050	220	20.0	$(-2.76530 \pm 0.01310) \times 10^{-5}$
0.050	250	22.4	$(-3.21147 \pm 0.00198) \times 10^{-4}$
0.050	280	24.8	$(-7.67004 \pm 0.00212) \times 10^{-4}$
0.050	310	27.0	$(-1.22623 \pm 0.00014) \times 10^{-3}$
0.050	340	29.0	$(-1.68934 \pm 0.00010) \times 10^{-3}$
0.050	370	31.0	$(-2.12860 \pm 0.00016) \times 10^{-3}$
0.050	400	33.0	$(-2.53843 \pm 0.00011) \times 10^{-3}$
0.075	400	36.6	$(-6.88666 \pm 0.00009) \times 10^{-3}$
0.100	400	39.0	$(-1.17524 \pm 0.00001) \times 10^{-2}$
0.150	400	42.4	$(-2.22038 \pm 0.00001) \times 10^{-2}$

(continued)

Table A.6: Dependence of repeat distance, d (given in units of the Kuhn length), on χ_{AB} and Z for lamellar structure, $f_A = 0.5$. The dependences of repeat distance on χ_{AB} and Z for these parameters are given in Figure 4.1.

χ_{AB}	Z	d	Δf (in $\rho_{ref}k_B T$)
<i>(continued)</i>			
0.200	400	44.8	$(-3.31639 \pm 0.00001) \times 10^{-2}$
0.300	400	48.4	$(-5.58612 \pm 0.00001) \times 10^{-2}$
0.050	600	44.8	$(-4.59111 \pm 0.00007) \times 10^{-3}$
0.075	600	49.0	$(-9.53032 \pm 0.00010) \times 10^{-3}$
0.100	600	52.0	$(-1.48025 \pm 0.00001) \times 10^{-2}$
0.150	600	56.2	$(-2.58405 \pm 0.00001) \times 10^{-2}$
0.200	600	59.2	$(-3.72408 \pm 0.00001) \times 10^{-2}$
0.300	600	63.8	$(-6.06283 \pm 0.00003) \times 10^{-2}$
0.050	800	55.2	$(-5.87618 \pm 0.00006) \times 10^{-3}$
0.075	800	60.0	$(-1.11019 \pm 0.00001) \times 10^{-2}$
0.100	800	63.4	$(-1.65819 \pm 0.00001) \times 10^{-2}$
0.150	800	68.4	$(-2.79306 \pm 0.00001) \times 10^{-2}$
0.200	800	72.2	$(-3.96575 \pm 0.00001) \times 10^{-2}$
0.050	1000	64.6	$(-6.75648 \pm 0.00009) \times 10^{-3}$
0.075	1000	70.0	$(-1.21564 \pm 0.00001) \times 10^{-2}$
0.100	1000	74.0	$(-1.77661 \pm 0.00001) \times 10^{-2}$
0.150	1000	79.8	$(-2.93150 \pm 0.00001) \times 10^{-2}$
0.200	1000	84.0	$(-4.11256 \pm 0.00002) \times 10^{-2}$
0.300	1000	90.8	$(-6.52492 \pm 0.00100) \times 10^{-2}$
0.050	1200	73.4	$(-7.40125 \pm 0.00009) \times 10^{-3}$
0.075	1200	79.4	$(-1.29203 \pm 0.00001) \times 10^{-2}$
0.100	1200	83.8	$(-1.86204 \pm 0.00001) \times 10^{-2}$
0.150	1200	90.4	$(-3.03142 \pm 0.00001) \times 10^{-2}$
0.200	1200	95.2	$(-4.22536 \pm 0.00001) \times 10^{-2}$
0.050	2000	104.6	$(-8.88307 \pm 0.00003) \times 10^{-3}$
0.075	2000	112.8	$(-1.46575 \pm 0.00001) \times 10^{-2}$
0.100	2000	119.0	$(-2.05628 \pm 0.00001) \times 10^{-2}$
0.150	2000	127.8	$(-3.26244 \pm 0.00005) \times 10^{-2}$

χ_{AB}	Z	R	Δf (in $\rho_{ref} k_B T$)
*0.075	190	11.3	$(-1.19380 \pm 0.09049) \times 10^{-5}$
0.100	190	12.0	$(-1.60405 \pm 0.00205) \times 10^{-3}$
0.150	190	13.5	$(-7.62447 \pm 0.00088) \times 10^{-3}$
0.200	190	14.5	$(-1.50889 \pm 0.00004) \times 10^{-2}$
0.300	190	15.9	$(-3.17155 \pm 0.00001) \times 10^{-2}$
0.078	200	11.7	$(-2.43102 \pm 0.01363) \times 10^{-4}$
0.085	200	12.0	$(-7.00308 \pm 0.00430) \times 10^{-4}$
0.093	200	12.3	$(-1.29899 \pm 0.00161) \times 10^{-3}$
0.100	200	12.6	$(-2.00624 \pm 0.00130) \times 10^{-3}$
0.150	200	14.1	$(-8.30272 \pm 0.00085) \times 10^{-3}$
0.200	200	15.1	$(-1.59182 \pm 0.00003) \times 10^{-2}$
0.300	200	16.5	$(-3.27387 \pm 0.00001) \times 10^{-2}$
0.075	280	15.2	$(-1.80514 \pm 0.00091) \times 10^{-3}$
*0.050	290	13.9	$(-3.23277 \pm 0.13725) \times 10^{-5}$
0.050	310	14.7	$(-1.57412 \pm 0.00775) \times 10^{-4}$
0.050	340	15.7	$(-4.13404 \pm 0.00840) \times 10^{-4}$
0.075	350	18.0	$(-3.26468 \pm 0.00040) \times 10^{-3}$
0.050	370	16.7	$(-7.02241 \pm 0.00738) \times 10^{-4}$
*0.036	400	15.7	$(-1.71191 \pm 0.08419) \times 10^{-5}$
0.039	400	16.3	$(-1.22841 \pm 0.00391) \times 10^{-4}$
0.040	400	16.6	$(-1.89127 \pm 0.00085) \times 10^{-4}$
0.045	400	17.3	$(-5.42946 \pm 0.00540) \times 10^{-4}$
0.050	400	17.9	$(-1.00335 \pm 0.00161) \times 10^{-3}$
0.075	400	19.9	$(-4.15133 \pm 0.00023) \times 10^{-3}$
0.100	400	21.3	$(-7.95909 \pm 0.00013) \times 10^{-3}$
0.150	400	23.3	$(-1.63694 \pm 0.00001) \times 10^{-2}$
0.200	400	24.6	$(-2.53112 \pm 0.00001) \times 10^{-2}$
0.300	400	26.6	$(-4.39824 \pm 0.00001) \times 10^{-2}$

(continued)

Table A.7: Dependence of cell radius, R (given in Kuhn lengths), on χ_{AB} and Z for cylindrical structure at $f_A = 0.7$. The asterisks indicate metastable structures where the spheres have lower free energy for the same χ_{AB} and Z . The dependences of cell radius on χ_{AB} and Z for these parameters are given in Figure 4.2.

χ_{AB}	Z	R	Δf (in $\rho_{ref}k_B T$)
<i>(continued)</i>			
0.036	600	22.5	$(-9.51640 \pm 0.00311) \times 10^{-4}$
0.050	600	24.4	$(-2.76756 \pm 0.00017) \times 10^{-3}$
0.075	600	26.8	$(-6.65815 \pm 0.00007) \times 10^{-3}$
0.100	600	28.5	$(-1.09129 \pm 0.00001) \times 10^{-3}$
0.150	600	30.9	$(-1.99342 \pm 0.00001) \times 10^{-2}$
0.200	600	32.6	$(-2.93216 \pm 0.00001) \times 10^{-2}$
0.300	600	35.1	$(-4.86695 \pm 0.00001) \times 10^{-2}$
0.036	800	27.9	$(-1.86323 \pm 0.00017) \times 10^{-3}$
0.050	800	30.2	$(-3.97954 \pm 0.00007) \times 10^{-3}$
0.075	800	32.9	$(-8.18471 \pm 0.00006) \times 10^{-3}$
0.100	800	34.8	$(-1.26556 \pm 0.00001) \times 10^{-2}$
0.150	800	37.6	$(-2.19912 \pm 0.00001) \times 10^{-2}$
0.200	800	39.7	$(-3.16182 \pm 0.00001) \times 10^{-2}$
0.050	1000	35.4	$(-4.82880 \pm 0.00006) \times 10^{-3}$
0.075	1000	38.5	$(-9.21688 \pm 0.00006) \times 10^{-3}$
0.100	1000	40.6	$(-1.38198 \pm 0.00001) \times 10^{-2}$
0.150	1000	43.8	$(-2.33536 \pm 0.00001) \times 10^{-2}$
0.036	1200	37.6	$(-3.08328 \pm 0.00006) \times 10^{-3}$
0.050	1200	40.3	$(-5.45647 \pm 0.00006) \times 10^{-3}$
0.075	1200	43.6	$(-9.96710 \pm 0.00004) \times 10^{-3}$
0.100	1200	46.1	$(-1.46608 \pm 0.00001) \times 10^{-2}$
0.036	2000	54.0	$(-4.33808 \pm 0.00004) \times 10^{-3}$
0.050	2000	57.5	$(-6.90991 \pm 0.00002) \times 10^{-3}$
0.075	2000	62.0	$(-1.16768 \pm 0.00001) \times 10^{-2}$

χ_{AB}	Z	R	Δf (in $\rho_{ref} k_B T$)
0.300	180	11.3	$(-8.00590 \pm 0.05256) \times 10^{-4}$
0.300	190	11.7	$(-1.31606 \pm 0.00233) \times 10^{-3}$
0.030	200	12.1	$(-1.84661 \pm 0.00969) \times 10^{-3}$
0.300	250	14.0	$(-4.57432 \pm 0.00523) \times 10^{-3}$
0.200	260	13.4	$(-3.27635 \pm 0.05612) \times 10^{-4}$
0.300	260	14.4	$(-5.07325 \pm 0.00149) \times 10^{-3}$
0.200	330	15.7	$(-1.97460 \pm 0.00179) \times 10^{-3}$
0.150	400	17.0	$(-9.27576 \pm 0.01733) \times 10^{-4}$
0.200	400	18.0	$(-3.60280 \pm 0.00064) \times 10^{-3}$
0.300	400	19.6	$(-1.03598 \pm 0.00017) \times 10^{-2}$
0.100	600	20.9	$(-6.17806 \pm 0.00944) \times 10^{-4}$
0.150	600	22.6	$(-3.45302 \pm 0.00071) \times 10^{-3}$
0.075	800	24.2	$(-4.64754 \pm 0.00696) \times 10^{-4}$
0.150	800	27.8	$(-5.18109 \pm 0.00202) \times 10^{-3}$
0.200	800	29.3	$(-8.88927 \pm 0.00170) \times 10^{-3}$
0.075	1000	28.0	$(-1.14217 \pm 0.00165) \times 10^{-3}$
0.100	1000	29.9	$(-2.74224 \pm 0.00213) \times 10^{-3}$
0.150	1000	32.6	$(-6.35503 \pm 0.00013) \times 10^{-3}$
0.050	1200	29.3	$(-3.08714 \pm 0.00378) \times 10^{-4}$
0.100	1200	34.1	$(-3.45165 \pm 0.00002) \times 10^{-3}$
0.150	1200	37.1	$(-7.20442 \pm 0.00064) \times 10^{-3}$

Table A.8: Dependence of cell radius, R (given in Kuhn lengths), on χ_{AB} and Z for spherical structure at $f_A = 0.9$. The dependences of cell radius on χ_{AB} and Z for these parameters are given in Figure 4.3.

Appendix B

Extensions to Other Architectures and Blends

B.1 Linear Multiblock Copolymers

In this section, we outline the method by which the theory can be extended to linear block copolymers containing three or more species. Here, we denote the blocks numerically (i.e., $\kappa = 1, 2, 3$, etc.). Connecting the $\tau = Z_\kappa$ monomer in block κ to the $\tau = 0$ monomer in block $\kappa + 1$, the partition function is written as

$$\begin{aligned} \mathbf{Z} = & \frac{Z_C^{\tilde{N}_C}}{\tilde{N}_C!} \int \prod_{i=1}^{\tilde{N}_C} \left\{ \prod_{\kappa=1}^N \delta[\mathbf{r}_{\kappa i}(\cdot)] P_\kappa[\mathbf{r}_{\kappa i}(\cdot)] \right\} \times \\ & \left\{ \prod_{\kappa=1}^{N-1} \delta[\mathbf{r}_{\kappa i}(Z_\kappa) - \mathbf{r}_{\kappa+1i}(0)] \right\} \times \\ & \prod_{\mathbf{r}} \delta\left[1 - \sum_{\kappa=1}^N \frac{\hat{\rho}_\kappa(\mathbf{r})}{\rho_{0\kappa}}\right] \exp[-\beta\hat{V}(\cdot)], \end{aligned} \quad (\text{B.1})$$

where N is the number of blocks. By an analogous transform that gave us equation (2.17) for diblock copolymers, we get [18]

$$Q_C = \int_{\Omega} d^3R_1 \cdots d^3R_{N+1} Q_1(\mathbf{R}_2, Z_1 | \mathbf{R}_1) \cdots Q_N(\mathbf{R}_{N+1}, Z_N | \mathbf{R}_N). \quad (\text{B.2})$$

Expressing the mean field equation (2.24) in terms of the volume fraction, we have

$$\phi_\kappa(\mathbf{r}) = -\frac{\bar{\phi}_\kappa}{Z_\kappa} \frac{\Omega}{Q_C} \frac{\delta Q_C}{\delta \omega_\kappa(\mathbf{r})}. \quad (\text{B.3})$$

Thus,

$$\phi_\kappa(\mathbf{r}) = \frac{\bar{\phi}_\kappa}{Z_\kappa} \frac{\Omega}{Q_C} \int_0^{Z_\kappa} d\tau \int d^3R_1 \cdots d^3R_{N+1} \times$$

$$\begin{aligned}
 & Q_1(\mathbf{R}_2, Z_1 | \mathbf{R}_1) \cdots Q_{\kappa-1}(\mathbf{R}_\kappa, Z_{\kappa-1} | \mathbf{R}_{\kappa-1}) \times \\
 & Q_\kappa(\mathbf{r}, \tau | \mathbf{R}_\kappa) Q_\kappa(\mathbf{R}_{\kappa+1}, Z_\kappa - \tau | \mathbf{r}) \times \\
 & Q_{\kappa+1}(\mathbf{R}_{\kappa+2}, Z_{\kappa+1} | \mathbf{R}_{\kappa+1}) \cdots Q_N(\mathbf{R}_{N+1}, Z_N | \mathbf{R}_N). \quad (\text{B.4})
 \end{aligned}$$

Note that this is the volume fraction due to *block* κ . In the case where several blocks are of the same species, as in an ABA-type triblock copolymer, [30] we may obtain the species volume fraction via the restricted sum

$$\phi_{\text{species}}(\mathbf{r}) = \sum_{\kappa}^{\text{species}} \phi_{\kappa}(\mathbf{r}), \quad (\text{B.5})$$

where the summation includes all blocks of the species in question.

Defining the functions

$$\begin{aligned}
 q_\kappa(\mathbf{r}, \tau) \equiv & \int_{\Omega} d^3 R_1 \cdots d^3 R_\kappa \times \\
 & Q_1(\mathbf{R}_2, Z_1 | \mathbf{R}_1) \cdots Q_{\kappa-1}(\mathbf{R}_\kappa, Z_{\kappa-1} | \mathbf{R}_{\kappa-1}) Q_\kappa(\mathbf{r}, \tau | \mathbf{R}_\kappa), \quad (\text{B.6})
 \end{aligned}$$

$$\begin{aligned}
 q'_\kappa(\mathbf{r}, \tau) \equiv & \int_{\Omega} d^3 R_{\kappa+1} \cdots d^3 R_{N+1} Q_\kappa(\mathbf{R}_{\kappa+1}, \tau | \mathbf{r}) \times \\
 & Q_{\kappa+1}(\mathbf{R}_{\kappa+2}, Z_{\kappa+1} | \mathbf{R}_{\kappa+1}) \cdots Q_N(\mathbf{R}_{N+1}, Z_N | \mathbf{R}_N), \quad (\text{B.7})
 \end{aligned}$$

we find that $\phi_\kappa(\mathbf{r})$ now satisfies (2.61) as before. The functions $q_\kappa(\mathbf{r}, \tau)$ and $q'_\kappa(\mathbf{r}, \tau)$ are easily shown to satisfy the diffusion equation, with initial conditions obtained via (2.16) as

$$q_1(\mathbf{r}, 0) = 1, \quad (\text{B.8})$$

$$q'_N(\mathbf{r}, 0) = 1, \quad (\text{B.9})$$

$$q_{\kappa+1}(\mathbf{r}, 0) = q_\kappa(\mathbf{r}, Z_\kappa) \quad \text{for } 1 \leq \kappa < N, \quad (\text{B.10})$$

$$q'_{\kappa-1}(\mathbf{r}, 0) = q'_\kappa(\mathbf{r}, Z_\kappa) \quad \text{for } 1 < \kappa \leq N. \quad (\text{B.11})$$

In terms of these functions, Q_C is

$$Q_C = \int_{\Omega} d^3 r q_N(\mathbf{r}, Z_N) \quad (\text{B.12})$$

$$= \int_{\Omega} d^3r q'_1(\mathbf{r}, Z_1). \quad (\text{B.13})$$

The potentials and free energy density are easily obtained as

$$\omega_{\kappa}(\mathbf{r}) = \frac{\rho_{ref}}{\rho_{0\kappa}} \left\{ \sum_{\kappa' \neq \kappa}^N \chi_{\kappa\kappa'} [\phi_{\kappa}(\mathbf{r}) - \bar{\phi}_{\kappa} + \frac{\sigma_{\kappa\kappa'}^2}{6} \nabla^2 \phi_{\kappa}(\mathbf{r})] + \frac{\eta(\mathbf{r})}{\rho_{ref}} \right\}, \quad (\text{B.14})$$

$$\begin{aligned} \frac{\Delta f}{\rho_{ref} k_B T} &= \frac{1}{\Omega} \int_{\Omega} d^3r \left\{ \frac{1}{2} \sum_{\kappa=1}^N \sum_{\kappa' \neq \kappa}^N \chi_{\kappa\kappa'} [\phi_{\kappa}(\mathbf{r}) \phi_{\kappa'}(\mathbf{r}) - \bar{\phi}_{\kappa} \bar{\phi}_{\kappa'} - \right. \\ &\quad \left. \frac{\sigma_{\kappa\kappa'}^2}{6} \nabla \phi_{\kappa}(\mathbf{r}) \cdot \nabla \phi_{\kappa'}(\mathbf{r})] - \right. \\ &\quad \left. \sum_{\kappa=1}^N \frac{\rho_{0\kappa}}{\rho_{ref}} \omega_{\kappa}(\mathbf{r}) \phi_{\kappa}(\mathbf{r}) \right\} - \frac{1}{r_C} \ln \frac{Q_C}{\Omega}, \end{aligned} \quad (\text{B.15})$$

with the incompressibility condition given by

$$\sum_{\kappa=1}^N \phi_{\kappa}(\mathbf{r}) = 1. \quad (\text{B.16})$$

Here, $r_C \equiv \sum_{\kappa=1}^N r_{\kappa}$. The expressions are equivalent if we sum over species instead of blocks. This formulation reduces to the diblock copolymer case for $N = 2$ where $q_A(\mathbf{r}, \tau) \equiv q_1(\mathbf{r}, \tau)$, $q_B(\mathbf{r}, \tau) \equiv q'_2(\mathbf{r}, \tau)$, $q'_A(\mathbf{r}, \tau) \equiv q'_1(\mathbf{r}, \tau)$, and $q'_B(\mathbf{r}, \tau) \equiv q_2(\mathbf{r}, \tau)$.

B.2 Star Diblock Copolymers

An N -armed star diblock copolymer consists of N linear diblock copolymers connected at one end to form a pinwheel pattern. If we designate species B as the hub of this molecule and species A as the limbs, we have a partition function in the form

$$\begin{aligned} \mathbf{Z} = & \frac{Z_C^{\tilde{N}_C}}{\tilde{N}_C!} \int \prod_{i=1}^{\tilde{N}_C} d^3 \mathcal{R}_i \prod_{j=1}^N \delta \mathbf{r}_{Aij}(\cdot) \delta \mathbf{r}_{Bij}(\cdot) \times \\ & P_A[\mathbf{r}_{Aij}(\cdot)] P_B[\mathbf{r}_{Bij}(\cdot)] \times \\ & \delta[\mathbf{r}_{Aij}(Z_{Aj}) - \mathbf{r}_{Bij}(Z_{Bj})] \delta[\mathbf{r}_{Bij}(0) - \mathbf{R}_i] \times \\ & \prod_{\mathbf{r}} \delta \left[1 - \frac{\hat{\rho}_A(\mathbf{r})}{\rho_{0A}} - \frac{\hat{\rho}_B(\mathbf{r})}{\rho_{0B}} \right] \exp[-\beta \hat{V}(\cdot)]. \end{aligned} \quad (\text{B.17})$$

The additional vector \mathbf{R}_i indicates the position of the hub of molecule i . An additional subscript j distinguishes the arms of the pinwheel. The associated Q_C will be

$$Q_C = \int_{\Omega} d^3 \mathcal{R} \prod_{j=1}^N d^3 R_j d^3 R'_j Q_{Aj}(\mathbf{R}'_j, Z_{Aj} | \mathbf{R}_j) Q_{Bj}(\mathbf{R}_j, Z_{Bj} | \mathbf{R}). \quad (\text{B.18})$$

From (B.3), we have

$$\begin{aligned} \phi_{Aj}(\mathbf{r}) = & \frac{\bar{\phi}_{Aj}}{Z_{Aj}} \frac{\Omega}{Q_C} \int_0^{Z_{Aj}} d\tau \int_{\Omega} d^3 \mathcal{R} d^3 R_1 \cdots d^3 R_N d^3 R'_1 \cdots d^3 R'_N \times \\ & Q_{A1}(\mathbf{R}'_1, Z_{A1} | \mathbf{R}_1) \cdots Q_{Aj-1}(\mathbf{R}'_{j-1}, Z_{Aj-1} | \mathbf{R}_{j-1}) \times \\ & Q_{Aj}(\mathbf{R}'_j, \tau | \mathbf{r}) Q_{Aj}(\mathbf{r}, Z_{Aj} - \tau | \mathbf{R}_j) \times \\ & Q_{Aj+1}(\mathbf{R}'_{j+1}, Z_{Aj+1} | \mathbf{R}_{j+1}) \cdots Q_{AN}(\mathbf{R}'_N, Z_{AN} | \mathbf{R}_N) \times \\ & Q_{B1}(\mathbf{R}_1, Z_{B1} | \mathbf{R}) \cdots Q_{BN}(\mathbf{R}_N, Z_{BN} | \mathbf{R}), \end{aligned} \quad (\text{B.19})$$

$$\begin{aligned} \phi_{Bj}(\mathbf{r}) = & \frac{\bar{\phi}_{Bj}}{Z_{Bj}} \frac{\Omega}{Q_C} \int_0^{Z_{Bj}} d\tau \int_{\Omega} d^3 \mathcal{R} d^3 R_1 \cdots d^3 R_N d^3 R'_1 \cdots d^3 R'_N \times \\ & Q_{A1}(\mathbf{R}'_1, Z_{A1} | \mathbf{R}_1) \cdots Q_{AN}(\mathbf{R}'_N, Z_{AN} | \mathbf{R}_N) \times \\ & Q_{B1}(\mathbf{R}_1, Z_{B1} | \mathbf{R}) \cdots Q_{Bj-1}(\mathbf{R}_{j-1}, Z_{Bj-1} | \mathbf{R}) \times \\ & Q_{Bj}(\mathbf{R}_j, \tau | \mathbf{r}) Q_{Bj}(\mathbf{r}, Z_{Bj} - \tau | \mathbf{R}_j) \times \\ & Q_{Bj+1}(\mathbf{R}_{j+1}, Z_{Bj+1} | \mathbf{R}) \cdots Q_{BN}(\mathbf{R}_N, Z_{BN} | \mathbf{R}). \end{aligned} \quad (\text{B.20})$$

Here, $\phi_{\kappa j}(\mathbf{r})$ is the volume fraction of arm j of species κ . The total volume fraction for species κ would be

$$\phi_{\kappa}(\mathbf{r}) = \sum_{j=1}^N \phi_{\kappa j}(\mathbf{r}). \quad (\text{B.21})$$

We define the convolutions

$$q_{A_j}(\mathbf{r}, \tau) \equiv \int_{\Omega} d^3 r' Q_{A_j}(\mathbf{r}, \tau | \mathbf{r}'), \quad (\text{B.22})$$

$$q'_{B_j}(\mathbf{r}, \tau) \equiv \int_{\Omega} d^3 r' q_{A_j}(\mathbf{r}', Z_{A_j}) Q_{B_j}(\mathbf{r}, \tau | \mathbf{r}'), \quad (\text{B.23})$$

$$q_{B_j}(\mathbf{r}, \tau) \equiv \int_{\Omega} d^3 r' Q_{B_j}(\mathbf{r}, \tau | \mathbf{r}') \prod_{i \neq j}^N q'_{B_i}(\mathbf{r}', Z_{B_i}), \quad (\text{B.24})$$

$$q'_{A_j}(\mathbf{r}, \tau) \equiv \int_{\Omega} d^3 r' Q_{A_j}(\mathbf{r}, \tau | \mathbf{r}') q_{B_j}(\mathbf{r}, Z_{B_j}). \quad (\text{B.25})$$

These functions satisfy the diffusion equation with initial conditions

$$q_{A_j}(\mathbf{r}, 0) = 1, \quad (\text{B.26})$$

$$q'_{B_j}(\mathbf{r}, 0) = q_{A_j}(\mathbf{r}, Z_{A_j}), \quad (\text{B.27})$$

$$q_{B_j}(\mathbf{r}, 0) = \prod_{i \neq j}^N q'_{B_i}(\mathbf{r}, Z_{B_i}), \quad (\text{B.28})$$

$$q'_{A_j}(\mathbf{r}, 0) = q_{B_j}(\mathbf{r}, Z_{B_j}). \quad (\text{B.29})$$

In the case where all arms are identical, we may drop the j subscripts, giving

$$q_A(\mathbf{r}, 0) = 1, \quad (\text{B.30})$$

$$q'_B(\mathbf{r}, 0) = q_A(\mathbf{r}, Z_A), \quad (\text{B.31})$$

$$q_B(\mathbf{r}, 0) = [q'_B(\mathbf{r}, Z_B)]^{N-1}, \quad (\text{B.32})$$

$$q'_A(\mathbf{r}, 0) = q_B(\mathbf{r}, Z_B). \quad (\text{B.33})$$

In this form, $\bar{\phi}_{\kappa} = N \bar{\phi}_{\kappa j}$ and so we obtain the species densities $\phi_{\kappa}(\mathbf{r})$ from equation (2.61) and Q_C from (2.60). The expressions for the potentials, incompressibility, and free energies are exactly as for the linear diblock case. The only distinction is in the initial conditions, which are recovered when $N = 1$.

B.3 Copolymer/Homopolymer Blends

In the previous examples, Q_C described the structure of the molecule in terms of the propagators. For a linear multiblock (B.2), block 1 starts at \mathbf{R}_1 and ends at \mathbf{R}_2 , block 2 starts at \mathbf{R}_2 and ends at \mathbf{R}_3 and so on. In the case of the star block copolymer, equation (B.18) specifies N blocks of species B starting at \mathbf{R} and ending at \mathbf{R}_j . The j -th A block then starts at \mathbf{R}_j and ends at \mathbf{R}'_j .

When more than one type of molecule is present, we have a separate function analogous to Q_C for each architecture. This is illustrated fully in reference [2]. In that work, the density variations in the blend were approximated by a finite number of their Fourier components and the free energy evaluated to fourth order. Here we outline how the same systems can be studied numerically through the fully self-consistent mean field theory.

Taking the example of a system consisting of both diblock copolymers and homopolymers (i.e., single species polymers), we will have a Q_C for the copolymer as found in Chapter 2. We also have a Q_H describing the homopolymer: [17]

$$Q_H = \int_{\Omega} d^3r d^3r' Q_H(\mathbf{r}, Z_H | \mathbf{r}'). \quad (\text{B.34})$$

Applying equation (B.3), we have the homopolymer volume fraction as

$$\phi_H(\mathbf{r}) = \frac{\bar{\phi}_H}{Z_H} \frac{\Omega}{Q_C} \int_0^{Z_H} d\tau q_H(\mathbf{r}, \tau) q_H(\mathbf{r}, Z_H - \tau), \quad (\text{B.35})$$

where

$$q_H(\mathbf{r}, \tau) \equiv \int_{\Omega} d^3r' Q_H(\mathbf{r}, \tau | \mathbf{r}'), \quad (\text{B.36})$$

satisfies the diffusion equation with initial condition

$$q_H(\mathbf{r}, 0) = 1. \quad (\text{B.37})$$

The diffusion equations for each molecule are solved separately.

The potentials are analogous to that of the generalised expression given in equation (B.14) where κ , here, corresponds to one of the two copolymer blocks A or B , or the homopolymer component H . That is,

$$\omega_A(\mathbf{r}) = \frac{\rho_{ref}}{\rho_{0A}} \left\{ \chi_{AB} [\phi_B(\mathbf{r}) - \bar{\phi}_B + \frac{\sigma_{AB}^2}{6} \nabla^2 \phi_B(\mathbf{r})] + \chi_{AH} [\phi_H(\mathbf{r}) - \bar{\phi}_H + \frac{\sigma_{AH}^2}{6} \nabla^2 \phi_H(\mathbf{r})] + \frac{\eta(\mathbf{r})}{\rho_{ref}} \right\}, \quad (\text{B.38})$$

with similar expressions for $\omega_B(\mathbf{r})$ and $\omega_H(\mathbf{r})$ obtained by exchanging the appearances of A and B or A and H respectively. The free energy density is also as for equation (B.15), *except* that the substitution

$$-\frac{1}{r_C} \ln \frac{Q_C}{\Omega} \rightarrow -\frac{\bar{\phi}_C}{r_C} \ln \frac{Q_C}{\Omega} - \frac{\bar{\phi}_H}{r_H} \ln \frac{Q_H}{\Omega}, \quad (\text{B.39})$$

must be made. This corresponds to the presence of the $Q_H^{\tilde{N}_H}$ term in the partition function. A similar term must be added for each molecular architecture present.

The numerical solution for all three systems described in this appendix would follow exactly the same discretisation and iteration methods as described in Section 2.3 for the diblock copolymer case. One may further generalise this to any blend, where the diffusion equations would be solved for each molecule individually, with the interactions carried through the potentials and free energy density. As well, more exotic molecular architectures can also be considered.